Julius-Maximilians-Universität Würzburg
Graduate School of Science and Technology

Doctoral thesis / Dissertation

for the doctoral degree / zur Erlangung des Doktorgrads

Doctor rerum naturalium (Dr. rer. nat.)

Spectroscopic investigation of molecular adsorption and desorption from individual single-wall carbon nanotubes

Spektroskopische Untersuchung von molekularer Adsorption und Desorption an einzelnen einwandigen Kohlenstoffnanoröhren

Submitted by / Vorgelegt von

Matthias J. Kastner

from / aus Würzburg

Würzburg, Sep 16, 2020

Submitted on / Eingereicht am: 19.12.2019

Stamp / Stempel Graduate School

Members of thesis committee / Mitglieder des Promotionskomitees
Chairperson / Vorsitz: Prof. Dr. Matthias Bode
1. Reviewer and Examiner / 1. Gutachter und Prüfer: Prof. Dr. Tobias Hertel
2. Reviewer and Examiner / 2. Gutachter und Prüfer: Prof. Dr. Ingo Fischer
3. Examiner / 3. Prüfer: Prof. Dr. Todd B. Marder

Day of thesis defense / Tag des Promotionskolloquiums: 29.05.2020

Affidavit

I hereby confirm that my thesis entitled Spectroscopic investigation of molecular adsorption and desorption from individual single-wall carbon nanotubes is the result of my own work. I did not receive any help or support from commercial consultants. All sources and / or materials applied are listed and specified in the thesis.

Furthermore, I confirm that this thesis has not yet been submitted as part of another examination process neither in identical nor in similar form.

Place, Date   Signature

Eidesstattliche Erklärung

Hiermit erkläre ich an Eides statt, die Dissertation Spektroskopische Untersuchung von molekularer Adsorption und Desorption an einzelnen einwandigen Kohlenstoffnanoröhren eigenständig, d.h. insbesondere selbständig und ohne Hilfe eines kommerziellen Promotionsberaters, angefertigt und keine anderen als die von mir angegebenen Quellen und Hilfsmittel verwendet zu haben.

Ich erkläre außerdem, dass die Dissertation weder in gleicher noch in ähnlicher Form bereits in einem anderen Prüfungsverfahren vorgelegen hat.

Ort, Datum   Unterschrift

special thanks to Shohei Chiashi.

CONTENTS

INTRODUCTION

Fig. 1: Molecular Adsorptions on a Single-Wall Carbon Nanotube.

Down-scaling of electronic circuits has undoubtedly determined the evolution of technology in the past 50 years. For decades, the semiconductor industry relied on an exponential growth predicted by Moore in 1965 [1]. While being a landmark for the prediction of demands in information technology, Moore's Law is at its limit in current silicon technology. Economic pressure has forced mass production in 7nm technology stacking circuits in three dimensions, but further down-scaling of the two-dimensional base circuits is not likely to happen in silicon-based fabrication technology. Bringing the production of electronics below the 10nm limit will require the use of new technologies for electronic components.

Carbon nanotubes have attracted considerable attention due to their defined nano-scaled structure and strongly varying electronic properties. A long search for synthesis conditions finally led to an excellent control over the process using sustainable carbon

sources.[2] The electronic properties originate from monolayer graphene and are highly adjustable to give either semiconducting or metallic nanotubes. The diameter and roll-up angle of a nanotube control the band structure by changing the symmetric arrangement of p-orbitals. As the diameter gets smaller, electronic effects become more prominent, and changes in the dielectric medium have a higher impact.[3]

Recent improvements to the synthesis [4][5] allow much better control of the production process and significantly increase the number of nanotubes with diameters and emission wavelengths that are below those of the (6,5) type. Today, almost every synthesis of semiconducting carbon nanotubes leads to a mixture of nanotubes with similar diameters. For applications like the production of transistors, it is, however, favorable to produce only specific types. Preselection can be performed through synthesis, but today, such selection is better achieved through wet processing with polymers [6] that selectively adsorb on the surface of specific types and remove metallic nanotubes. This adsorption is a combination of solvent, π-stacking, and dispersion forces and is not fully understood.[7] A more detailed look into these adsorption mechanisms could give a better insight for more efficient separation of nanotube types.

Nanotube-based electronics are an alternative to silicon-based electronics. Such electronics are down-scalable, do not require the use of rare earth metals to achieve their unique properties, and can be synthesized from sustainable precursors. Metallic nanotubes can be used to transport charges and semiconducting nanotubes to form electronic components. In 2012, IBM presented the first implementation of semiconducting carbon nanotubes as a transistor in a sub-10nm geometry[8]. These investigations enabled to build the first operable computer [9] using carbon nanotubes as transistors. To increase computation power, a caching memory for storing intermediate calculation results, and a power source are crucial. Supercapacitors fulfill both of these needs. Following theoretical predictions, carbon nanotubes are very suitable as electrodes in supercapacitors [10]. Research on all-carbon electronics should, therefore, be highly favorable. However, almost no experimental evidence for the usage of carbon nanotubes as supercapacitors are available since adsorption processes on the single nanotube level are not so easily be observed and are generally hard to understand.

The photoluminescence of semiconducting carbon nanotubes is in the short wave infrared (SWIR) region. This region is important for enhancing the image contrast in biological samples as it avoids blood and water absorptions typically present in biological tissue.[11] Also, glass fibers do not show absorption in the SWIR range, which enables a better transmission of data at telecom wavelengths. Moreover, the photoluminescence has shown single-photon emission [12][13], which enables the use of semiconducting carbon nanotubes in quantum cryptography. Such a transmission technique is operable on any existing fiber glass network. As carbon nanotubes also show electroluminescence

with high carrier-to-photon conversion efficiencies [14] nano-scaled lasing components became possible that can be coupled efficiently to wave-guides. It was also recently found that sp^3-defects highly enhance these emission properties. These defects both show luminescence up-conversion in biological tissues [15], and photon anti-bunching [16][17][18] at room temperature. Such defects can be efficiently synthesized through chemisorbed hydrogen [19] on the surface of nanotubes.

The highest culprit, however, is the generally low photoluminescence quantum yield of nanotubes that is caused by further irradiative decay paths in these systems. The transfer to solvent for wet processing, for example, leads to a major loss in nanotube emission through non-radiative decay paths of the excitonic states. The structural arrangement of such molecules on a carbon nanotube can also be used to form various properties. The emission strength of these excitons is highly influenced by physisorbed molecules on the nanotube surface.

Carbon Nanotubes only consist of surface atoms and exhibit a high surface to volume ratio. All nanotube-based technology is, therefore, based on surface adsorptions. In the following, I will investigate these surface interactions on the single-molecule level focussing on nanotubes with diameters of 0.7-1.2nm. It will be shown that the initial gas adsorption that is inherent in air significantly shifts the emission energy. Gas adsorption is also responsible for the introduction of new states through sp^3-defects. Further findings allow us to estimate the quantum yield loss in different solvents and help to shed light on the different processes during polymer adsorption that are responsible for a selective sorting of specific carbon nanotube roll-up angles. The first chapter focusses on the experiment design for the synthesis and microscopic investigation of suspended nanotubes which allows making statistically significant analyses. It starts by giving a short introduction on the history of nanotube synthesis before introducing the setup.

METHODS
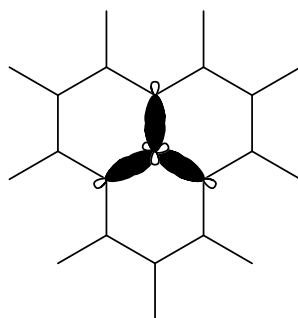
Fig. 1: The hexagonal unit cell of graphitic carbon consists of a planar arrangement of sp^2 hybridized carbon with p$_Z$ orbitals pointing out of the plane.

The correct synthesis and identification of new materials is the key to more thorough analyses. In this chapter I will give a historical introduction to the synthesis of carbon nanotubes and in the further course concentrate on the here chosen synthesis technique for fabricating samples with small diameters. I will then introduce the microscopic setup that was developed to perform a spectroscopic investigation of molecular adsorption and desorption from individual single-wall carbon nanotubes (SWNT). The adsorption processes have been grouped into Adsorption of Gas, Adsorption of Liquid, and Adsorption of Solid.

2.1 Early Synthesis

Although the synthesis of carbon nanotubes is almost 90 years old, it had gathered higher interest only when suitable measurements revealed the material's nanoscale composition and astonishing photonic properties.

2.1.1 1930

From what we can say with today's insights into synthesis conditions and techniques for the production of carbon nanotubes, the first report on a successful synthesis and confirmation of the nanostructure of the material was released in 1932 by Ulrich Hofmann from the Technical University of Berlin.[20][21] He worked with his father who by then had a research experience on graphitic carbon allotropes of more than ten years[22][23]. Hofmann et al. distinctively identified a new form of hexagonal carbon by looking at changes in the hexagonal crystal unit cells for different synthesis temperatures between 400°C and 950°C.

Note: Besides using X-ray diffraction, hexagonal unit cells of graphitic carbon can be identified by Potassium K adsorption tests where calorimetrically three different adsorption states of Potassium per Carbon (16M, 8M, 4M) are identifiable.[24]

The structure was neither comparable to the lustrous graphenic form which forms on a substrate at 930°C [25] nor to the black amorphous carbon structures that are found above 950°C. The new material was shown to form on iron, cobalt and nickel catalyst at 850°C and 950°C. In their paper, they proposed a hexagonal prism with rounded edges as the unit cell. The diameter of this unit cell was measured to be 1.4nm at 850°C and 1.7nm at 950°C which is a reasonable mean carbon nanotube diameter for the used benzine precursor at these temperatures.

Note: A calculated roll-up angle for these structures would be 13° and 15° which is roughly the mean average of the theoretical minimum and maximum angle of carbon nanotubes.

The electron microscope was invented in 1933 and became commercially available in 1938.[26] It is noteworthy that these early reports did not have access to this technique. Consequently, Hofmann analyzed the material that he synthesized in 1932 with this new microscopy technique almost ten years later in 1941 together with Manfred von Ardenne who is the inventor of transmission electron microscopy. In their report, they prove that the new material consists of chains of spherical carbon.[27] Later reports always show the existence of carbon nanotubes with electron microscopy, which shows that this fundamental visual technique opened insights into nanostructured graphitic carbon allotropes.
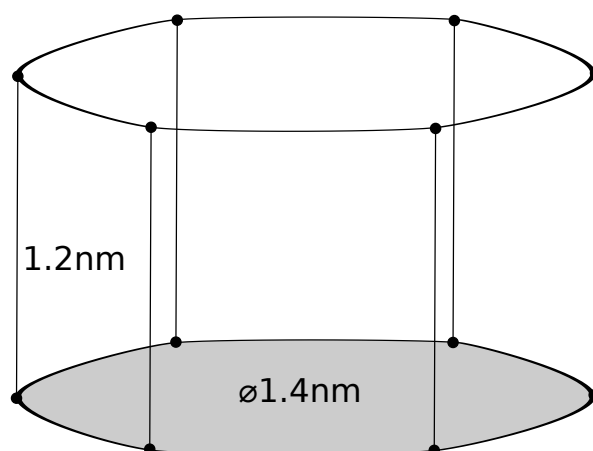
Fig. 2: A prismatic hexagonal unit cell with rounded edges as proposed by Hofmann et al. in 1932 is close to what we see as a nanotube today.
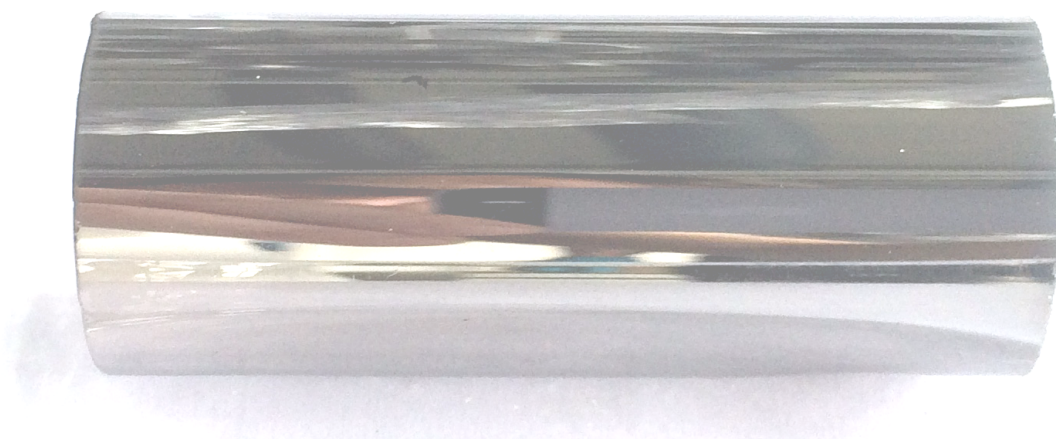

Fig. 3: The picture shows a quartz substrate covered with Hofmann's "Glanzkohle" (lustrous carbon) [22] synthesized by chemical vapor deposition of toluene at 1000°C.

2.1.2 1950

As stated by Montieux[28], there had been earlier reports on the production of carbon filaments back unto 1889 but the main credit for "the discovery of carbon nanotubes" should go to Radushkevich and Lukyanovich [29] who published a series of rather detailed electron microscopy images in 1952. Regarding the research on the synthesis conditions, though, they cite some of the earlier German articles but not necessarily the relevant ones.

Although there had been previous reports [30], the first correct analysis for the growth conditions of carbon nanotubes in English speaking literature had been carried out in 1953 by W.R. Davis, R.J. Slawson, and G.R. Rigby [31]. Working for the British Research Association, they were intentionally investigating the disintegration of bricks in blast furnaces. In their report on a "minute vermicular [form of carbon]", they correctly identified iron as the catalyst, carbon monoxide as the carbon source, and high temperatures (>450°C) for the growth of carbon nanotubes. At the time of writing, the research of Davis et al. was state of the art in electron microscopy working at the resolution limit of 10nm. Within the short report, they also suggested a growth mechanism that holds until today: They found that the catalyst particles are located at the end of the growing nanotubes and successive bundling takes place in the bulk raw material. Even though they underestimated the growth temperature by at least 150°C, this report is overly astonishing from today's point of view as it identifies all necessary conditions for the synthesis of carbon nanotubes.

2.1.3 1960

How important the use of an electron microscope was, shows the first synthesis of carbon structures via chemical vapor deposition in 1959 [32]. Although, Walker et al. measured surface area and crystal structure, they were not able to report on nanostructures most likely due to the missing availability of microscopic methods.

In 1960 Roger Bacon carried out the first comprehensive analysis on carbon filaments.[33] In his publication he collects different growth temperatures (350-1000°C) and extends the list of valuable catalysts to iron, cobalt, and nickel. Bacon uses arc-discharge on a graphitic electrode as a synthesis method with defined growth control. His key finding is the confirmation of the bent graphitic nature of the carbon lattice by Bragg diffraction. Due to their high length to diameter ratio, he named the filaments "Graphite Whiskers". When describing the raw aggregated carbon nanotubes, he referred to "bundle[s] of Christmas tinsel". In his attempt to explain the high resistivity against strain, he introduces a scroll-like structure. The carbon nanotubes should be rolled in a continuous helical spiral
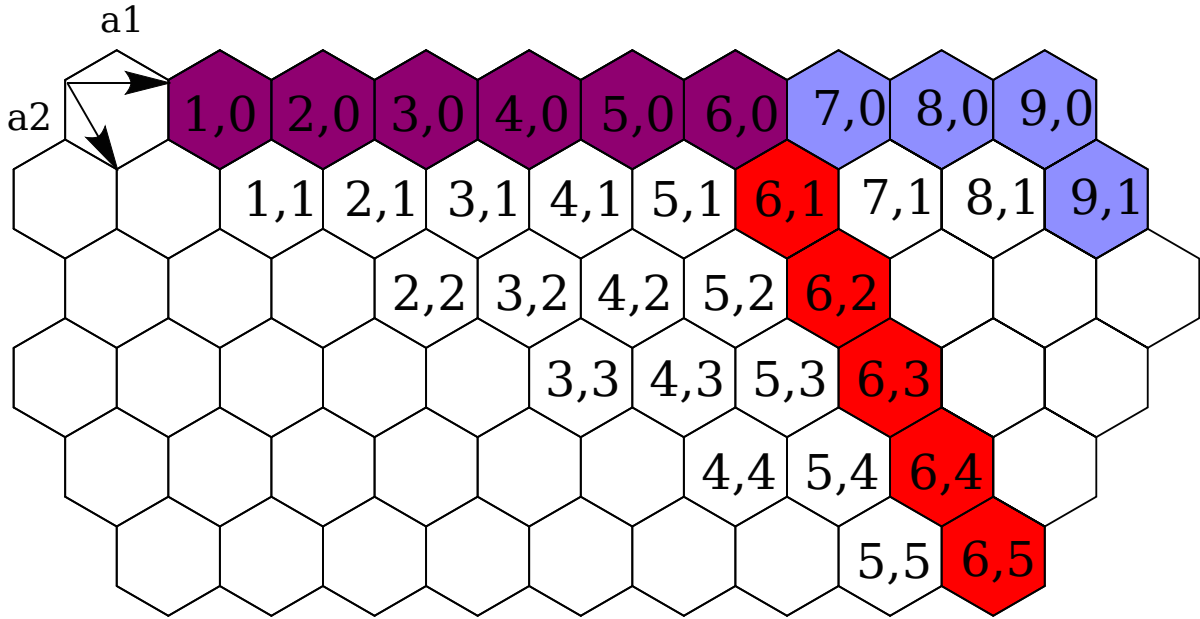
Fig. 4: Carbon Nanotubes consist of a graphitic hexagonal lattice. Its unit cell is extended along the two hexagonal unit vectors to form a cylindircal object. The picture shows the extension of the unit cell vectors $6 \cdot \vec{a_1} + 5 \cdot \vec{a_2}$ which is called a (6,5) carbon nanotube in the commonly used Dresselhaus notation.

rather than in discrete cylinders.

Based on our knowledge today, these early publications were describing large bundles of carbon nanotubes, largely overestimating the diameter by one to five orders of magnitude. Nevertheless, those discoveries of a nano-scaled world are overly astonishing as the first electron microscope was constructed only 20 years before this discovery by Ruska at Siemens [26]. Despite the presence of suitable microscopic techniques and the knowledge about the proper synthesis conditions, research on carbon nanotubes became stale until the beginning of the early 1990s.

2.1.4 1990

Initially, the arc-discharge technique was used for the synthesis of C60 fullerenes in the middle of the 1980s [34]. This look into graphitic carbon nanostructures also revived research on carbon nanotubes: In the year 1991, Sumio Iijima described "needle-like" "microtubules"[35] as by-products during the synthesis of fullerenes. Using X-ray diffraction, he confirmed the previously mentioned findings by Bacon that the underlying hexagonal graphene lattice is indeed helically rolled up at a certain angle to the tube axis. In his attempt to confirm Bacon's scroll model, he searched for overlapping edges at the outer surface of the "carbon needles" using transmission electron microscopy. As he was not able to find those features, he suggested concentric cylinders. Each tube should have spiral growth steps at the beginning and end similar to screw dislocations in a planar
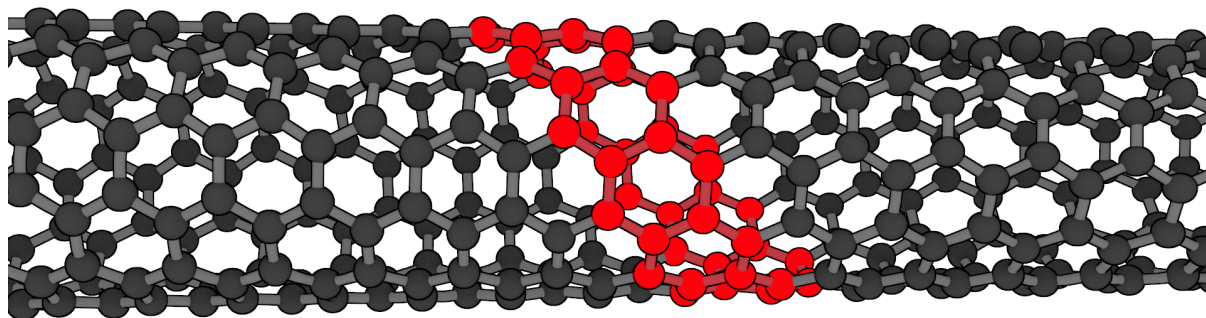
Fig. 5: Rolling the graphene unit cell at an angle of 27° to the unit vector forms a (6,5) carbon nanotube.
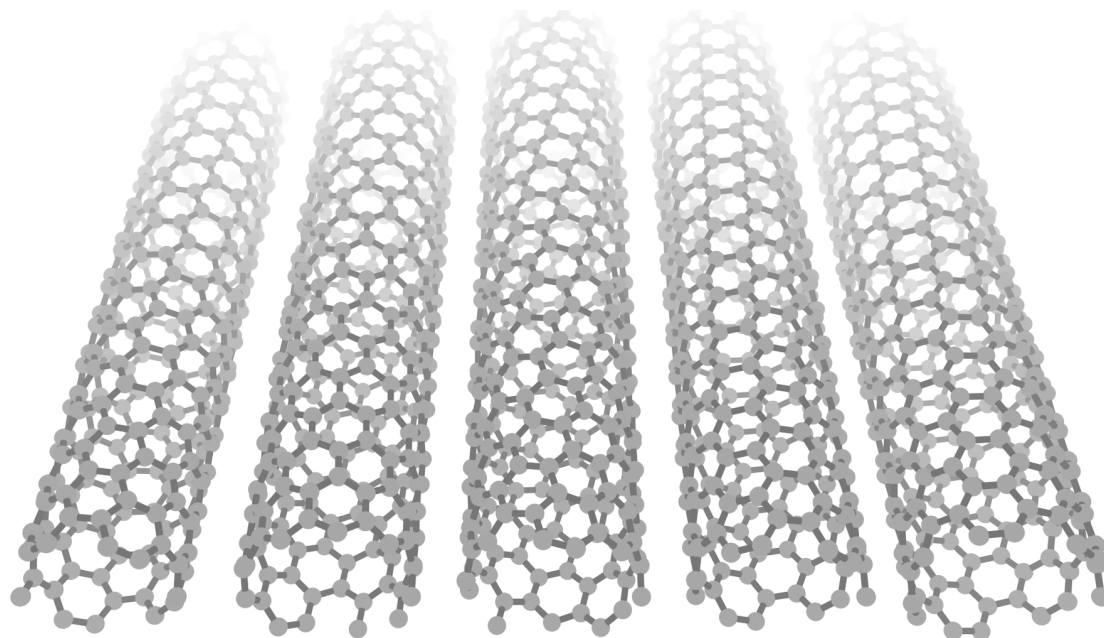
Fig. 6: The (n,m) descriptor defines the unit cell extension.
Differently rolled carbon nanotubes with increasing diameters from 0.7nm to 0.9nm: LTR (6,4), (9,1), (8,3), (6,5), and (7,5) type.

graphene lattice. With his publication, he not only correctly described multi-wall carbon nanotubes but also introduced discrete roll-up angles and pointed out that the screw dislocation produces handed (chiral) tubes.

2.1.5 Excitons
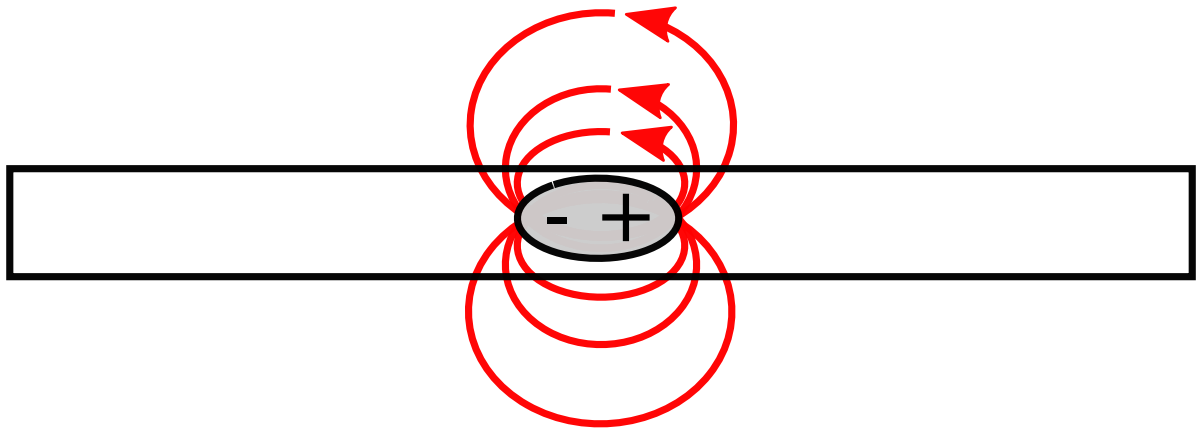
Fig. 7: The charge-separated net-neutral state of an electron and a hole binds through quantum mechanical forces and forms quasi-particles that are called excitons.

Although the carbon nanotubes described in this initial report were multi-wall due to typical synthesis temperatures of 4000°C, it was readily after recognized by Riichiro Saito that single-wall carbon nanotubes of the described cylindrical structure would have unique electrical properties.[36]

Sumio Iijima also reported the first actual synthesis of single-wall carbon nanotubes (SWNT) only two years after his initial report on multi-wall carbon nanotubes.[37] Due to their rolled symmetry, the electronic bands in SWNT accumulate at distinct energy levels, which are called van-Hove singularities. These singularities allow charge-separated states to exist. Even though the Coulomb interaction acts attractive, the quantum mechanical exchange interaction allows these systems to form a bound state. The one-dimensional confinement in the tubular structure causes binding energies of up to 500meV, which allows these quasi-particles, so-called excitons, to be stable at room temperature. Ando et al. theoretically predicted excitons [38] and in 2005 they were also experimentally confirmed using 2-photon spectroscopy [39].

2.1.6 Chiral Distribution
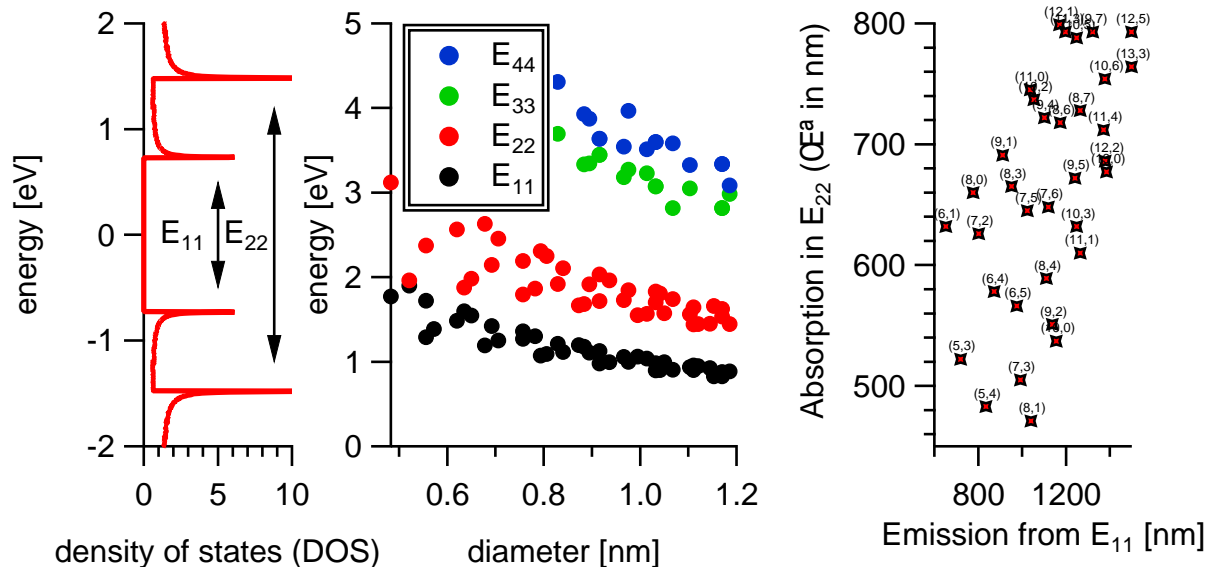
Fig. 8: Nanotubes can have the same diameter as can be seen for the (6,5) and (9,1) type, but only the roll-up angle defines their distinct electronic band structure. Plotting the diameter of a carbon nanotube against its energy separation between first and second subbands is called a Kataura plot[40].
Data for this Kataura plot was measured in air by Liu et al.[41]

More control over the synthesis process with higher yields and overall smaller diameters was first achieved in 1995 by laser ablation or laser furnace techniques.[42][43][44] There have also been routes for the deposition in plasmas generated by solar furnaces, but there is generally no need for going to such high temperatures during synthesis.[45][46] All of these techniques produce bundles [47] and chiral distributions with a larger mean diameter. Other innovative approaches use wet chemical synthesis to construct single chiral samples from the bottom up using Scholl reaction or aryl-aryl domino coupling.[48][49][50] A more cost-effective production environment that gives good control over the diameter distribution and also allows up-scaling to commercial production grades[51] is chemical vapor deposition.

2.1.7 Conclusion

Without going into more detail of the early advances in carbon nanotube synthesis, it should be clear by now that it is crucial to control both synthesis and analysis methods to investigate a new material properly. In the following chapter I want to concentrate on chemical vapor deposition as the preferred synthesis technique in this study to create samples of single-wall carbon nanotubes with diameters between 0.7 and 0.9nm and a length of 2μm and more on different substrates. Advances in optical techniques also allow doing more thorough analyses than what is possible with electron microscopy. The

following chapters will introduce the synthesis technique to produce the samples and the principal optical characterization methods for taking images and spectra.

2.2 Chemical Vapor Deposition
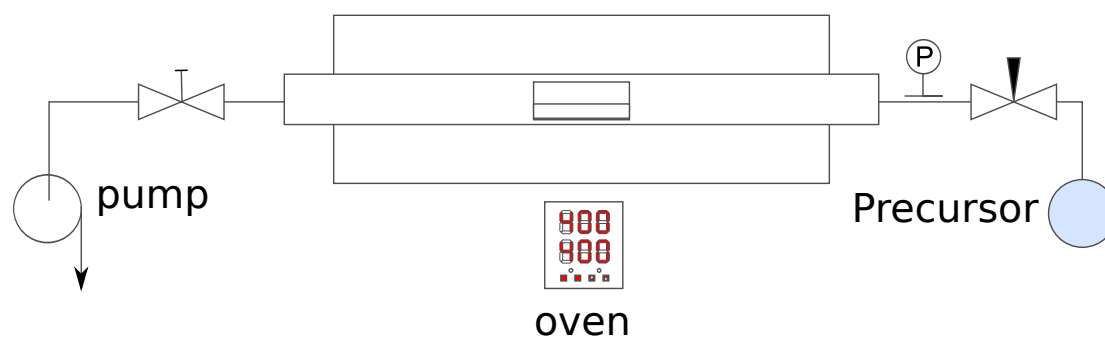
Fig. 9: The general CVD process consists of a carbon precursor and a reaction chamber with typically higher temperatures. A pump directs the precursor flow from the right to the left and controls the pressure.

2.2.1 Technique

Upon all synthesis techniques, chemical vapor deposition is mostly preferred for laboratory scale production of carbon nanotubes. The technique allows synthesis in a controllable environment with constant temperature, an adjustable synthesis pressure and a wide range of variability when it comes to carbon precursors. Gaseous precursors include carbon monoxide[52], methane[53][54] or ethene[55] and various liquid precursors like xylene [56], camphor [57] or benzene [58], or ethanol [2]. In all synthesis routes, metal catalysts are used. While in the early beginnings, only iron, cobalt, and nickel were confirmed to catalyze carbon nanotube growth, CVD has since then shown to apply on a large variety of metals:

Pb [59], Sn, Mg, Al, Cr [60], W [61], Mn [60][62][63], Fe [51][2][64][60][65][61], Co [53][2][66][64][60][61][67], Ni [68][53][43][69][60][70], Cu [71][60][72][67], Mo [52][43][66][60][67], Ru [73], Rh [43][74], Pd [43][60], Pt [43][60][75], and Au [76][60]

Most catalysts today are combinations of different metals as co-alloy catalysts. Although iron and cobalt play a significant role as catalysts, almost all combinations are possible.

Its generally low yield as compared to continuous installations like the commercial HipCo material contrasts to the overall good quality giving carbon nanotubes with fewer lattice defects and higher quantum yields [78]. Single tube lengths of around 5μm are a common
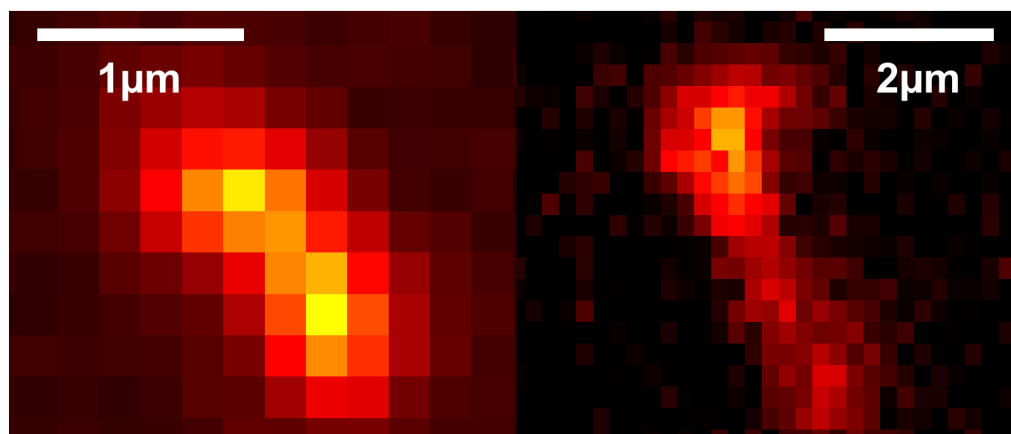
Fig. 10: Even unprocessed, raw CoMoCat material[77] like the black sand material (left image) shows overall smaller tube length than the CVD material (right image).

result of an unoptimized procedure, which contrasts the 200nm length of the commercially available CoMoCat material[77]. Optimized Processes have even shown that nanotubes from sub-millimeter[79] up to 4cm[65][80] length and more are achievable.

2.2.2 Reactor
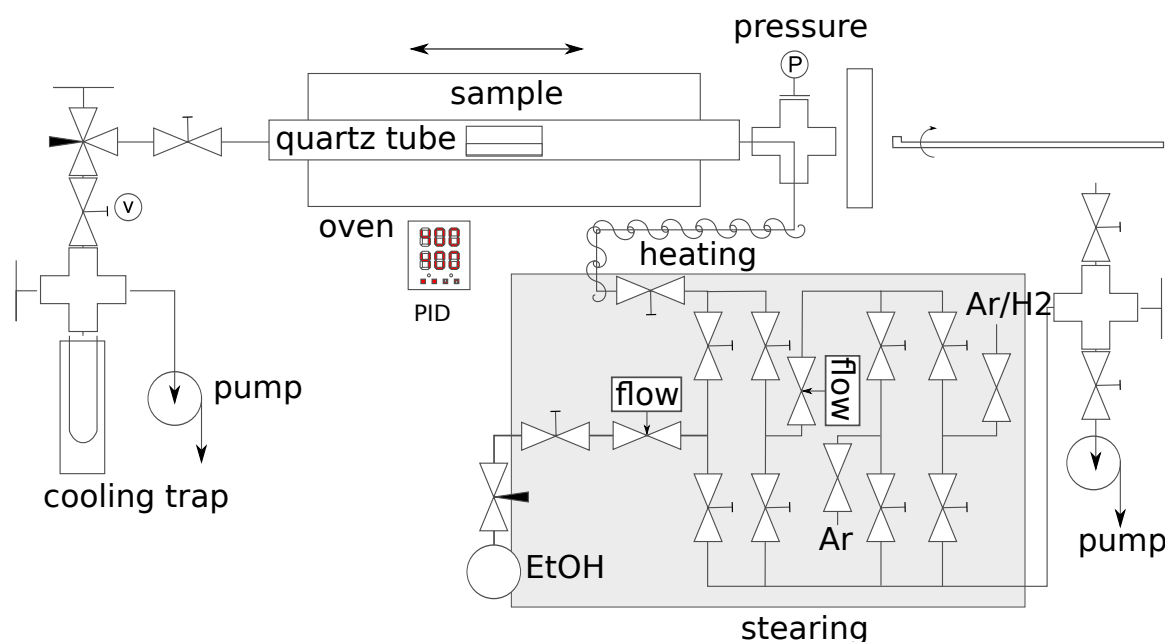
Fig. 11: The setup for Chemical Vapor Deposition from the presented study allows low-pressure CVD, rapid cooldown, and exchange of gas sources during a reaction.

The reaction chamber in the presented study consists of an oven that heats the sample for the reaction. The reaction chamber needs to stay evacuated during the whole CVD

process to avoid reactions of the produced carbon nanotubes with oxygen which increases hetero atom defects in the graphene lattice.[81][82]

Due to reaction temperatures of 800°C and more and temperature jumps of around 100°C per minute, the reaction chamber consists out of quartz, which easily withstands such conditions. A PID controller adjusts the reaction temperature to a value measured at the center of the oven. It is, therefore, crucial to place the sample in the middle of the quartz tube. The oven is placed on rails to allow the proper positioning of the sample. This approach also reduces cooldown time as the oven can be quickly get moved away from the sample and therefore allows laboratory-scale mass production of carbon nanotubes as heat-up is the limiting time factor during synthesis.

The pump evacuates the chamber from the left, and any potentially toxic reaction by-products remain in the cooling trap. A needle valve controls the pressure between the pump and the reaction chamber and allows an exact adjustment of the pressure during synthesis. Additional argon flow as a carrier gas allows increasing the pressure during the reaction. The gas sources are exchangeable, but argon and argon with 3% hydrogen are pre-installed to the system.

The most important part of the reaction is the carbon source, which is plugged in with a glass flask and can hold pre-evacuated solvents. A water bath helps to adjust the vapor pressure, and a needle ventile right after the flask controls the maximum exhaust from the source. A digital flow meter is installed to control precursor inflow. The exchangeable flask and programmable flow meter allow a wide range of carbon sources with vapor pressures of up to around 100mbar.

Nearly all carbon sources that were tested with this setup allow synthesis of carbon nanotubes of fairly small diameters (<1nm). Among the tested carbon sources were methanol, ethanol, n-propanol, i-propanol, butanol, toluene, o-xylene, and p-xylene. Tested hetero-atom carbon sources include acetonitrile, triphenylborane, and triisopropylborate. This large variety of precursors probably also explains the aforementioned early discovery of carbon nanotube synthesis using vastly undefined carbon precursors and metal catalysts.

Due to the chosen setup with a cooling trap, glass flask, and a quartz tube, it is easily cleanable and usable even if potentially toxic, and volatile reaction intermediates are likely to form. The advantage as compared to pure-gas-flow setups is also the low risk of combustion of common gaseous carbon precursors like acetylene.

Fig. 12: The Chemical Vapor Deposition Reactor consists of an oven in the center of the image and a gas control with different inlets on the right. The pump at the left can achieve constant flow synthesis at 10mbar. The quartz tube connects the gas inlet and pump and allows temperatures of 800°C.

2.2.3 Alcohol Catalytic CVD

Shigeo Maruyama and Shohei Chiashi introduced alcohol catalytic chemical vapor deposition (ACCVD) for the synthesis of semiconducting single-wall carbon nanotubes at the University of Tokyo in 2002.[2] Today, typically ethanol is used as a precursor in this synthesis route for carbon nanotubes. The carbon nanotube community readily accepted this technique due to its simplicity of the setup and its generally secure handling and a-toxic impact of the carbon precursor to western haplotypes[83] if compared to conventional alternatives like toluene or acetylene.

Despite its complexity when it comes to the growth mechanism itself, the combustion into reactive precursors is well studied and understood using theoretical investigations.[84] The liquid combustion product of the ACCVD process is mainly acetaldehyde.[85] More elaborate in-situ monitoring of the reactive intermediates via infrared spectroscopy shows that "ethanol decomposes within 3min and generates ethylene, acetylene, acetaldehyde, methane, carbon monoxide, carbon dioxide, and water"[79]. ^{13}C labeling has shown that ethanol reaches the reaction center without splitting into symmetric intermediates like acetylene or ethene. Instead, only the methylic carbon opposite to the hydroxyl group in ethanol is incorporated into the nanotube lattice.[86] Therefore, the reactive asymmetric species of the ethanol combustion process are C-C-OH and C-C-O.[87]. Molecular dynamics simulation studies typically underline the insights into the actual growth process.[88][89]

Not only the mechanism but also the growth conditions are widely understood: There is a close relationship between pressure and synthesis temperature for (A)CCVD which is usually reflected by a phase diagram that relates temperature, pressure, and quality of the synthesized material.[90][4] Hou et al. showed that the temperature for the synthesis of carbon nanotubes using ACCVD ranges between 350 and 1000°C with a pressure of 10mPa to 10kPa. Such a wide growth range lets the author assume that carbon nanotubes are likely to form during every carbon combustion process that involves metal catalysts. Despite this wide range of acceptable growth conditions, a material with lower defects is typically produced from ACCVD at 750-850°C with a pressure of 0.1 to 100mbar. Lower pressure is only needed when lowering the synthesis temperature. No-flow techniques [79], where the ethanol flow is turned off during the reaction, allow to achieve lower pressures. While lower temperatures give access to the synthesis of single-wall carbon nanotubes with diameters below 0.8nm, lower temperatures generally also lead to lower sample quality.[78] Smaller diameters grow kinetically at lower temperatures and become thermodynamically unstable at higher temperatures[64] due to their curvature[91][81][92][93]. Therefore, amorphous carbon and defective nanotubes are only avoidable by raising the synthesis temperature.[92][94][90]
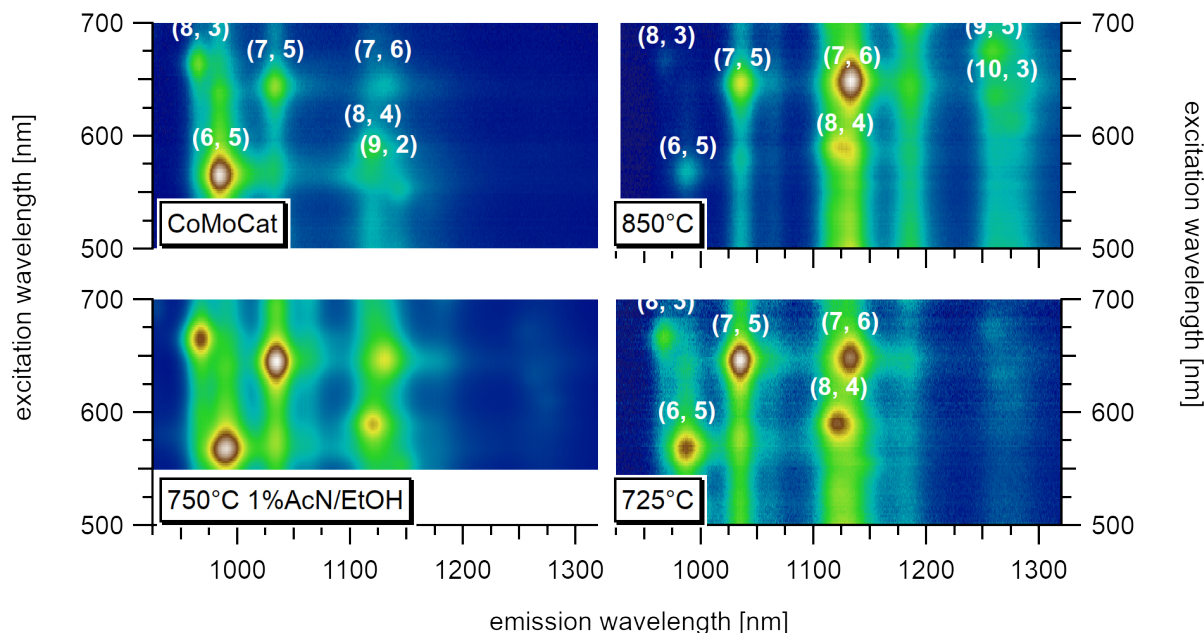
Fig. 13: A comparison between commercial CoMoCat Material and as-synthesized CVD material for different synthesis strategies shows the difference in the chirality distribution. The commercial material is post-processed after synthesis to achieve high enrichment in the (6,5) type. It is extensively studied and serves as a reference.

Within a constant flow setup like the one presented in this study, the precursor flow mostly determines the minimal achievable reaction pressure. The lower limit of this pressure is at 1-5mbar, and a typical reaction was therefore carried out at 800°C with a pressure between 5 and 15mbar in a constant ethanol flow environment of 80-300mg/min. At constant pressure, the flow does not play any significant role for reaction times of 10min and below.[85][79]

Notable for the chosen synthesis route is that even though a typical reaction finishes after around 1min, it was carried out for 10min in all experiments to facilitate defect healing due to the reductive properties of combusted ethanol.[95][79][84][87]

The high-temperature trade-off with this setup yields both, good quality and diameters that are in the range of the silicon detector's quantum efficiency. If low defects and nanotubes between 0.8 and 1.2nm are the preferred synthesis target, these conditions have proven to be best for our CVD setup without the complications that emerge from going to lower pressures.

2.3 Growth on Substrate

The synthesis via CCVD was accomplished using two different general synthesis techniques [2][74] that can be differentiated by the substrate on which the catalyst was deposited. The synthesis on zeolite was primarily used for convenient large-scale production and individualization using wet post-processing methods. The Synthesis on wafers was used to directly yield individualized nanotubes of high quality for microscopic investigations and single-molecule measurements. The diameter distribution in both methods is similar.[96]

2.3.1 Zeolite
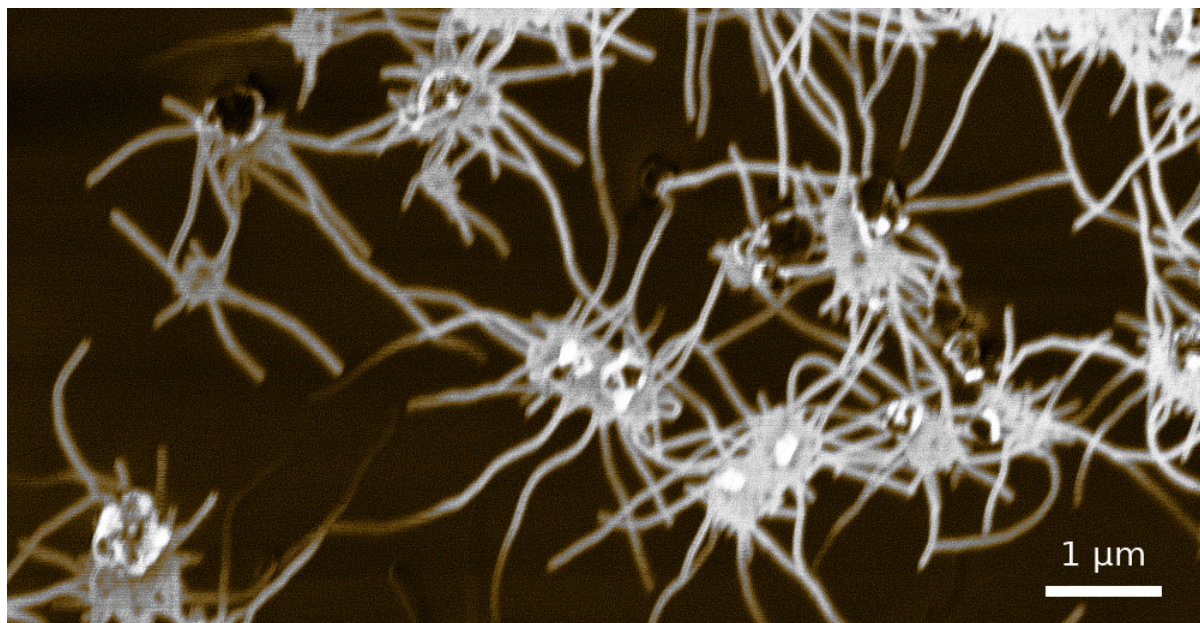
Fig. 14: Spider-like growth of carbon nanotubes on zeolite FAU 111 using the Maruyama approach. Cavities in the zeolite substrate isolate and direct the growth of single-wall carbon nanotubes. The as-grown carbon nanotubes directly allow further wet-processing.

A conventional way for the synthesis of carbon nanotubes via ACCVD is the usage of zeolite as a substrate. These alumno silicates accept metal catalyst particles to their microporous structure. The pores of zeolite Y are 0.74nm in diameter and act as a mold for carbon nanotubes with a similar diameter.

In the presented experiments, Cobalt co-alloy catalysts in concentrations of 0.5mol metal per gram zeolite Y were prepared. For the growth on zeolite, there was no notable difference between different combinations with Fe, Cu, and Rh on zeolite at 800°C. The diameter distribution only slightly varies at lower synthesis temperatures. For measures of toxicity and cost, Iron-Cobalt has shown to give the best results at 800°C[2][78] and Copper-Cobalt when synthesizing at lower temperatures[67]. As Copper has a lower
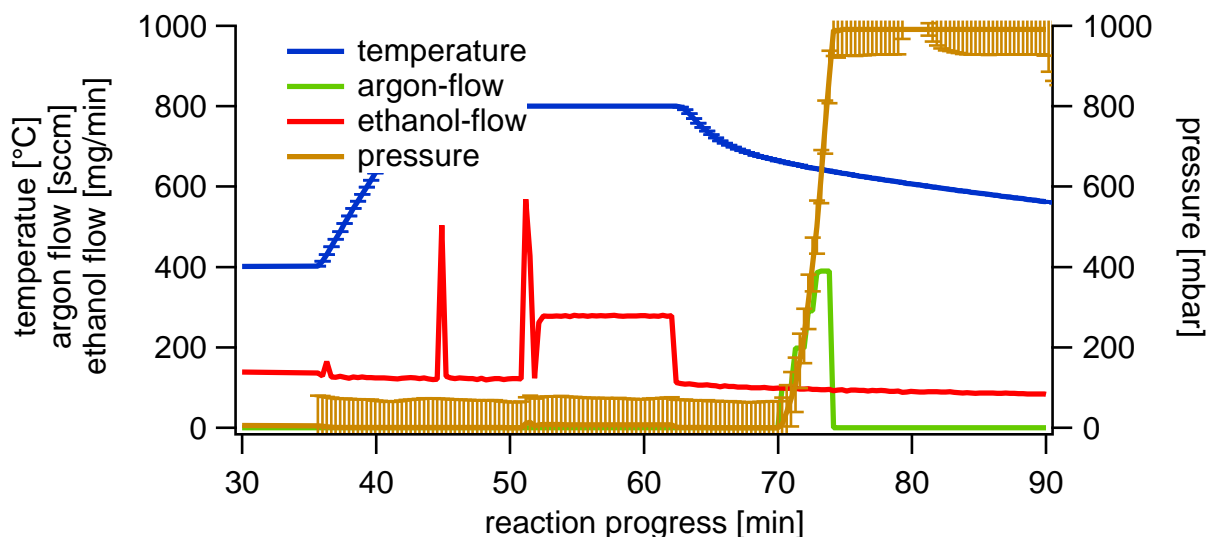
Fig. 15: The figure shows the variation of temperature, pressure, and precursor as a function of the reaction time for a typical ACCVD process. The reaction is carried out at a temperature of 750°C and a pressure of 15mbar.

melting point than Iron, exchanging Iron against Copper shows coalescence to smaller cobalt nanoparticles [67]. These particles are then anchored during Oswalt ripening to their Metal-Co-Alloy.

Wet processing of the as-grown zeolite raw material allows for an easy investigation of the sample quality and chiral distribution in a cuvette without the need for statistical methods that arises from single-molecule spectroscopy. Within one measurement the sample can be nearly fully characterized in its chiral distribution.

An absorption spectrum is not sufficient for characterizing the chiral distribution of a sample. Some chiralities have overlapping absorption with other chiralities in their excitonic transitions in E_{22} or E_{11}. For instance, the absorption spectrum of the (7,6) type overlaps with the E_{22} transition of the (7,5) type and with the E_{11} transition of the (8,4) type. This overlap is better visible in the second derivative, but such a chiral mixture makes distinct identification of the sample composition impossible using absorption spectroscopy solely.

A distinct identification of these chiralities is possible using, Photoluminescence Excitation (PLE) Spectroscopy which was introduced by O'Connel et al. in 2002.[97] It allows the exact and distinct identification of all optically active chiralities. This technique is overly important to identify the chirality in varying dielectric environments which is otherwise subject to rough guesses when identifying the chirality during the adsorption of solvent molecules to carbon nanotubes.

However, the de-bundling of the carbon nanotube arrays grown on the zeolite substrate requires the use of rather high force typically applied using shear mixing or sonication
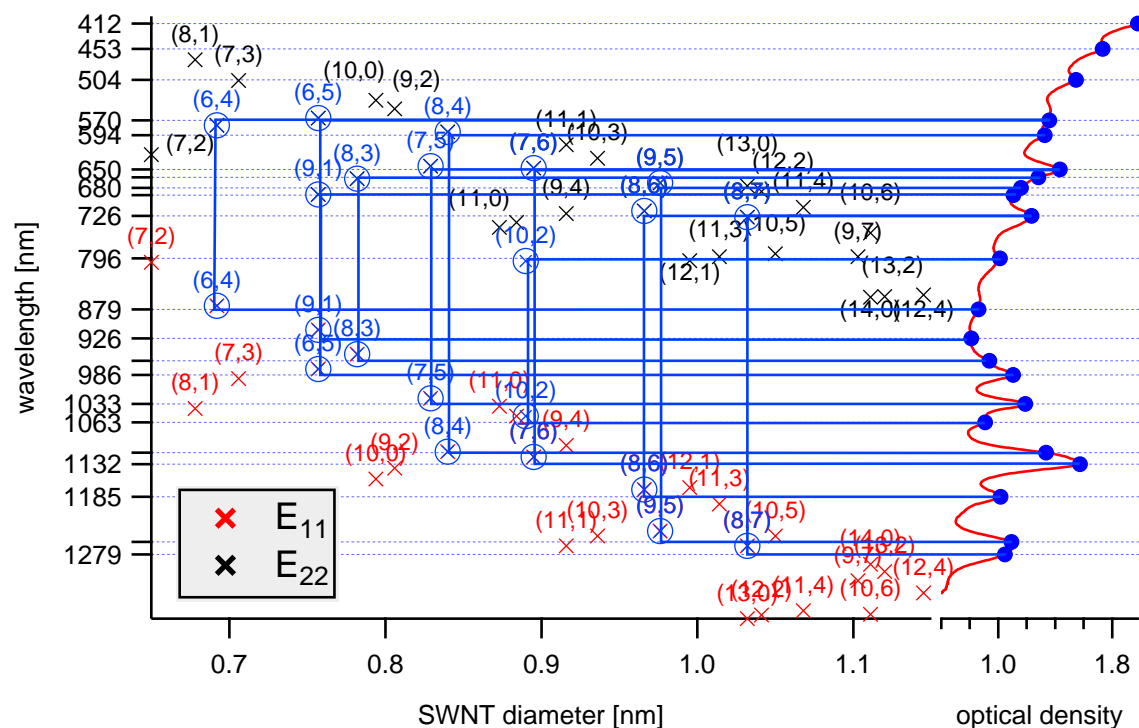
Fig. 16: The figure shows an absorption spectrum (right) of a typical sample synthesized from FeCo catalyst on zeolite Y with corresponding Kataura plot (left) and connections of the first and second excitonic subbands. The ACCVD process gives diameters at about the pore size of the used zeolite material.
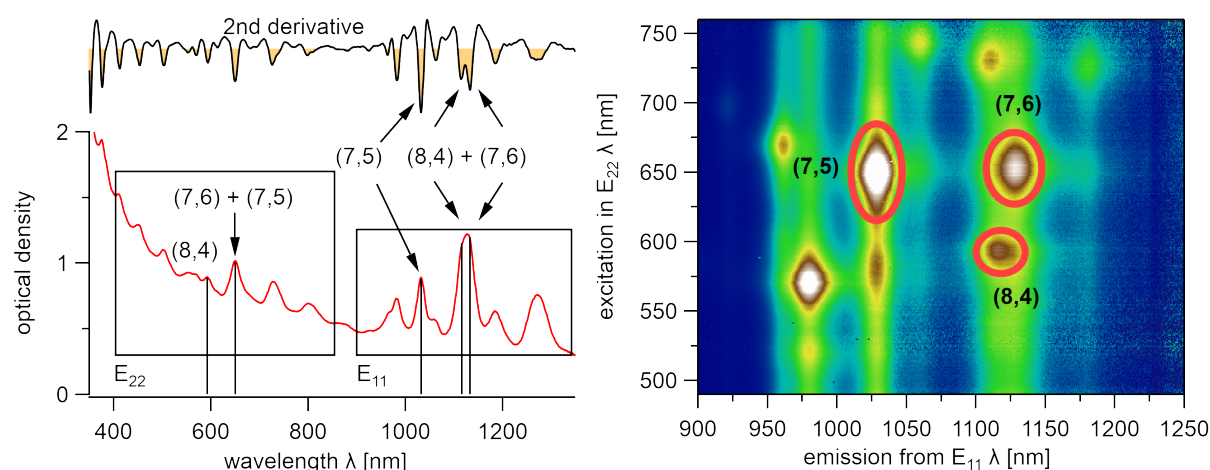
Fig. 17: The (8,4) and (7,6) type exhibit the same excitonic absorption energy in their E_{22} state but differ in their E_{11} state. However, the (7,6), (7,5), and (8,4) type are clearly identified using PLE spectroscopy. The nanotubes were dispersed with 1.5wt% DOC in water.

and surfactants to prevent subsequent bundling.

2.3.2 Wafer
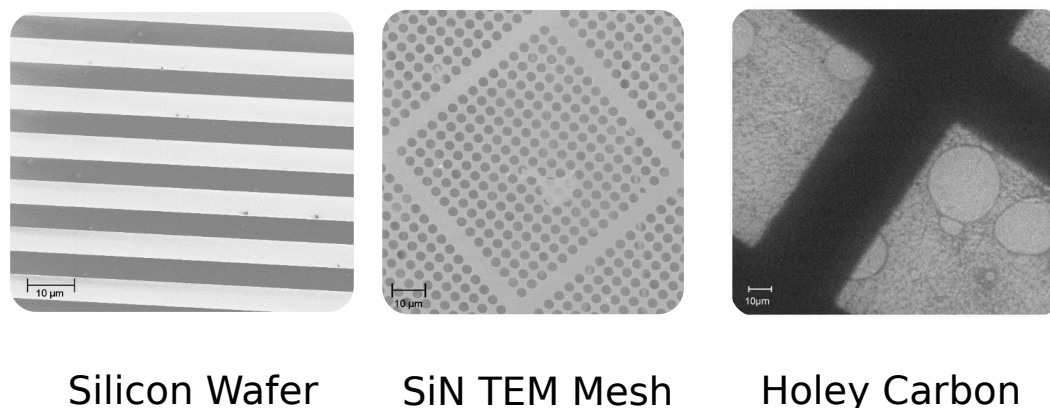
Fig. 18: Different substrates for growing carbon nanotubes freely suspended over trenches: Silicon wafers, Silicon Nitride membranes, and holey Carbon grids. The latter two are typically used in TEM

The synthesis and analysis of carbon nanotubes on a substrate is a more demanding task than the synthesis on zeolite substrates with subsequent wet processing.

Grids for transmission electron microscopy have good commercial availability and the needed porous structure for suspending nanotubes. In short, holey and lacey carbon grids could not withstand the synthesis temperature during the growth process. SiN grids, on the other hand, have shown good results but could not stand the mechanical forces applied during the experiments. These grids, however, are ideal for testing the microscopic setup due to their inherent absence of background emission. In the following experiments, all single molecular measurements were performed with the thermally and mechanically stable, silicon wafers[98][85].

The synthesis on silicon wafers needs similar growth conditions as on zeolite. However, the lack of a predefined catalyst mold requires a slightly modified synthesis route for the catalyst preparation.

The procedure follows a slightly customized variant of the route described by Thurakit-seree et al.[74]. In a typical process, the substrate surface was subsequently cleaned using sonication in acetone, isopropanol, and ethanol. It is then dip-coated into 0.5mM cobalt acetate in ethanol and annealed in air at 400°C. After cooling to room temperature, the co-alloy metal solution with equal molarity was added, repeating the described steps.
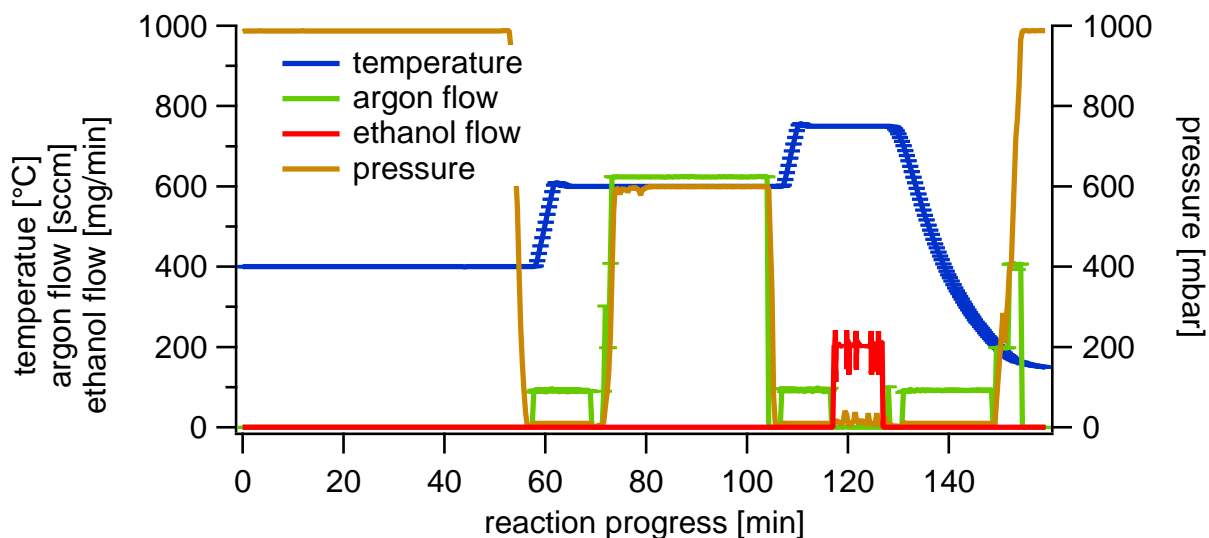
Fig. 19: The synthesis on flat substrates is carried out with an additional reduction step where hydrogen is used to reduce catalyst particles to facilitate carbon nanotube growth.
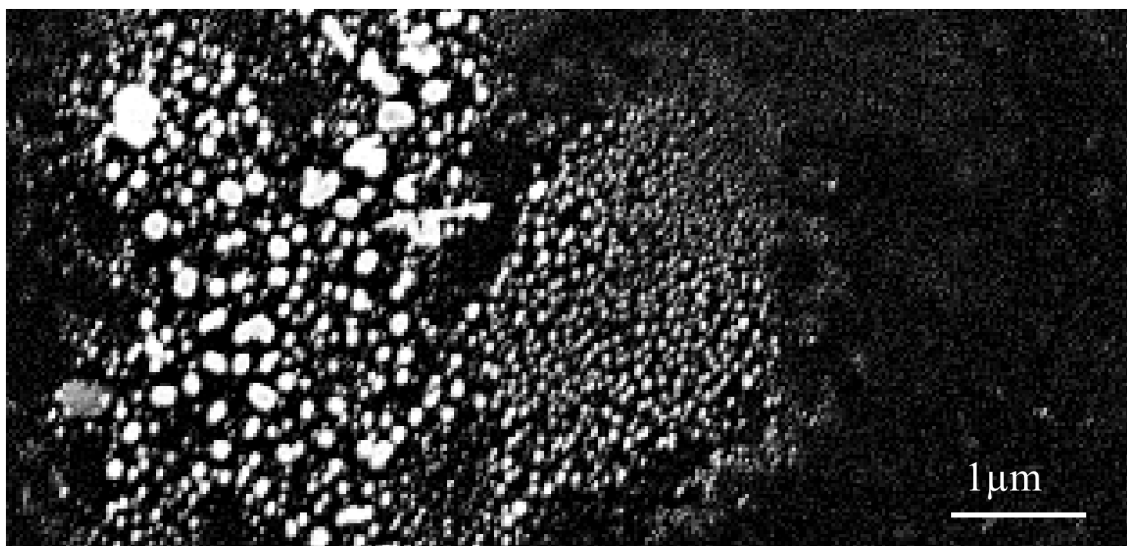
Fig. 20: Co-Rh catalyst particles on a silicon substrate after Oswalt ripening under a hydrogen atmosphere at 600°C. The picture shows a spot with a large variety of particle diameters. Due to the high catalyst density in this area, Oswalt ripening is producing particles up to 200nm in diameter.

For the formation of catalyst particles with a defined diameter, the coated catalyst is annealed in a reductive argon atmosphere with 3% hydrogen at 600°C for 30min. This step facilitates Oswalt ripening and isolates metal catalyst islands on the substrate and forms cobalt silicide [99][100] on silicon substrates. The size of these particles is considered to be of superior importance as they serve as templates for the nanotube growth.
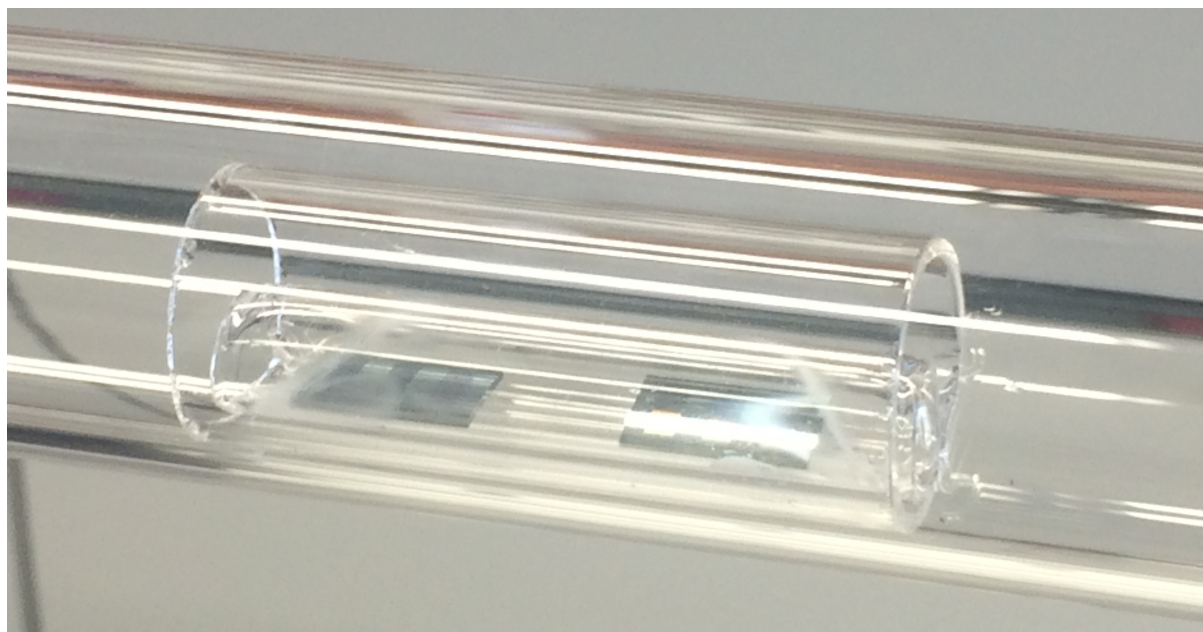
Fig. 21: The picture shows the quartz boat with two loaded wafer samples inside the reaction chamber. The oven is placed on rails and can be pulled away for the exact positioning of the sample in the center of the oven.

The reaction chamber is then evacuated and heated to 800°C, where 100mg/min ethanol is introduced for 10min at 8mbar. After the reaction, the sample is cooled to room temperature and kept in a dust-free environment.

Catalyst coating plays a superior role during this process. Since the catalyst is deposited at arbitrary positions on the sample via dip coating, the procedure was lacking reproducibility. In an attempt to compare the chiral distribution of the produced samples, the coated wafers were sonicated in aqueous deoxycholate solution and analyzed using photoluminescence emission spectroscopy while comparable quantum yields for all metals had to be assumed. The chiral distribution slightly varies for different co-alloy metals of cobalt with molybdenum, manganese, iron, copper, or zinc. Chiralities synthesized from Mo and Mn generally show the highest emission. The samples with Fe and Rh as cobalt co-alloy metals have a more homogeneous chiral distribution but are generally also 80% lower in their emission strength and thus their estimated nanotube yield. Cu and Zn did not give good results.[96] Following these results, the following study only uses iron, molybdenum, and rhodium as cobalt co-alloy catalysts for the synthesis of suspended carbon nanotubes at 800°C.

2.4 Spectroscopy

This chapter is a collection of instruments and analysis techniques used throughout the thesis. The sample preparation and synthesis were described previously and the diameter reduction with nitrogen poisoning during synthesis is described afterwards. The setup for taking spectra and images is described in more detail after the introduction of these basic methods here. All methods serve the investigations on Surface Adsorption on carbon nanotubes.

2.4.1 Wet Dispersion

If not stated otherwise, aqueous samples were debundled using Deoxycholate (DOC).[101] Typically 50mg of the raw CCVD material was dispersed in 10ml aqueous solution containing 1.5wt.% DOC. Water was purified with a millipore filter. Samples were sonicated for 1h with a Branson Horn Sonicator in a 50% duty cycle and subsequently centrifuged for 3-5min with a Haereus Spatech Biofuge 15 at 14000rpm.

2.4.2 Density Gradient Ultracentrifugation

Density Gradient Ultracentrifugation (DGU) was performed using a linear density gradient [102][103] with a Beckmann Optimatm L-90K ultra centrifuge. Fractioning of the centrifuged material was achieved with a KD Scientific KDS 210 syringe pump.

2.4.3 Absorption Spectroscopy

Absorption spectroscopy was performed on a Varian Cary 5000 UV-Vis-NIR spectrophotometer. The background of the pure solution was measured as a reference before every experiment. The spectra are processed and analyzed with a custom analysis program

2.4.4 Raman Spectroscopy

Raman spectroscopy at 1064nm was done using a Nd:YAG laser together with a high resolution FT-spectrometer (Bruker IFS 120 HR coupled to a FRA-106).

Raman spectroscopy at 488nm was achieved using an Argon laser and a dichroitic mirror (520nm) coupled to an Andor Shamrock spectrometer with an Si-CCD array (Andor Newton). The grating has 300 lines/mm and a blaze wavelength at 500nm.

Raman spectroscopy at 570nm was done at a SP2500 spectrograph with a Princton Instruments Pixis 256 CCD array

2.4.5 PLE Spectroscopy

Photoluminescence excitation/emission spectroscopy and -microscopy was performed using a home-built setup. Spectra were acquired with a LabVIEW program. It is based on a similar setup [104] that was taken for taking PLE maps in solution. The generated spectra and images are loaded and processed with a Igor Pro program for loading measured data.

2.5 Data Processing

2.5.1 Statistical Analysis

Statistical analysis, data preparation, and extraction was performed with a custom Igor Pro program for mass analysis.

2.5.2 Data Export

Data export was performed on continuous integration installations using docker containers with an automated Igor Pro pipeline. All graphs are available online as Igor Experiment (pxp) files in their complete form to perform further analyses and to extract data.

2.5.3 CVD Control

The CVD setup has a python GUI. The recording of CVD parameters was performed with an Arduino Uno and has already been decribed elsewhere [85].

The flow for various carbon sources is digitally read with the Bronkhorst flow meters using a custom python program

2.6 Nitrogen Poisoning

2.6.1 Synthesis

Introducing hetero atoms to Single-Wall Carbon Nanotubes should lead to lattice defects and a largely modified outer surface. There have also been reports on the adsorption of molecular nitrogen to the inside of carbon nanotubes during synthesis. Investigating the adsorption on such systems could shed light on the properties of these nanotubes. The material was fabricated using low-pressure CCVD and analyzed in solution and as suspended nanotubes.

The obtained results confirm the presence of heteroatoms and exciton trap states in the synthesized SWNTs but also show the limits for the applied optical analysis techniques.

NCNT (Nitrogen-doped Carbon Nanotubes) have been reported first in 1993 by Yi et al. [105] followed by more detailed investigations and review[106][107]. Ciricmarjanovic gives a thorough introduction on preparation techniques, varying structure, and possible applications.[107] It should be mentioned that the functionalization of nanotubes with carboxylic groups and subsequent amidization is also called N-CNT [108] but this is not subject to this study.

NCNT can be synthesized from a wide range of organic Nitrogen-containing molecules like melanin [109][110][111], benzylamine [112][113][114], phthalocyanine [115] as well as pure acetonitrile [116]. Extending the well-established alcohol catalytic chemical vapor deposition (ACCVD), a combination of acetonitrile and ethanol was chosen in this study following the route for low-pressure CCVD described by Ayala et al.[117]. Ibrahim et al. also reported a similar route for high-pressure CCVD[118] which was adapted for synthesis between 750°C and 850°C at 12mbar using either bimetallic Rh-Co catalysts [74] on silicon substrate or Fe-Co catalysts on zeolite [2] as the process is considered to be independent of the substrate[5].

2.6.2 Diameter Reduction

The most prominent observation when synthesizing NCNT via the acetonitrile ACCVD route is the severe diameter change. Adding acetonitrile reduces the amount of larger diameter chiralities and even enhances the growth of smaller diameters.

The change is first visible when adding concentrations of 1vol.% acetonitrile to the ethanol precursor and gets more prominent when increasing the concentration to 5% up unto 12.5%. It is notable that at lower temperatures, the effect is more prominent even at low fractions of nitrogen in the precursor. A general explanation for this effect is that a nitrogen poisoning of the catalyst causes the observed diameter reduction.[5][119] This is similar to reports on a chirality dependence when mixing Nitrogen-containing molecules to the carbon feedstock.[118][109][110][110]

In addition to the diameter change, the amount of amorphous carbon (measured by the optical density of the samples at 450nm) is significantly reduced, leaving nearly transparent solutions while the typical ACCVD product is black due to the high absorption when dissolved in aqueous 1wt.% Deoxycholate (DOC). A similar decrease is visible when mixing triphenylborane to a toluene carbon source.

Energy-dispersive X-ray spectroscopy (EDX) was carried out to determine the elemental composition of the material. The analysis of the unprocessed raw material shows a direct
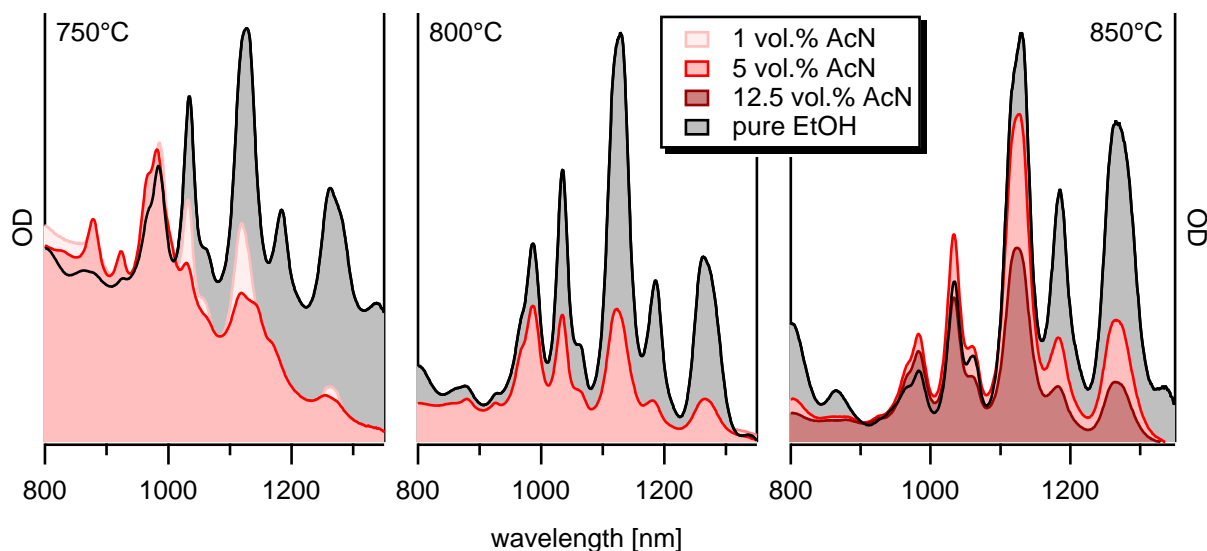
Fig. 22: Acetonitrile in the carbon precursor of the ACCVD process reduces the amount of larger diameters significantly in the sample composition reducing the diameter distribution. The absorption for the NCNT samples is offset to match up at the (6,5) type to emphasize this effect.

correlation between the amount of nitrogen in the feedstock and the EDX signal of the raw material at 0.39keV originating from Nitrogen. The elemental composition also shows carbon from the precursor and oxygen from the zeolite catalyst. Approximately 8% of Nitrogen from the source is found again in the obtained CCVD material. Ibrahim et al. also find such near-linear relationship between nitrogen from the precursor and its incorporation in the carbonaceous material.[118]
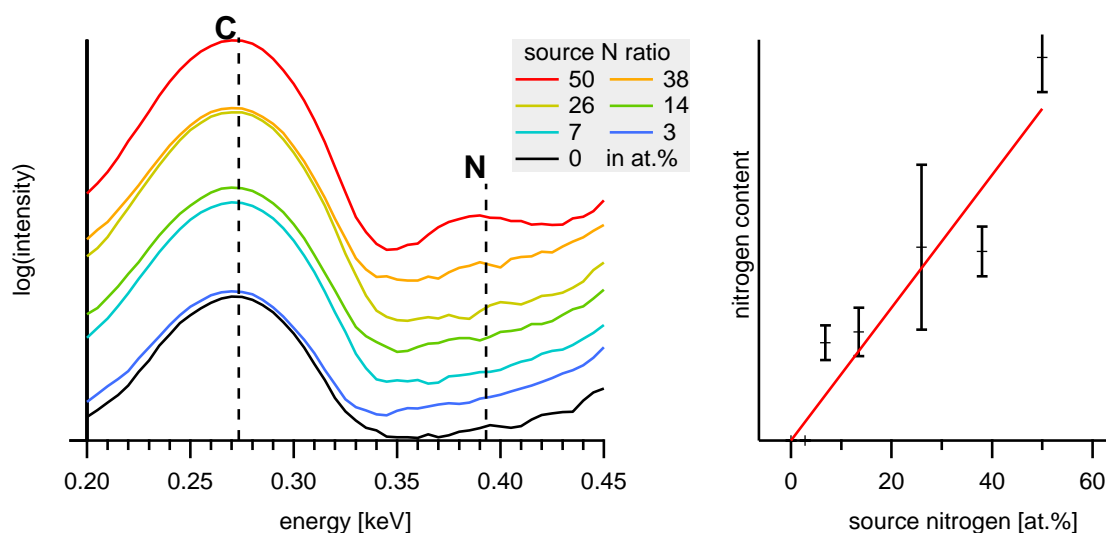
Fig. 23: A fraction of 0.6% of the initial nitrogen from the carbon source is found again in the raw material. The nitrogen content is only significantly detectable for higher nitrogen ratios.

2.6.3 Graphitic Nitrogen

NCNT can be both p and n-type semiconductors. [120][106] The two contradictory properties originate from two different bonding environments of Nitrogen in sp^2-carbon-networks: C=N-C and C-N(-C)-C. X-ray photoelectron spectroscopy (XPS) typically proves the incorporation of nitrogen into carbon nanotubes by analyzing the carbon bonding environment. Graphite-like Nitrogen bonds to three carbon atoms while the pyridinic form has only two adjacent carbon neighbors.
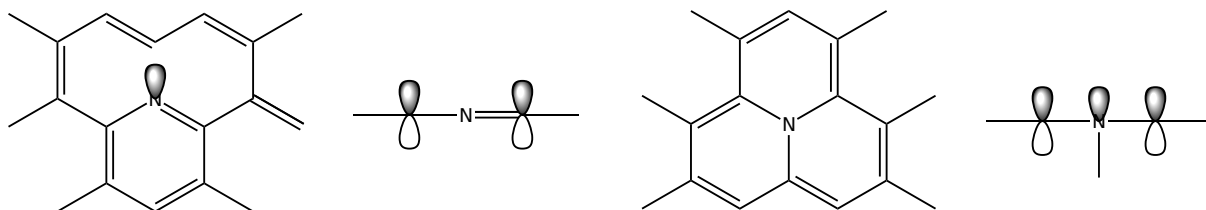
Fig. 24: In solid-state systems from sp^2 hybridized carbon, Nitrogen can be built into the carbon lattice as either graphenic or pyridinic nitrogen, respectively leading to p- or n-doped states or to combinations.

During synthesis with high pressure, graphitic Nitrogen is starting to appear between 30vol.% and 60vol.% acetonitrile in the ethanol carbon source while pyridinic Nitrogen is increasing proportionally to the total amount of nitrogen [118]. At low-pressure synthesis, a significantly higher amount of nitrogen is incorporated even at 1 vol.% acetonitrile. Graphitic nitrogen was shown to be already present at these low concentrations and is overall five times higher than pyridinic nitrogen. [5]

As stated by Krstic et al. [120], only graphitic nitrogen bonding environments generate charges in SWNT and can yield real n-type semiconductors. As the bonding environment in NCNT is known to change in acetonitrile nanotubes, electrochemical gate doping was carried out to investigate changes to the bandgap. In combination with absorption measurements, it is possible to observe the filling of the bandgap with charge carriers by observing the reduced generation of E_{11} excitons [121][122] caused by the Pauli exclusion principle.

The electrochemical measurements were performed using PFO dispersed SWNT films on ITO substrate.[123] PFO was chosen as a surfactant to narrow the diameter distribution of the poly-chiral ACCVD sample to the (7,5) type [7] and avoid energy transfer to chiralities with larger band gaps [124] like the (6,5) type. All potentials were aligned to their mid gap for visibility, and the fitted optical density was normalized to the maximum between 0.5 and 1.5V. Peaks were fitted to Gaussians. The fit of the trion peak was constrained between 1215-1250nm because of overlaps with lower bandgap chiralities, and the E_{11} absorption was allowed to be fitted between 1020-1075nm. Band gaps were calculated using the simple method described by Tanaka et al. [125] extracting the potential at
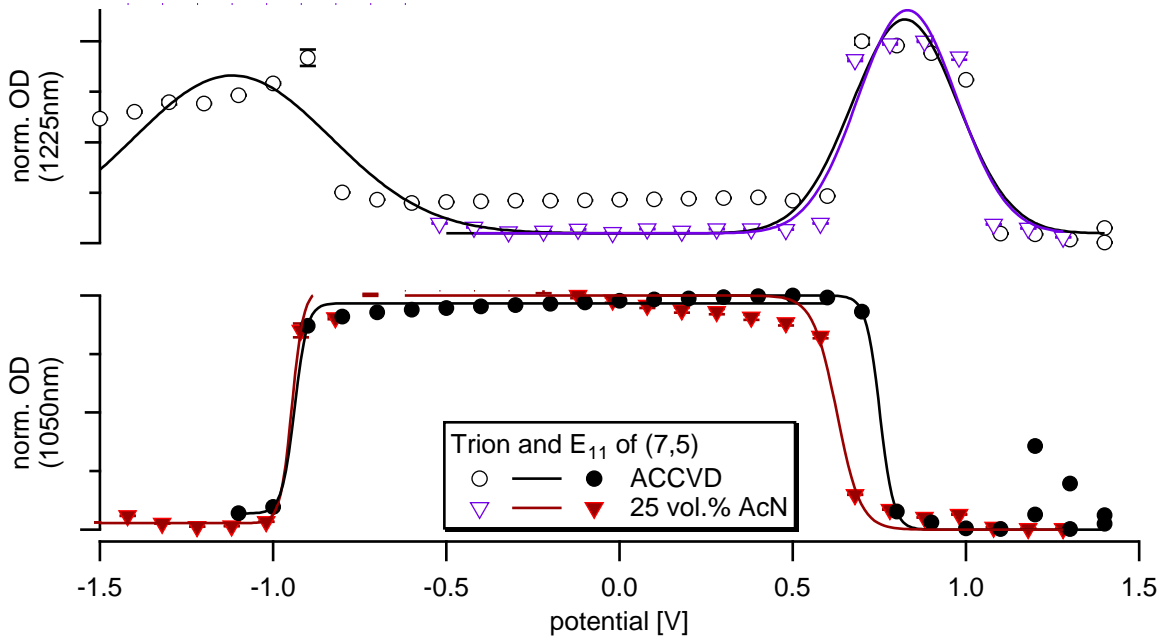
Fig. 25: Gate-doping of the (7,5) type in an NCNT sample aligned to the trion emission. Measurement by J. Heitmüller [123] on ITO films against a Pt electrode.

the point where the optical density is half-depleted utilizing the turning point of the hill equation.

	bandgap	red	ox
CoMoCat	1.79V	-1.51V	0.28V
ACCVD	1.66V	-1.34V	0.32V
1 vol.%	1.62V	-1.19V	0.44V
5 vol.%	1.77V	-1.58V	0.19V
25 vol.%	1.57V	-1.43V	0.14V

Note: Lower band gaps for the (7,5) type are typically found if the photoluminescence is measured against Ag/AgCl.

setup	method	electrode	ref	red [V]	ox [V]	gap
(7, 5)	PL	Ag/AgCl	[126]	3.97	4.98	1.01
bulk	PL	Ag/AgCl	[125]	-0.47	0.54	1.01
individualized	PL	Ag/AgCl	[127]	-0.38	0.41	0.79

These measurements were performed in chloroform on ITO, which is most probably responsible for the significant difference (350meV) in the potential to 1.43eV previously

found for the bandgap of the (7,5) type [128].

Part of this significant difference must be due to the calculation with the Tanaka method, which overestimates potentials with different steepness in the intensity signal decay. Another factor is the variation of the dielectric surrounding by using another solvent.

It is noteworthy that the bandgap of the (7,5) type from the ACCVD raw material is 140meV smaller than what was found for the CoMoCat sample and has a much steeper signal decay at the reduction and oxidation sites which is why the ACCVD sample was chosen as a reference. The exponential phase factor nF/RT of the Nernst equation is responsible for the steepness. Therefore, it is possible to explain the steeper decrease in the ACCVD material with a higher electron diffusion due to the increased sample quality. Better Sample quality also reduces the number of defective states that would otherwise broaden the density of states for the excitonic transition. A lower amount of defective states, therefore, also explains the narrower bandgap in the CVD raw material. Nevertheless, this high discrepancy for the undoped (7,5) is unexpected and hinders giving a good interpretation of other results from this measurement.

The measurements at higher acetonitrile additons show an incomplete reduction, which is visible from the missing trion band at negative potentials. It is possible that in NCNT no charged excitons are generated as negative charges can bind to the graphitic nitrogen sites. However, due to the low spectral quality at negative potentials, these findings should not be considered strict.

The interesting finding from this experiment is that upon doping with nitrogen, the bandgap decreases by about 90meV. This decrease is attributed to the introduction of graphitic nitrogen forming charge acceptors in the bandgap.

2.6.4 Lattice Defects

The introduction of graphitic nitrogen to the sp2 hybridized carbon lattice is likely to form defect states. The method of choice for investigating defects in carbon nanotubes is Raman spectroscopy.

A small insignificant red-shift of the graphenic High Energy Mode (HEM, G-mode) for excitation with 488nm and 1064nm is visible. Increasing the nitrogen content of the feedstock also leads to a decrease in the intensity of HEM, which is nearly proportional to the decrease in optical density of the involved nanotubes. The D/G ratio was found to increase when exciting with 570nm, which is in agreement with literature.[118][129][130] However, this increase was barely visible in our samples and only at high acetonitrile concentrations where barely any carbon nanotubes are synthesized.

The D* mode shifts around 15cm^{-1} to the red. This shift is significant but lower than
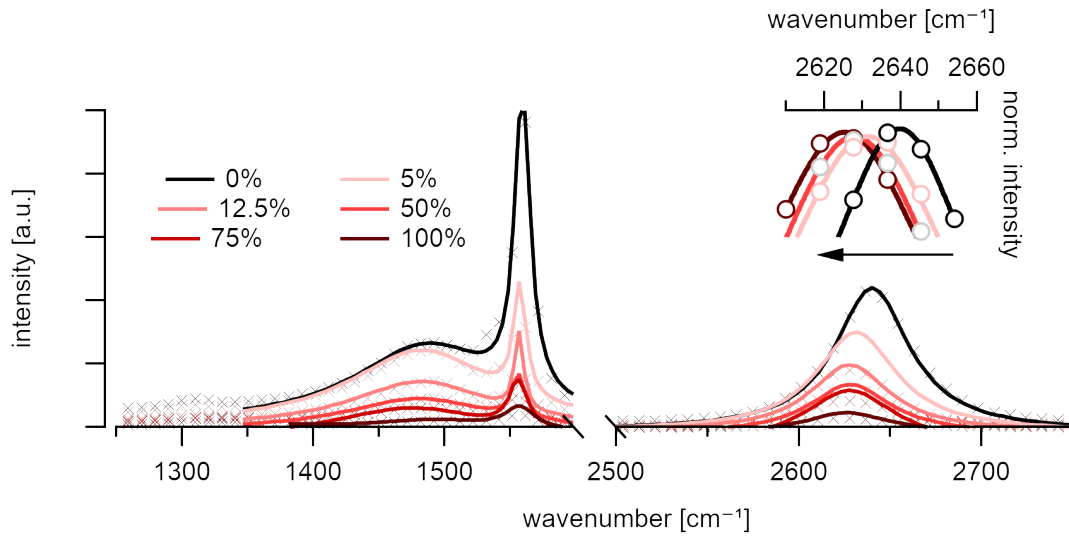
Fig. 26: Broadening and frequency shift of the Raman 2D mode ($\sim$2640cm^{-1}) of in NCNT in the unpurified samples. No energy changes in the graphenic high energy (HEM) mode ($\sim$1560cm^{-1}). Excitation at 488nm.

what is discussed in the literature [5] for this laser wavelength.

Thurakitseree et al. [5] discussed the change in chirality distribution as the origin for these shifts since the mode frequencies of Raman vibrations in carbon nanotubes are known to shift proportional to their inverse diameter[131]. A separation via density gradient ultracentrifugation (DGU) confirmed that there are no differences in the Raman spectra of purified (6,5) NCNT when compared to the ACCVD nanotubes.
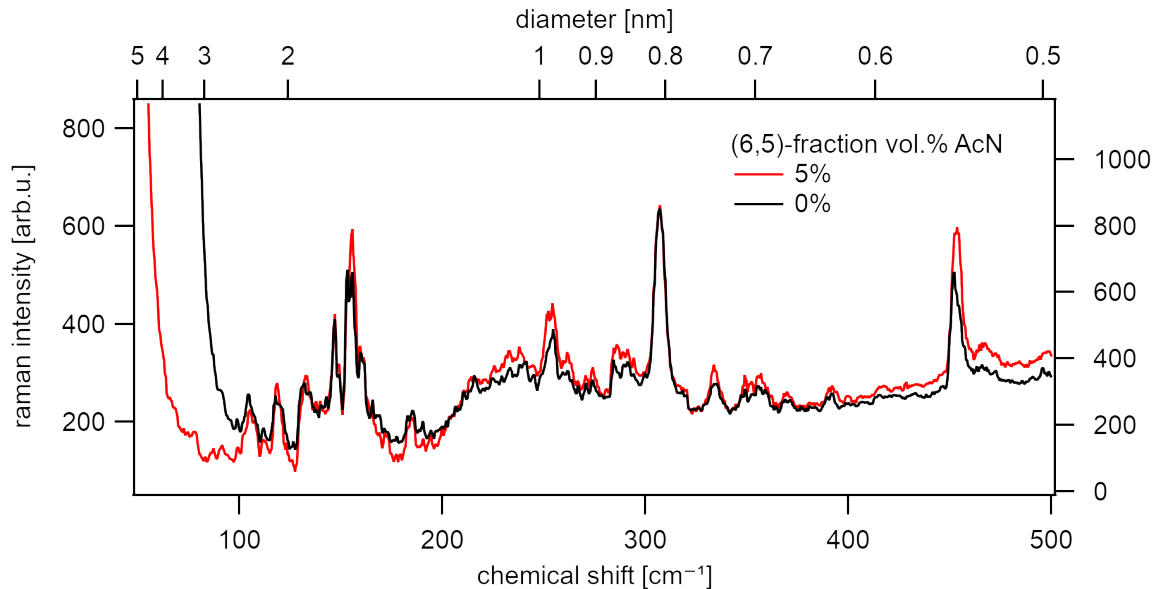
Fig. 27: No changes to the RBM mode and fingerprint region of the Raman active vibrations upon low (5vol.%) acetonitrile addition to the ethanol carbon source. Resonant excitation of the (6,5) type ($\varnothing$=0.76nm) at 570nm.

However, the photoluminescence quantum yield should be influenced as predicted by

the model of diffusion-limited contact quenching [132]. The samples were separated by chirality using a linear density gradient ultracentrifugation [102][103] to identify these changes.

A continuous shift of 6nm to the blue is visible along the density gradient for NCNT samples between the top and bottom fractions. This shift is overly dominant for the NCNT samples. A shift of 4nm with similar changes to the FWHM is typically allocated to the right and left-handed chiral species of the same (n,m) index.[133]
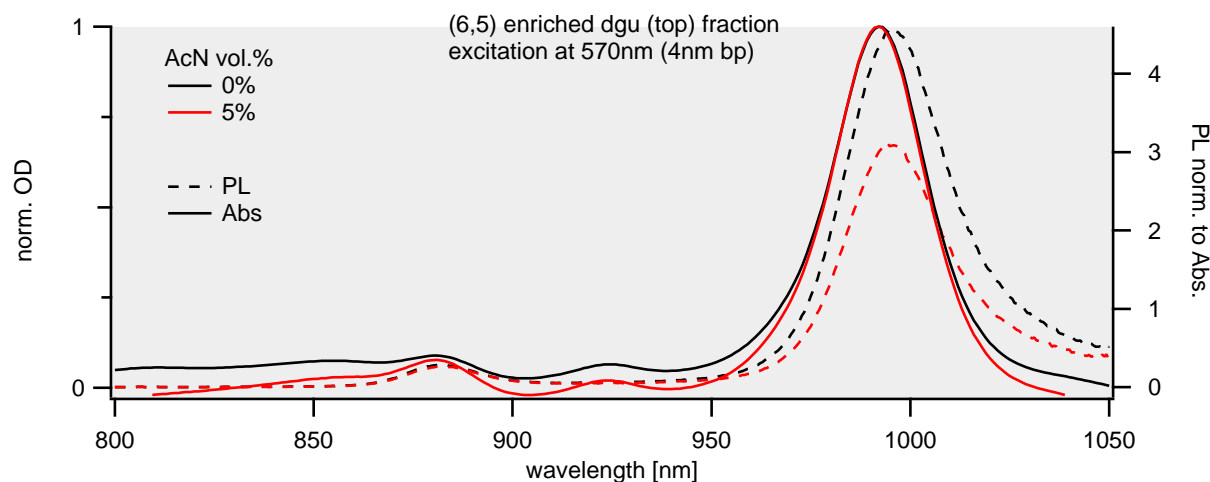
Fig. 28: Purified samples of the (6,5) type do not show a significant difference in their excitonic energy but also show a decrease in quantum efficiency

In the NCNT samples, the quantum efficiency of the measured nanotubes is reduced by 25-50% when compared to equally prepared ACCVD samples. These remarkable changes in quantum efficiency can be attributed to the nitrogen doping, which introduces exciton trap states. Notably, the carbon lattice seems to be intact for this type of NCNT judging from the results of Raman spectroscopy on the purified samples.

2.6.5 Molecular Nitrogen

As stated by Ayala et al.[117], it has been proven that molecular nitrogen is either intercalated [115][134] between the bamboo-like multi-wall structure or directly encapsulated [135][114] to the inside of NCNT. It is, however, doubtful if molecular nitrogen inside a single-wall carbon nanotube is preserved during sonication because it was found that nanotubes that are open at the tips do not contain nitrogen.[114]

As some nanotubes grow with closed caps on both ends, it should be possible to preserve the encapsulated Nitrogen if they are investigated as suspended carbon nanotubes. The encapsulated Nitrogen should be responsible for a change of the internal dielectric environment if the encapsulation would be to the inner nanotubes. An analysis of a set of more than 300 Nanotubes synthesized with the ethanol and ethanol/acetonitrile route

could not reveal significant statistical deviations from the natural spread of the excitonic energy in air-suspended carbon nanotubes. This result suggests that nitrogen adsorbs to the outside of the carbon nanotube surface during synthesis, and upon forming the bamboo-like structure, it gets encapsulated between the inner walls of the multi-wall carbon nanotubes. Single-wall carbon nanotubes, on the other hand, are not influenced by this process.

2.6.6 Conclusion

Nitrogen is responsible for a significant diameter reduction of the chiral distribution even at low additions of 5vol.% acetonitrile to the ethanol carbon source. The diameter reduction comes at the cost of a loss in photoluminescence quantum yield. Measurements in purified nanotube samples of the low-doped material could not determine changes to the graphenic lattice vibrations. Despite the many reports on molecular nitrogen adsorbed to the inner surface of NCNT, no significant changes of the excitonic energy could be observed, which leaves doubts regarding the adsorption of molecular nitrogen in single-wall carbon nanotubes. Electrochemical measurements have only shown n-type doping by graphitic nitrogen at highest concentrations of acetonitrile. The acetonitrile, when applied in low concentrations, is therefore thought to only poison the catalyst which shifts the diameter distribution to nanotubes with smaller diameters during synthesis. These nanotubes along with others synthesized from ethanol were statistically investigated and compared in more detail as suspended carbon nanotubes. Nanotubes with smaller diameters show a higher influences to changes in their dielectric environment than nanotubes with larger diameters. These nanotubes can also be investigated in higher digital detail with a silicon camera. The advantage of having a vast amount of spectra available in this range gives better insight into the adsorption processes on their surface that is not so heavily investigated for suspended nanotubes and complement some of the previous investigations in this topic.

2.7 Microscopic Insight

2.7.1 Resolution Limit

The wavelength of the observed light limits the resolution in optical microscopy. Photoluminescence microscopy, therefore, has lower spatial resolution than electron microscopy, where the wavelength can easily be lowered by increasing the electron energy. Carbon Nanotubes typically emit light from the excitonic state at their first subband transition with a wavelength of around 1μm. Such SWIR emission limits the spacial resolution to
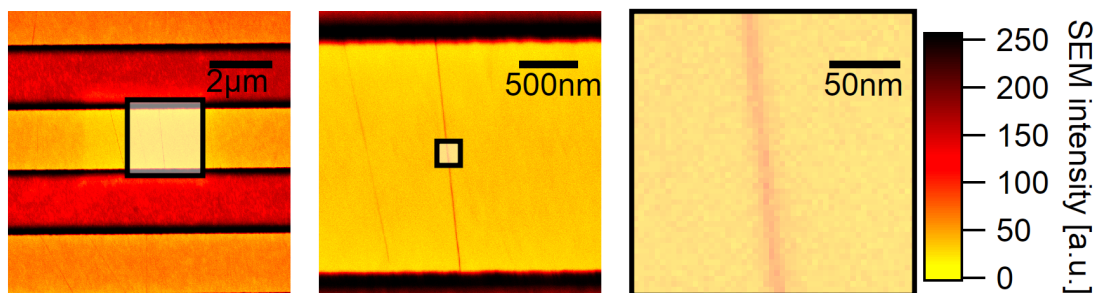
Fig. 29: A carbon nanotube of 1nm diameter that is hanging over a trench structure of 2μm and is referred to as "freely suspended" in air.

about 500nm. However, the diameter of a nanotube is 1nm and around two orders of magnitude smaller. Photoluminescence microscopy may, therefore, not seem to be the first choice for analyzing nanoscaled systems.

In the following chapter, I want to introduce the setup and recording technique for the microscopic setup that was devised to carry out all analyses in the following chapters. I also want to emphasize the insights that are possible from optical microscopy. This allows analyzing fundamental properties of the underlying excitonic particles like their diffusion length and their size by analyzing the phase information of images with high digital resolution (16bit).

2.7.2 Setup

Epifluorescence microscopy was performed on a Nikon Eclipse Ti series with an Olympus LCPLN50XIR 50x near-infrared objective lens (NA 0.65). The objective allows high working distances of up to 5mm and has superior transmittance of around 70 to 90% in the measurement window between 830nm and 1300nm. The magnification in Nikon geometry is 83.3x with the built-in 1.5x magnification enhancement of the Nikon microscope. The distance limits the resolution for taking images with this objective to the first minimum of the airy pattern: $r(airy) = 1.22\lambda/(2NA)$ This gives a maximally resolvable distance between two point sources of around 0.75μm at emission wavelengths above 800nm.

The sample is mounted using a custom-built sample holder and placed into a quartz cuvette with a 1mm thick observation window. This allows flooding the measurement chamber with solvents. The cuvette sits on a Thorlabs PR01/M rotational stage and can be fine-positioned using a Physikalssche Instrumente (PI) P-563.3CD nano stage with 300μm positioning range in x, y, and z-direction using a PI E-712.3CD modular digital multi-channel piezo controller.
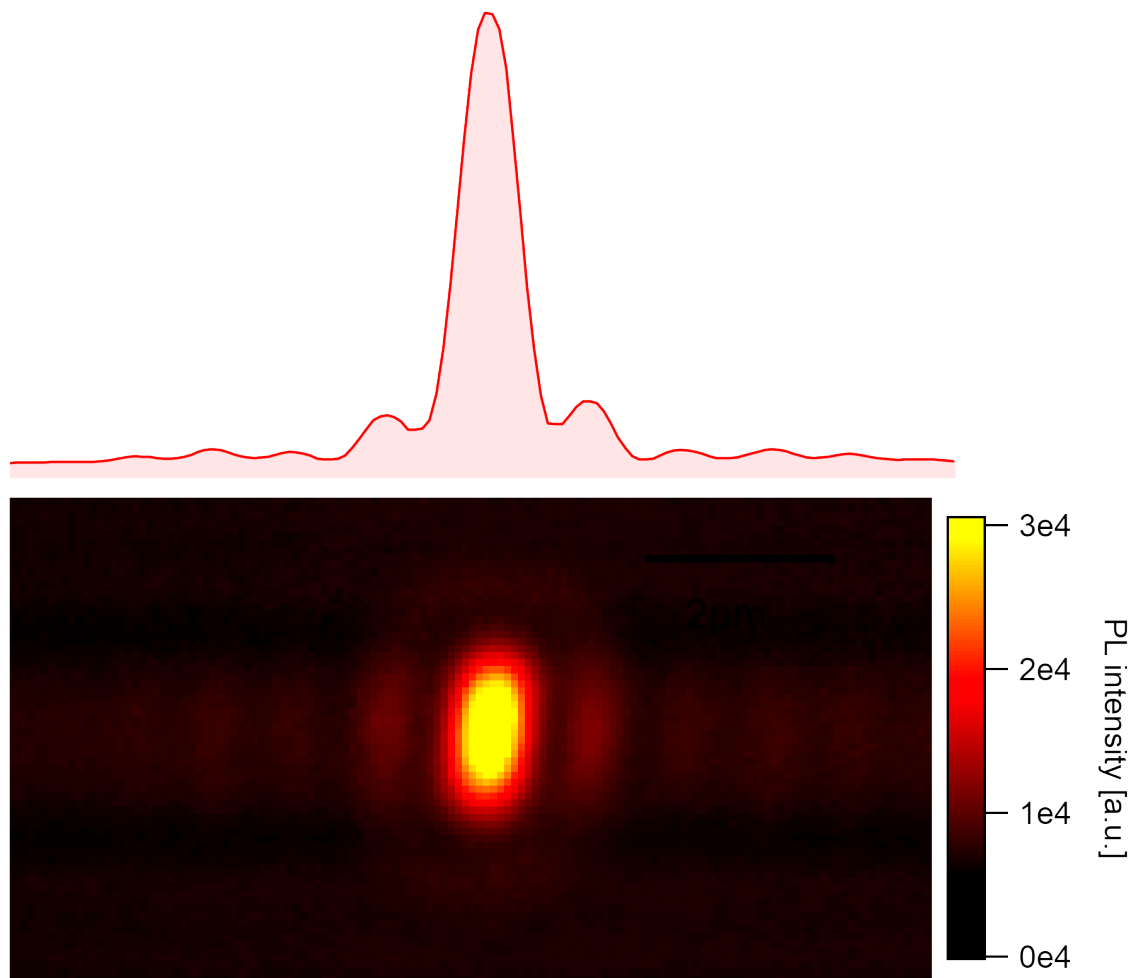
Fig. 30: A typical SWNT hanging over a 2μm trench structure taken with high digital resolution. The luminescence is spacially broadened due to emission in the SWIR and shows phase information.
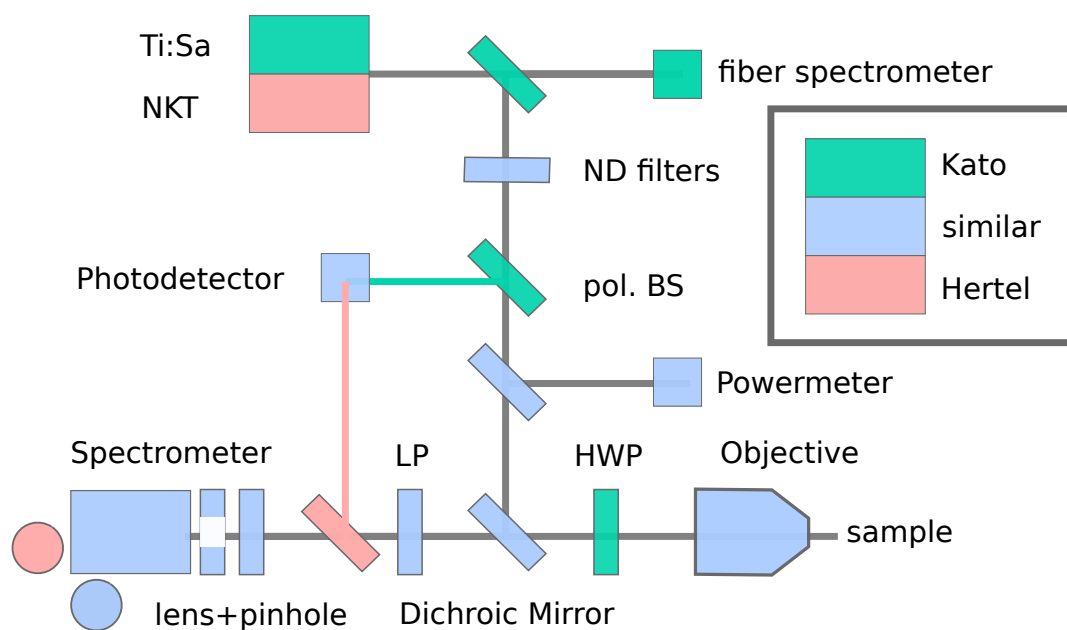
Fig. 31: Devised principal setup with emphasized similarities to the setup of the Kato group [136].
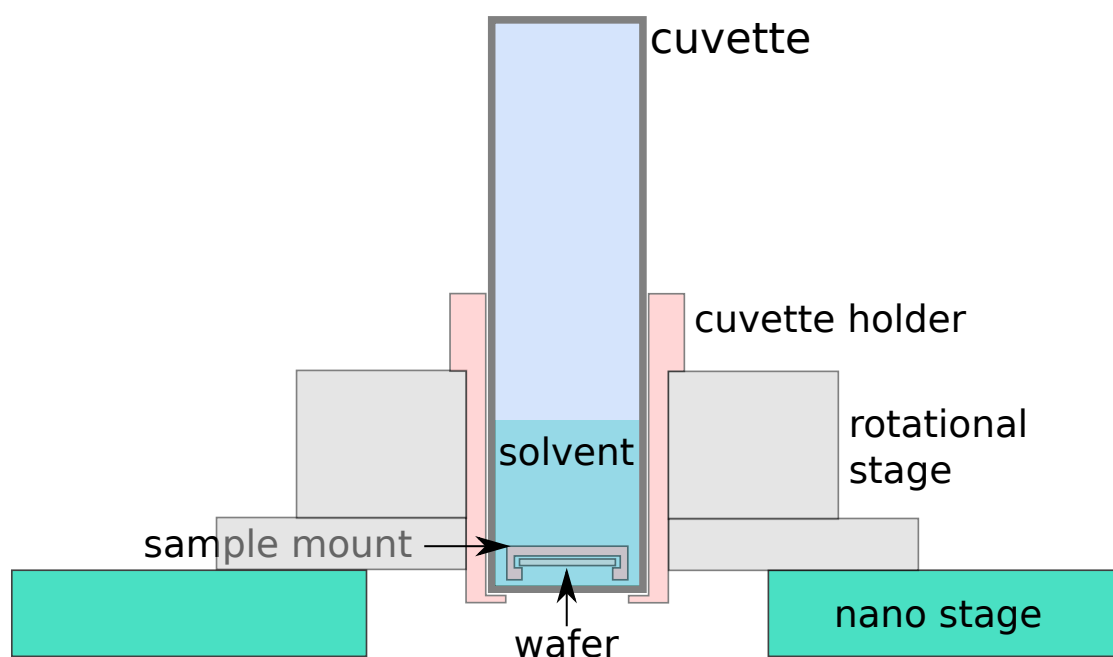
Fig. 32: The sample is placed into a glass cuvette that sits on a rotational and a nano stage.

Cameras

Images in the near-infrared region (800-1000nm) were taken with an Andor Clara camera model DR-01374 with an integrated Sony ICX285 progressive scan silicon CCD image sensor with a square pixel size of 6.45μm and a 4:3 aspect of readable 1392x1040 pixels (1.5MP) which is an effective diagonal of 11mm on the chip. Thermoelectric cooling was set to hold -55°C, and the readout rate for images was 1Mhz, where the lowest readout noise can be achieved, and digitization of 14bit (without dynamic range) is possible. Images were saved both as 16bit unsigned integers using Wavemetrics Igor Pro binary wave and plain ASCII format. Quantum efficiency for the images in extended NIR mode is expected to linearly drop from around 30% at 830nm to 5% at 1000nm.
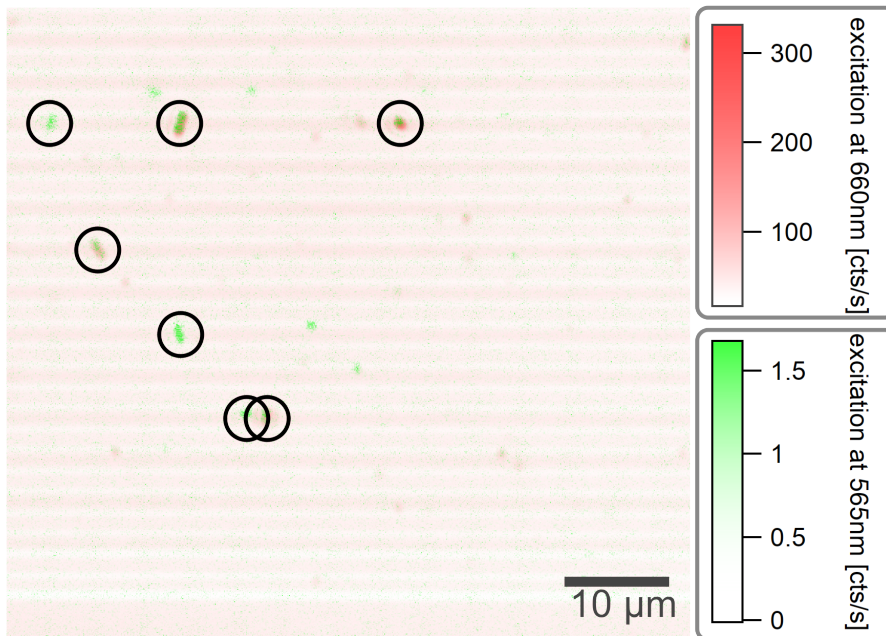
Fig. 33: Andor Clara (Silicon) detector at different excitation wavelength marked with lime green (570nm) and deep red (660nm) color.
Even though the two excitations differ by a factor of 100 in power, the highest intensities differ by almost a factor of 200, which could be due to the low sample size of the nanotubes, excited by green light.

A Xenics Xeva-1.7-320 series with 320x256 InGaAs pixels (80kP) and a quadratic pixel pitch of 30μm was attached for image measurements in the short wave infrared (SWIR) region (0.95-1.25μm). The sensor's effective array size is 12.3mm in diagonal, and illumination intensity is therefore nearly comparable between silicon and InGaAs camera. The camera is specified with a peak quantum efficiency of 80% and exhibits a near-linear photoresponse increase of 0.6 to 0.8A/W in the SWIR range with stable thermoelectric cooling at -70°C. It was specifically aligned for operation at 15s exposure times with high

gain to achieve low readout noise. An unilluminated background image had always been taken and was subtracted to account for the high dark current.

The dark current of the InGaAs camera is $0.19 \cdot 10^6 \mathrm{e^-/s}$ (specified at 280°C) which is around nine orders of magnitude higher than the $0.3 \cdot 10^{-3} \mathrm{e^-/s}$ of the silicon camera which dramatically influences the achievable image quality even though the quantum efficiency of InGaAs at 950nm is one order of magnitude higher than that of silicon. Notable is also that the dwell time significantly differs between the two cameras, and the InGaAs camera could not be operated at high exposure times (5min), which is needed for increased contrast in single-molecule spectroscopy.
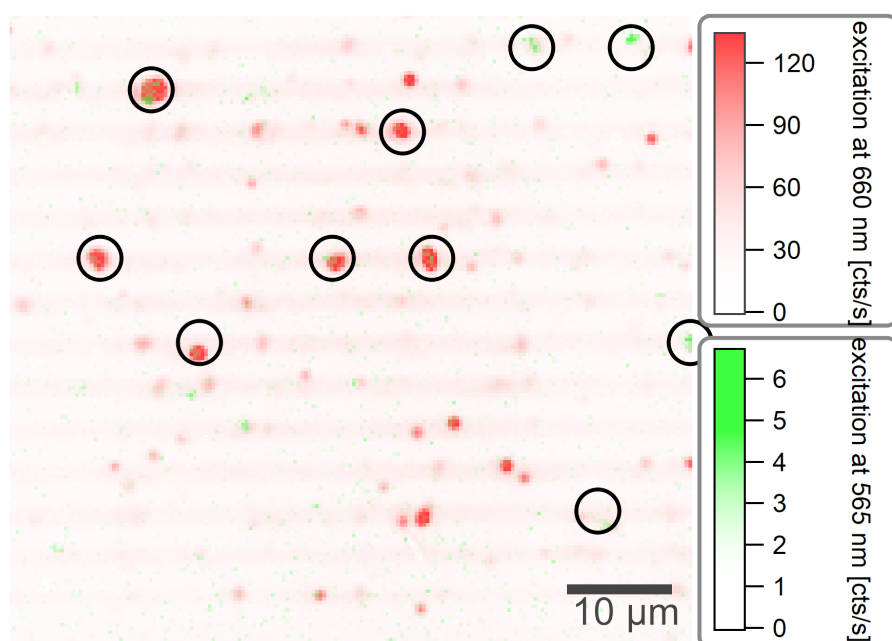
Fig. 34: Xenics Xeva (InGaAs) detector at different excitation wavelength marked with lime green (570nm) and deep red (660nm) color.
There is no significant benefit of the lime green excitation in the SWIR range as it only targets the (6,5) nanotubes.

Illumination

Images were illuminated using a Nikon TI-FL epi-fluorescence illuminator. The image area was illuminated with the iris of the TI-FL fully open. Images were taken using a 660nm dichroic mirror mounted to a Nikon microscopy cube assembly in the rotatable cube revolver of the eclipse. Two light sources were typically used: Thorlabs M660L4 for deep red illumination at 660nm and M565L3 with a 570nm bandpass for lime green. The sample was illuminated with a total power of 1.34mW for the red LED, and 350μW

for the green LED (15μW with attached bandpass). The excitation intensity is nearly homogeneously (FWHM > 1mm) distributed over the illuminated camera area (0.1mm^2). This low power excitation prevents the samples from being damaged by reaction with oxygen but also requires long illumination times.
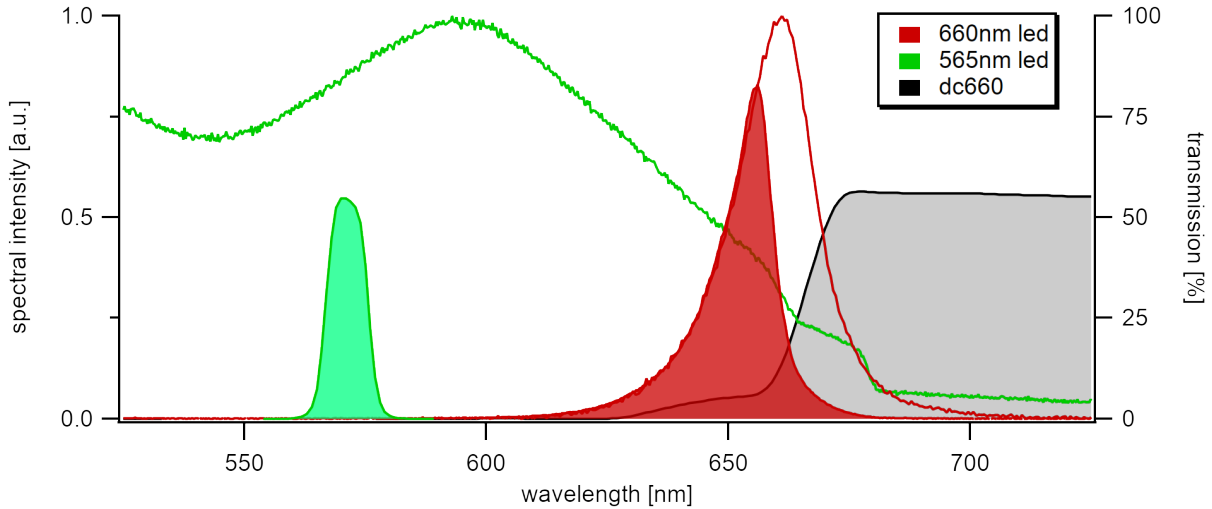
Fig. 35: The figure shows the excitation spectrum of the deep red and lime green diodes. The red spectrum (660nm) is cut off at the edge of the dichroic mirror (dc660), and the green spectrum (565nm) is narrowed by a 570nm bandpass filter.

Data Acquisition

The measurements were performed using a custom build LabVIEW program and saved using Igor Pro binary waves (ibw). The measurement program allows automatic positioning with the nano stage and subsequent spectra recording for a set of coordinates. It also allows recording photoluminescence excitation maps and images in the same automatic manner. Data were further processed using Wavemetrics Igor Pro 8. Files were loaded using the PLEM loader and analyzed using typical automated tasks with the mass analysis package.

The sample tilt plane was measured using the 3-point technique described at Ishii et al.[136]. The maximum intensity of the laser reflection in the z-direction at 3 points on the sample surface was measured using the silicon camera and analyzed with SMAcameraGetTiltPlaneParameters() which generates the Hesse Normal form of the surface plane. From this, the exact z-position could be calculated. Best images are acquired when the laser focus is 2.5μm away from the sample surface with a rough tolerance of 1μm. Best spectra were measured when the laser was focussed on the surface.

The described technique allows detailed scanning of the image area that is only limited by the range of the nano stage. The acquired images also show that substantial background emission comes from the bottom of the trenches. This emission was found to disturb
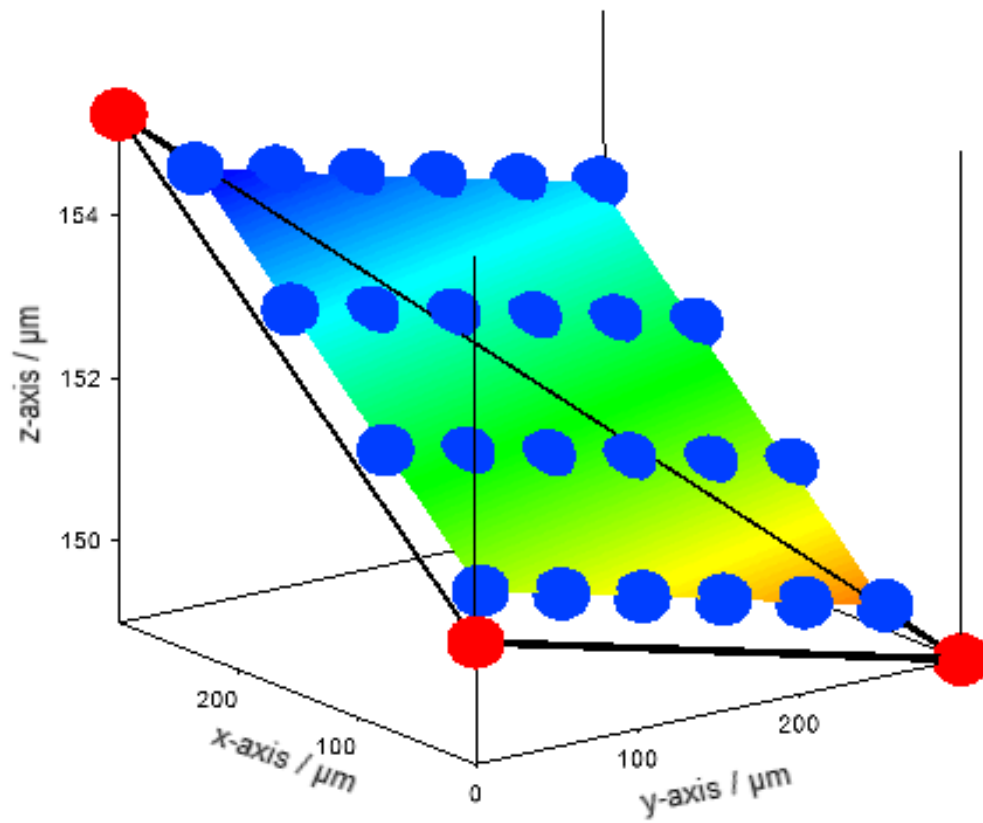
Fig. 36: Calculation of the tilt plane for image acquisition and spectra recording. The three points from SMAgetFocuspoints() are marked in red, and the locations for image acquisition of the $300x300\mu m$ range of the nano stage calculated from SMAcameraCoordinates() are marked in blue.

the recording of excitonic spectra as it increases in the SWIR. It could be reduced by accurately positioning the laser in the z-direction using the laser focus reflection from the sample plane as an offset to the calculated tilt plane parameters.
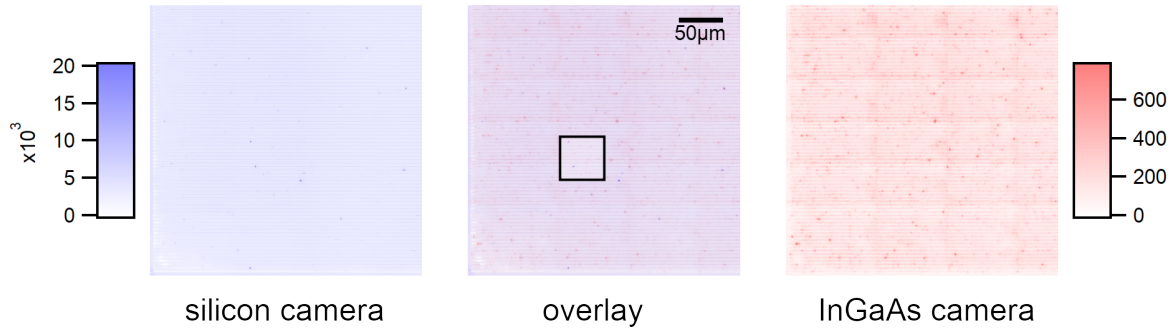
Fig. 37: An overview of the available sample area (300μmx300μm) is constructed from 24 individual images at different focus positions recorded with the LED excitation centered at 660nm.
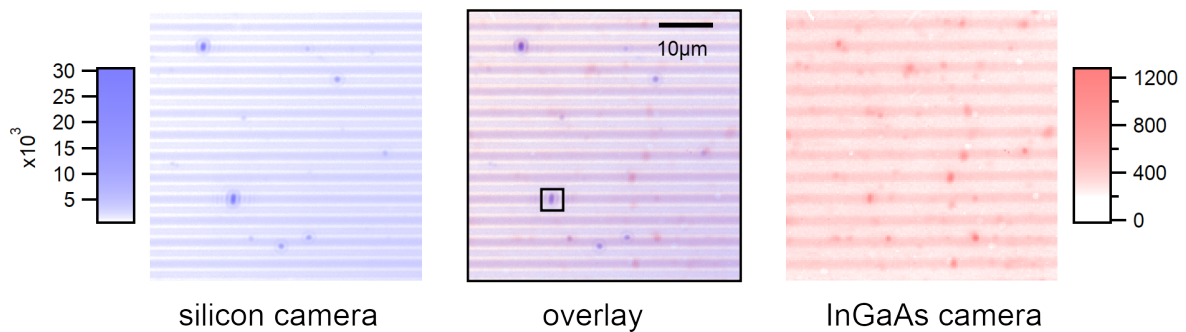
Fig. 38: A comparison of the two cameras at different zoom levels shows that both cameras detect a subset of the available suspended nanotubes while some tubes (mostly (7,5)) are detectable by both cameras.

In all measurements except tilt plane measurements, an 830nm long-pass filter is attached to filter out the excitation spectrum.

Data Analysis

The acquired images show homogeneous photoluminescence along the nanotube axis and symmetrical rays around the nanotube. Homogeneous emission along the nanotube axis is typical for long nanotubes and is sometimes considered to originate from a highly fractured defect landscape that confines the emission to distinct unresolvable spots. [137] However, it is also reasonable that such homogeneous emission can also originate from perfect nanotubes leading to high diffusion lengths. Typical for the acquired images are the rays surrounding the central nanotube location, which are more prominent in the trench cavity parallel to the longitudinal extension of the suspended nanotubes. The

images in this study exhibit an overly high digitization resolution compared to usually seen nanotube images [138][139], resulting in extremely high contrast. Images of lower digitization were recorded with the InGaAs camera but generally only show a blurred gaussian decay of the photoluminescence intensity perpendicular to the axis. The wide pixel pitch (and size) combined with the moderate numerical aperture of the objective lens used in this study does not allow to discover the presence of these bands with a typical InGaAs camera. The excellent full well depth of the Silicon camera at long illumination times allows studying these bands with exceptional digital resolution. In the following images, the false coloring is done on logarithmic scales to account for the exponential decay of the intensity in these bands. In the following, the origin of these rays is discussed to shed light on their origin. A simple optical simulation is included to substantiate estimations about the nanoscaled system that is responsible for these bands.
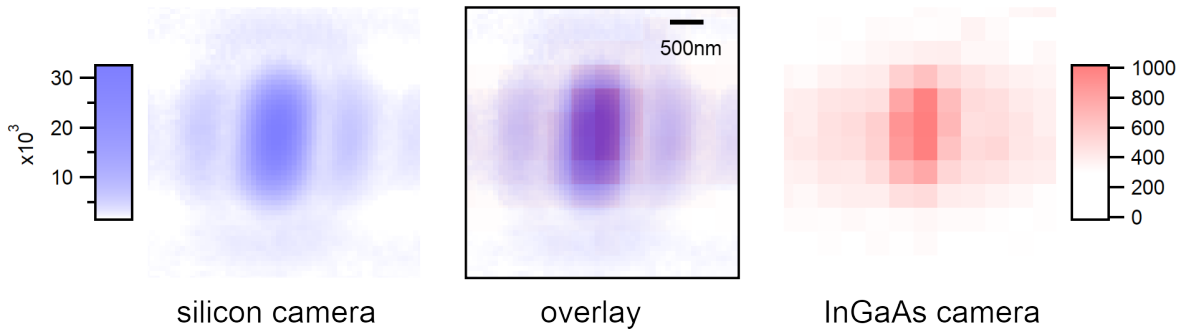
Fig. 39: Two images taken from the same location with different cameras show the effective digitization difference between the two cameras. Left: Andor Clara (5min exposure), Right: Xencis Xeva (15s exposure)

The images are recorded with a 660nm led and an attached beam splitter at 660nm. The observed bands may originate from the superposition of Rayleigh scattered energies with the incident energy creating a standing wave. However, due to the attached dichroic mirror, direct Rayleigh scattering of the second subband transitions is not observable and is thus not considered here.

Due to its shape, the pattern must have its origin from the interferences of excitons emitted along the longitudinal axis. Reflections from the $3\mu m$ deep trenches are neglected as the emitted field $E(\vartheta)$ is expected to be homogeneous around the circumference. Such a homogeneous emission would lead to a decay of the radial intensity $E(r)$ proportional to the (co-)tangent: $E(r(\vartheta)) = 2 \cdot 3\mu m \cdot \tan(\varphi)$ with φ between 0 and $\pi/2$ for r→∞. However, the decay of the emission is rather exponential, extending far beyond a distance of $2\mu m$.

Interferences caused by a reflection at the bottom of the trenches is also neglected since the led is considered a single photon emitter which allows assuming that only one exciton at a given time is emitted and excitons with different lifetimes that are emitted at different times are not probable to result in a large interference.

2.7.3 Simulation

To shed light on the origin of these side bands, a simulation of the images acquired with optical microscopy using Bessel's functions for single exciton emissions is carried out. A Monte Carlo simulation is done to estimate the emission profile of excitons along the axis.

First Passage

For Exciton diffusion, the principle of fist passage is applied [140][141][136]. The rather complex mathematical approach is easily transferred to the following simulation:

Excitons are allowed to diffuse freely along the tube axis. As soon as they hit a quenching site, they are blocked from further diffusion and decay non-radiatively. Quenching sites in this simulation are the ends of the nanotube that touch the silicon wafer surface. The nanotubes are considered defect-free without adsorbed molecules.

Excitons are generated using a homogeneous probability along the axis originating from the illumination with a spatially homogeneous light source. In this example, the (6,5) type is taken for the simulation, which emits from its first excitonic subband at a wavelength λ of 930nm.

The emission aperture is approximated with the longitudinal exciton diameter a and the observer distance d is set equal to the working distance of the objective (5mm), neglecting a 1mm thick quartz glass window between observer and nanotube at a distance of 1mm from the silicon wafer surface. The point spread function PSF(r,θ) for the emission is approximated with an airy disc of diameter a in cylindric coordinates using Bessel's function of first-order J_1 from the SLATEC Common Mathematical Library as a solution to diffraction-limited beams:

$$PSF(r,\theta) = 2\frac{J_1(x)}{x} x(r,\theta) = k \cdot a \cdot sin(\theta) = \frac{2\pi}{\lambda} \cdot a \cdot r/d$$

The LED is operated at low power densities and has considerable temporal coherence in the 10ms range to only excite one exciton at a time. This makes it reasonable to neglect electronic many-body effects like exciton-exciton annihilation and phase space filling for the simulation of these images.

Note: The assumption that only one exciton is generated at a time is based on the relative absorption cross-section of 1.710^{-17}cm^2 per carbon atom [142][143]. This is used together with the central emission wavelength of 660nm at irradiation of 1.5W/cm^2 to estimate the generation of excitons in this system to 85 excitons per carbon atom and second. For the (6,5) type, which has 88 carbon atoms per nm [144], this gives 15 million
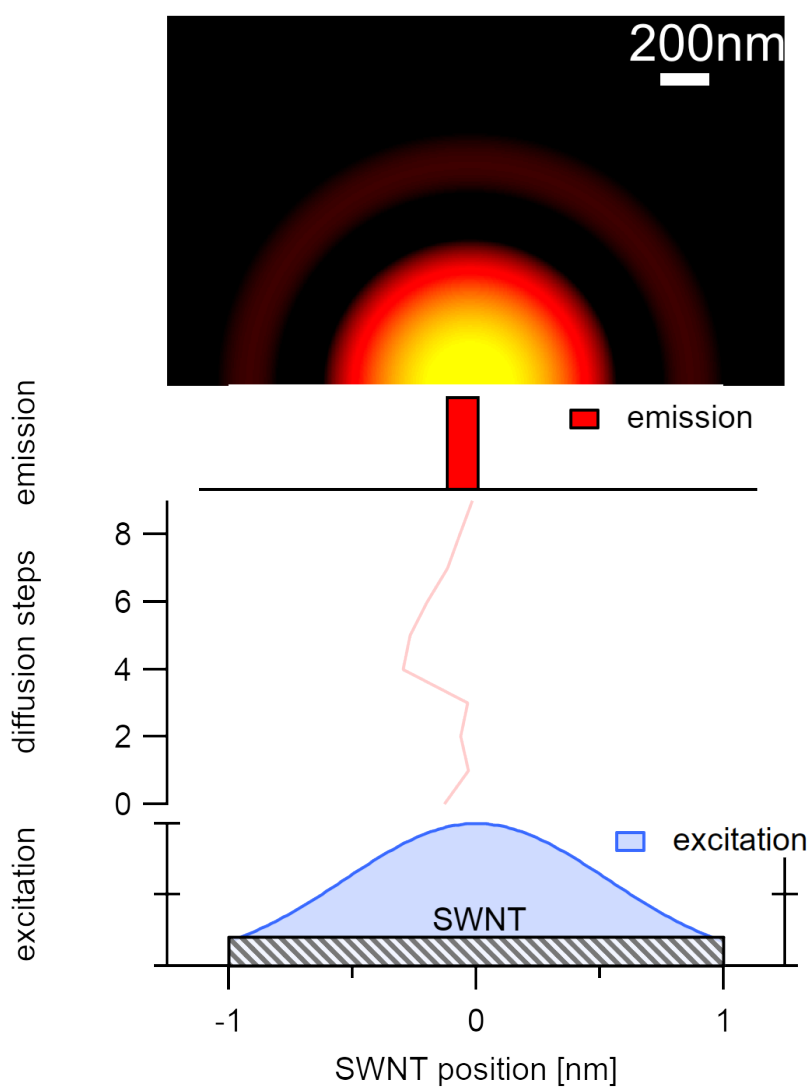
Fig. 40: An exciton is generated in the center of the nanotube by a gaussian shaped laser profile. The exciton diffuses over nine steps and decays radiatively, which gives the (axially symmetric) point spread function of single excitonic emission calculated for one lateral side.

excitons per second on a 2μm long carbon nanotube. As the generated excitons have an estimated decay time of less than 350ps, this allows assuming that only one exciton at a time is generated in the system.

In comparison to laser excitation, however, quenching at the ends of the nanotube tips or respectively at the contact to the silicon substrate can not be neglected. The irradiation with a laser was simulated and compared to homogeneous irradiation. While the images from laser irradiation show emission from the center of the nanotube similar to a point source, the emission from homogeneous excitation show wider spreading along the nanotube axis with a bone-like emission profile.

Exciton Diffusion
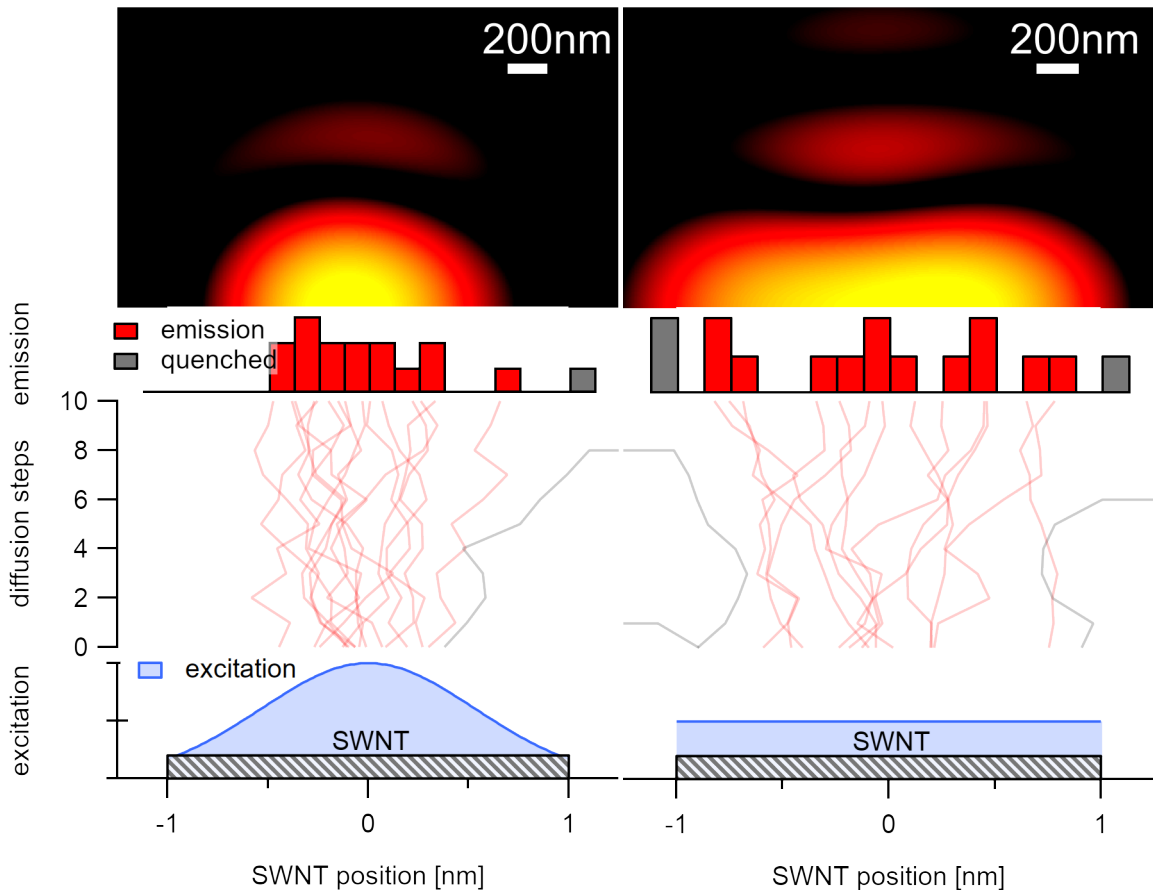
Fig. 41: The emission profiles of two 2μm long carbon nanotubes illuminated with a light source of spacially homogeneous intensity (left), and a gaussian shaped profile (right) show that end quenching effects and diffusion length are not neglectable in this system.

For a typical simulation, 2048 excitons are allowed to decay after 10k diffusion steps radiatively. They emit from spots on a 24nm spaced potential energy landscape [145].

The length of the nanotube is fixated in the simulation at 2μm neglecting elongations caused by nanotubes dispersed non-perpendicularly.

Due to end quenching effects, the spatial emission profile upon homogeneous emission is primarily governed by the exciton diffusion length. Within the simulation, the diffusion length was varied. For a typical image, 10k diffusion steps are calculated while the diffusion length l_D is distributed with a Gaussian probability to give the displacement s [136].

$$\frac{1}{\pi l_D} exp\left(-\frac{s^2}{l_D}\right)$$

Discrete diffusion steps are necessary for the model of first passage to eliminate excitons that hit a quenching site during their lifetime. Due to Fick's law, the quadratic diffusion length is proportional to the lifetime $l_D \propto \sqrt{\tau}$. This readily gives the diffusion length l_N for N diffusion steps at a fraction N of the lifetime τ:

$$l_N = l_D\sqrt{\frac{1}{N}}$$

The diffusion length is typically estimated to be 10nm for short-lived excitons [146] and 100nm [147][148] up to 1 micrometer [141] for the long-lived excitons that are relevant for photoluminescence. Within the simulation, the diffusion length is varied between 10 and 1000nm, which allows simulating the effects on the squared combination of all PSFs. In the simulated diffusion range, the emission intensity shape at the tips of the nanotubes varies. These end quenching effects allow estimating that the diffusion lengths in these samples are greater than 350nm but could also be up to 1μm. It has to be noted, however, that as the diffusion length approaches the nanotube length, a significant amount of excitons is affected by end quenching. At diffusion lengths of 1μm, this typically affects 75% of the excitons in a 2μm long nanotube. The amount is reduced at lower diffusion lengths. While at 350nm, 30% of the excitons decay non-radiative, at 100nm 8%, and at 10nm, only 0.5% are affected by end quenching.

Relying on the results of this simulation, we estimate end quenching effects as the dominating decay process in suspended nanotubes that are homogeneously excited at low fluence. This finding is especially important for nanotubes shorter than 2μm, where the nanotube length approaches twice the diffusion length. A reduction in diffusion length can, therefore, yield brighter photoluminescence even in air, which was already shown for quasi-zero dimensional systems with excitons immobilized at oxygen defects [149].
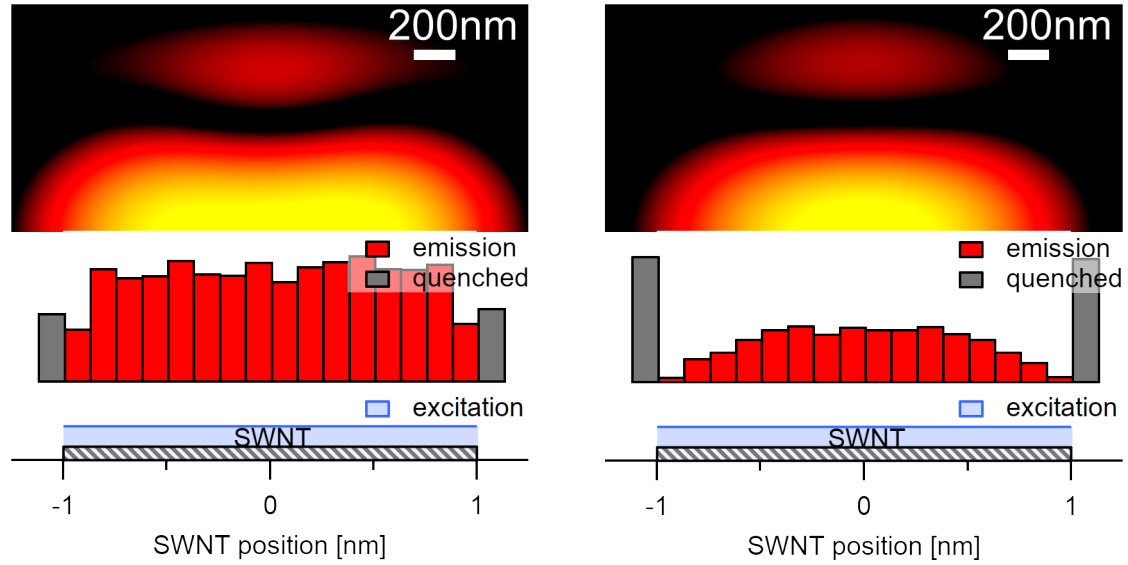
Fig. 42: The exciton diffusion length determines the shape of the excitonic emission. At low diffusion lengths (<100nm), end quenching becomes neglectable (left) while at diffusion length above 350nm, it is significantly high, and the shape loses its bone-like structure (right).

Exciton Size

The exciton size a can be approximated from the phase information of the transverse radial part of the observed airy discs. A commonly used size of 2nm was measured using SC-dispersed nanotubes [146]. Newer studies suggest that this size is by at least a factor of 6 higher for better-individualized nanotubes [150][144]. For a suspended (6,5) type, which was taken as a reference for the simulation, the exciton size is estimated to be 8.5(5)nm. This is by a factor of 3-4 larger than most estimations but also by a factor of 2 lower than the recent approximations for nanotubes with a strong dielectric screening [144]. In environments with low dielectric screening as in air-suspended nanotubes binding energies of around 725meV [151] are found, which is by a factor of 2 higher than in micelle encapsulated nanotubes [39]. An exciton can be approximated with a hydrogen atom where the radius is inverse proportional to the energy. Double the energy gives half the radius, which makes an exciton size of 8.5(5)nm reasonable compared to the size of 14(3)nm at half the binding energy.

A simple airy disc for the excitonic emission is only a rough approximation. The circular aperture is not a good approximation of an exciton considering the reasonably large exciton sizes. The aperture should rather be elliptically shaped, which would influence the above approximation for end quenchings. The fact that the airy disc is not perfect can also be seen from the comparison of the intensity in the first and third horizontal maximum of the measured and calculated images. For a more exact approach, a linear combination of higher-order Bessel functions has to be used, which leads to more complex
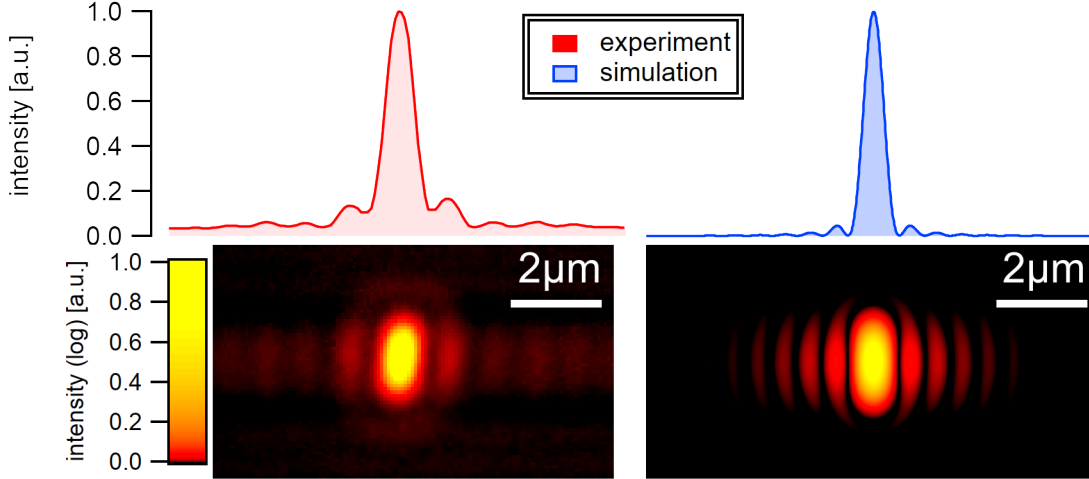
Fig. 43: The simulated airy disc pattern shows good agreement with the camera images at a simulated emission aperture of 6.5nm.

solutions to the Fraunhofer diffraction equation.

Far Field Propagation

The easiest of these solution is a monochromatic wave propagating in z direction with a phase factor that describes the pattern in the (x,y) plane. It is conveniently described in cylindric coordinates [152]:

$$E(r, \phi, z) = exp(ik_z z) \cdot J_n(k_r r) exp(-in\phi)$$

The radial and transverse wave vector along z satisfying $k = \sqrt{k_z^2 + k_r^2} = \frac{2\pi}{\lambda}$ and the radial coordinate in the (x,y) plane $r = x^2 + y^2$. Bessel's functions generate the periodic part of the airy pattern. The phase factor, though, is invariant to the distance from the source. Such waves extend with a slow exponential decay along the z-axis, and their radial intensity profile in the (x,y) plane is independent of the distance z. The first order beams carry phase information and are thus able to reconstruct in the far-field [153]. Non-diffracting Bessel waves have been found as special solutions to the Helmholtz equation [154] if the radius of the emission source is far smaller than the wavelength of the emitted light. This is the case for carbon nanotubes as they emit at wavelengths of around $1\mu m$ with exciton sizes smaller than 10nm and a potential energy landscape of 24nm.

Without making assumptions about the shape of the generating PSF, the observed wave function $\Psi(x)$ can be destructed into its spacial autocorrelations using Fourier Analysis or a Wigner quasi-probability distribution. The Wigner distribution W disassembles the wave function from real space into phase space, allows to visualize phase information,

and is thus able to emphasize the source of interferences in the camera images.
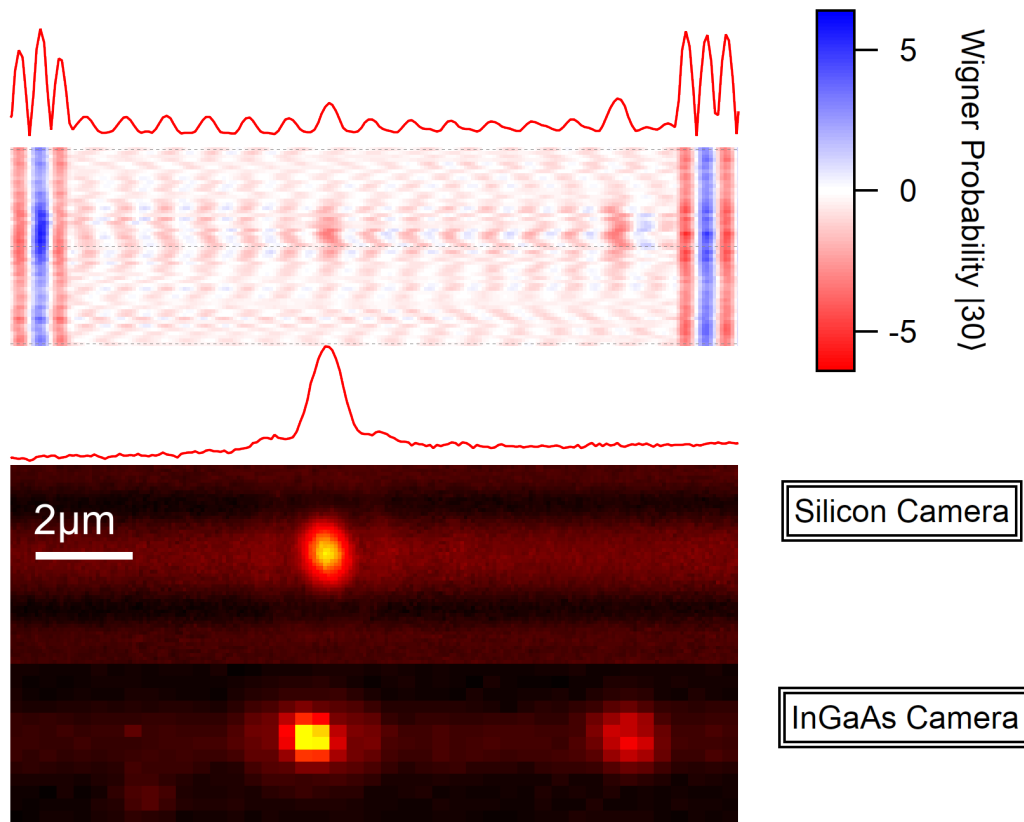
Fig. 44: An astonishing feature of non-diffracting Bessel waves is that they are able to reconstruct in the far-field. This allows detecting asymmetries in the electric far-field, making SWIR nanotubes visible for the silicon camera.

Such a reconstruction of the generating wave functions using Wigner Transformation is able to reveal far-field interference of nanotubes. The surprising outcome of this interference is that nanotubes that are usually only visible with the InGaAs camera can be detected if they are located in the surrounding (~6μm) of a Silicon-active nanotube. This far-field interaction confirms the presence of non-diffracting Bessel waves emitting diffraction-free. The datasets need more sophisticated analysis to study if this interference is wavelength-independent as the phase factor suggests and up to which distance it is able to reconstruct the phase.

2.7.4 Conclusion

Microscopy images of carbon nanotubes are recorded at the optical resolution limit. From the shape of these images, it is possible to estimate an exciton diffusion length higher than 350nm in 2μm long carbon nanotubes. Images recorded with high digital resolution reveal the phase of the emitting point sources. This phase holds information about the wavelength and size of the emitter. As the wavelength was also measured, it is possible to estimate the exciton size to 8.5(5)nm. Emitting sources where the emitter size is much smaller than the emission wavelength are able to reconstruct in the far-field. This allows detecting the source of excitonic emission interferences by analyzing the phase information making excitonic emission visible solely by their phase and independent of their emission energy.

2.8 The Perfect Nanotube

Adsorption experiments are one-time experiments that can not preserve the clean surface of the nanotubes during an experiment. It is also evident that only one nanotube per sample can be observed and studied. Therefore, it is crucial to select the best nanotube for the upcoming adsorption studies. Within the limit of the nano stage, this requires scanning all trenches in this range. Camera images can give great insight into the locations of these tubes. As described by Ishii et al.[136], a subsequent exact scan for the identification of the exact position as well as the identification of aggregates is needed. Such an exact scan reveals the positions of the brightest nanotubes that are then taken to further examinations. For this information, statistical methods are combined with a manual analysis. It is also possible to easily study principal phenomena like defect generation or spectral diffusion in this system which is necessary for adjusting the excitation power to the setup.

2.8.1 Setup

Monochromator

Spectra were taken confocally using an Andor Shamrock 303i-B-SIL monochromator with an integrated grating turret with two gratings of 300lines/mm blazed at 500nm and 1200nm and one grating for high range and lower resolution with 150lines/mm with the blaze wavelength at 1250nm. A typical slit width for the experiments is 200μm. NIR and VIS measurements were performed with an Andor Newton DU920P-OE detector. This detector has 1024x255 pixels with a quadratic pixel size of 26μm, which is an effective diagonal of 28.5mm. The vertical binning was reduced to 25 pixel to remove dark noise

and spikes at longer integration times. Spectra from microscopic measurements use an illuminated pixel size of only around 300μm on the detector. Therefore, the detector readout was constrained to a subset of 25 vertical pixels, which essentially covers the total emission area and leaves room for some alignment errors. Selecting a subset of 25 pixels also reduces the RMS noise and reduces cosmic ray spike generation. An Andor iDus model DU491A-1.7 covered the SWIR range with 1024x1 pixels and a pixel size of 25x500μm. The detection area and illumination are comparable to the binned silicon camera and completely cover the spacial extension of the microscopic emission. Both detectors are cooled thermo-electrically to -90°C with an additional attached water cooling for temperature stabilization.
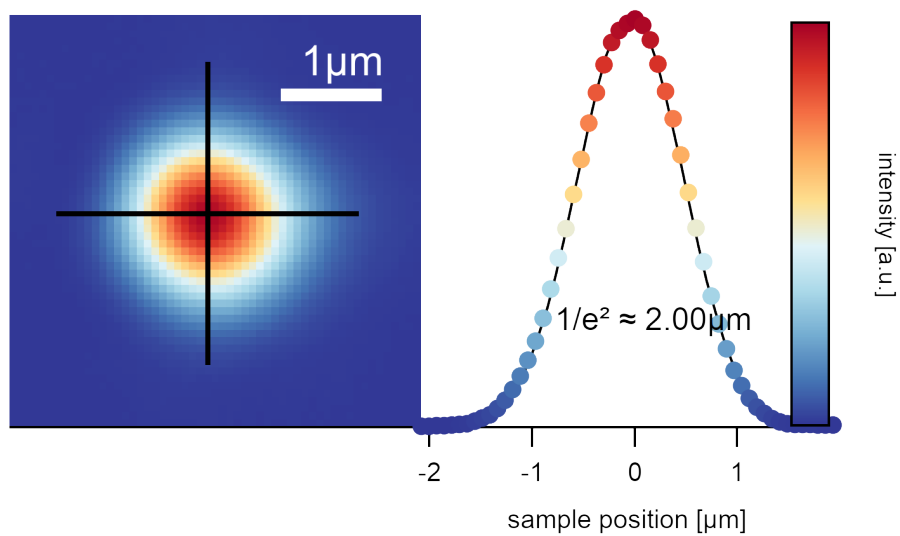
Fig. 45: The laser profile of the SuperK after the fiber output is around 1.2mm broad. If focused on the sample with the objective, it illuminates the area with a diameter of 2μm (the diameter of the laser spot is measured where the maximum intensity I_0 drops to I_0/e^2).

Excitation in epi geometry was accomplished using a chroma 760nm dichroic mirror and an 830nm color glass long pass filter. For the excitation of the sample area, a NKT SuperK Extreme light source is used, which generates a suitable white light spectrum. A NKT Varia was added for wavelength control of the excitation bandpass. The excitation light is filtered by two NIR neutral density absorption filters and a variable neutral density filter to adjust output power. Laser performance was continuously measured and recorded from the reflection at a thin glass plate using a Thorlabs PM100D power meter.

Excitation
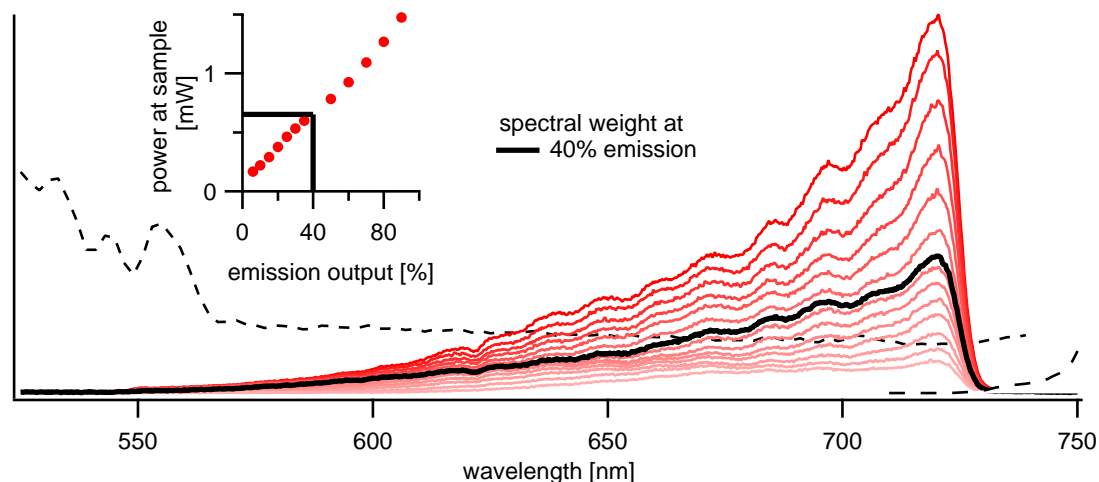
Fig. 46: The excitation spectrum of the light source varies with the selected bandpass and emission power. For a bandpass of 550-725nm, the excitation spectrum varies with the output power. Dashed lines indicate the limit of the excitation range due to absorption in the dichroic mirror.

The maximum output of the NKT SuperK in this setup is 18W. The spectrum varies strongly over the visible range and intensifies to the NIR due to the white light generation process using a NIR pump laser. Thus also the excitation power varies depending on the selected bandpass and the pump laser emission strength.[155] The NKT output was fixed to 40%, and the excitation power was then reduced with a variable neutral density filter to reduce the actual power on the sample. The emission control was fixed at 40% during photoluminescence excitation measurements. As the spectral weight varies over the excitation range, the power was continuously measured and used for excitation corrections.

Power

Excitonic emission from carbon nanotubes has shown to be sensitive to the excitation power. The irreversible generation of defects at high power due to the reaction with oxygen leads to the formation of defect sites, which act as exciton trap states leading to a decrease in photoluminescence intensity with an accompanied red-shift of the emission signal. A non-linear, reversible reduction of the intensity is observable above $25\mu W$ excitation power. This reduction of the intensity originates from electronic many-body interactions leading to exciton-exciton annihilation. An additional but more critical factor for the following experiments is the subsequent shift of the emission spectrum to higher energies at higher laser powers. The shift originates from changes in the dielectric environment that are caused by a laser-induced temperature increase of the adsorbed
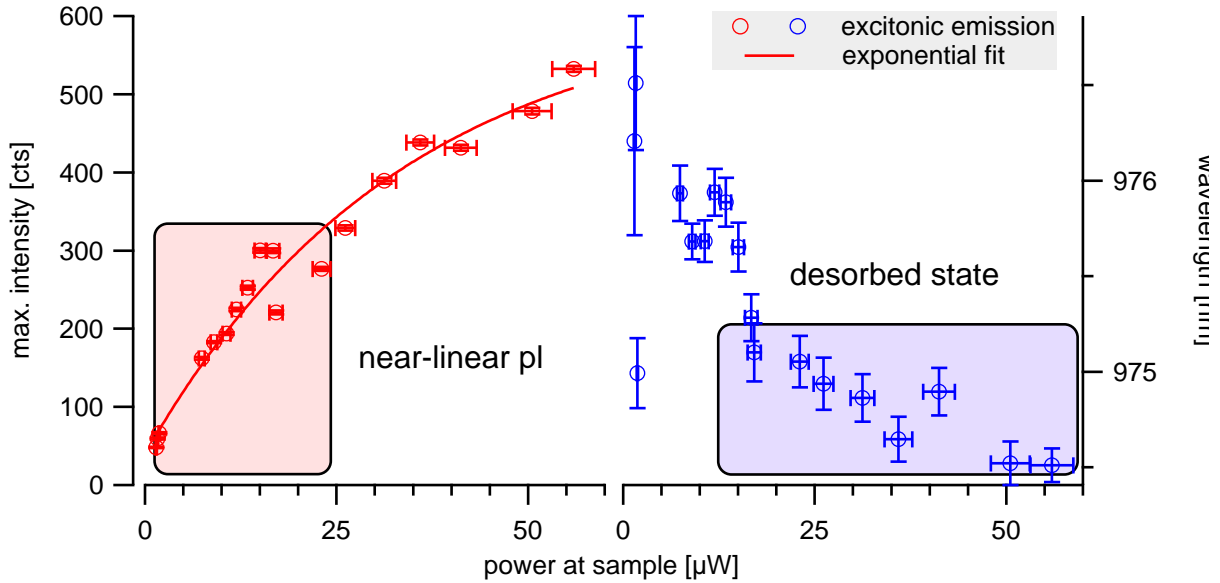
Fig. 47: Excitation of a suspended carbon nanotube has to happen below 50μW with a 20nm bandpass that fits the targetted chirality. Continuous shifting of the excitonic emission peak to the blue is a commonly observed phenomenon for measurements in air.

molecules. In our setup, a typical individual semiconducting carbon nanotube is excited with a 20nm broad spectrum of 662.5-682.5nm at the excitonic transition in its second electronic subband. In such a system, the nanotube shows energy-stable emission at around 20μW excitation power.

Note: The setup-specific excitation power at the sample is six times higher than the measured reflection at the glass plate. However, the spectra in this work are normalized to the photon flux measured at the glass plate as the ratio is proportional.

Polarization

The emission output after the NKT Varia is elliptically polarized. Carbon Nanotubes are excited to their E_{22} states only if the excitation aligns with the nanotube elongation axis. Although there are states like the E_{12} or coupled phononic states that can be excited perpendicular to the axis. The absorbance of these states is generally lower, which in turn also gives lower emission when relaxed to the E_{11} level. Thus, carbon nanotubes can theoretically be excited in every polarisation direction. However, to ensure that the maximally possible spectral overlap is happening, the emission for different polarisations was tested. In all measurements, the nanotube emission maximum coincides with the maximum of the NKT excitation. Most homogeneous polarisation measurements, though, were performed with an angle offset of around 25° to the elliptical laser excitation axis

which suggests that there is some degree of skew between the orientation of the nano stage and the polarisation of the light source that is most probably due to the alignment of the uplift mirrors. In short, polarisation is not expected to have a significant impact on this setup with a high tolerance of $\pm 30°$ to the nanotube axis.

Spectral Window

The as-described setup is limited when taking spectra above 1300nm due to the absorption of the dichroic mirror. It excels, on the other hand, at taking spectra between 830nm and 1000nm. It allows observation of carbon nanotubes with diameters from 0.7nm to 1.2nm, which is also the targeted diameter of the chemical vapor deposition synthesis. Even though at 800°C, most carbon nanotubes emit between 1100 and 1200nm, the nanotubes that emit between 800 and 1000nm show excellent emission properties, which are most probably due to their high photoluminescence quantum yield estimated to around 7% [156].
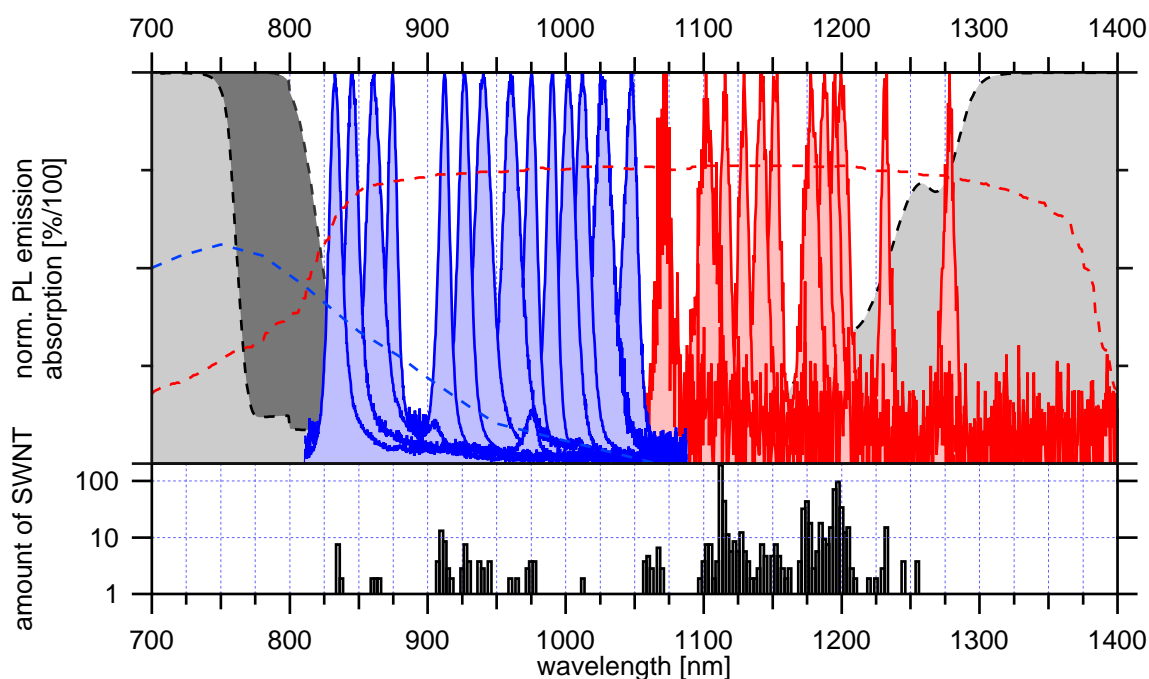
Fig. 48: The blue spectra were measured using a silicon detector, the red spectra using an InGaAs detector. The dotted line shows the quantum efficiency for the detectors. The measurement range is limited at low wavelength by an 830nm long-pass filter and at high wavelength by the absorption of the chroma 760nm dichroic mirror.

Also, gratings need to get considered when taking spectra. Gratings distort the spectrum nearly quadratically to the edges as each grating is optimized for a specific Blaze wavelength. These effects are reduced computationally with grating correction curves. Additionally, if the spectral intensity among gratings with different amounts of lines

per mm needs to get compared, the intensity can be corrected to the wavelength pitch [cts/nm] but stats.booWavelengthPitch as such a correction alters integration results. When acquiring wavelength-dependent spectral information, the spectra are furthermore corrected to the quantum efficiency curves of the detectors. The measured excitation power is then transferred into a photon flux [photons/s] by taking the central excitation wavelength of the selected bandpass as photon energy. The microscope setup has a reasonably unusual beam splitter for taking spectra (Chroma Technology T760LPXR). Due to its varying reflectivity between 500-570nm and setup constraints, it is necessary also to correct the measured excitation power in this range. All microscopy spectra are furthermore corrected using the transmission curves of the mounted high pass filters. For spectra, it is a 750nm (Thorlabs FELH0750) or an 830nm color glass filter. The filter curves are slightly corrected by the reflectivity of the used silver mirrors at 45° incidence. Missing data points within these curves are linearly interpolated. For image acquisition, only the color glass filter mentioned above was used, and only magnification and tilt corrections are performed computationally. Spectra with different excitation times were compared, by normalizing to their exposure time in seconds. All corrections are calculated using PLEMd2BuildMaps() which preserves the original measurement data and allows to reversible apply specific corrections. When displaying PLE maps as images, the pixels are displayed evenly spaced for convenience reasons, whereas calculation and analysis are always performed on the physically correct, distorted scale. A measurement series on one nanotube was usually performed without changing filters, grating, or detectors during the measurement.

When analyzing multiple camera images in one image, camera images were rotated to match the setup specific rotational offset between nano stage axes and camera pixel alignment. Magnification is corrected for Nikon geometry with an additional constant factor to achieve maximum image overlap for images taken at different positions of the nano stage. The relative positioning of the nano stage within 300μmx300μm is taken as a reference for the magnification correction.

2.8.2 Technique

Trench Scan

The silicon substrate consists of 2μm wide and 3μm deep trenches, evenly spaced in parallel arrangements every 4μm. The center of the laser excitation is positioned on a known offset to the first trench on the substrate. Such zeroing allows performing a scan over all trenches to identify the exact position of nanotubes. The trenches are scanned in 2μm steps along the trench as the laser spot size determines the step size. In such a scan, the rough locations of suspended nanotubes can be estimated. Using a broad excitation
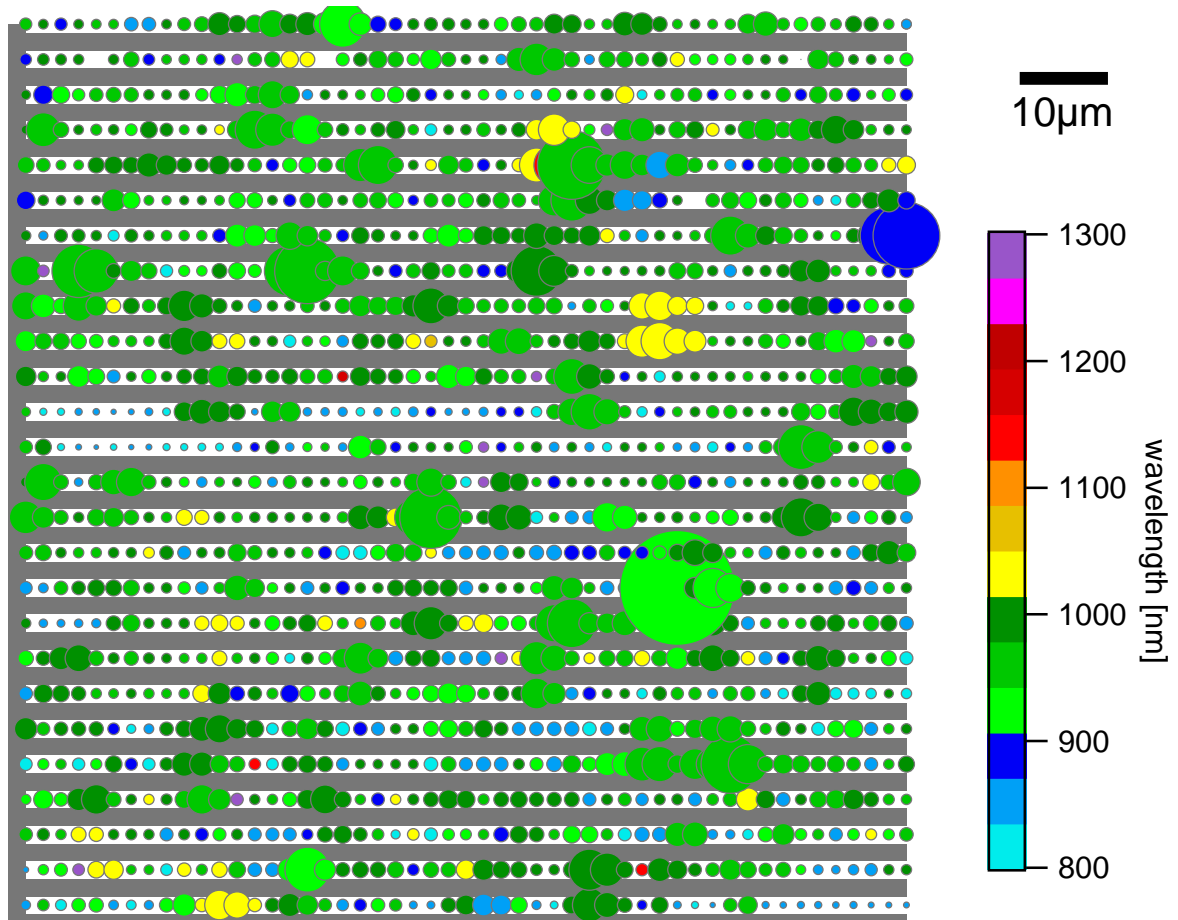
Fig. 49: A complete raster scan with 2x4μm spacing over 100x100μm with the silicon detector. The circle size indicates the maximum intensity of the spectral emission, and colors indicate the central emission wavelength of the excitonic signal.

of 550-725nm, it is also possible to cover a wide range of chiralities. The downside of this approach is the enormously long scanning time per detector. An area of 100μmx100μm requires 1326 spectra to be taken. Depending on the exposure time per spectrum, which is typically 15s, such a scan can take 5.5h for one detector only. Scanning a sample area of 300μmx300μm with the same exposure time using two detectors would, therefore, require measurements over more than four days and can only identify a fraction of the sample.

Image Scan
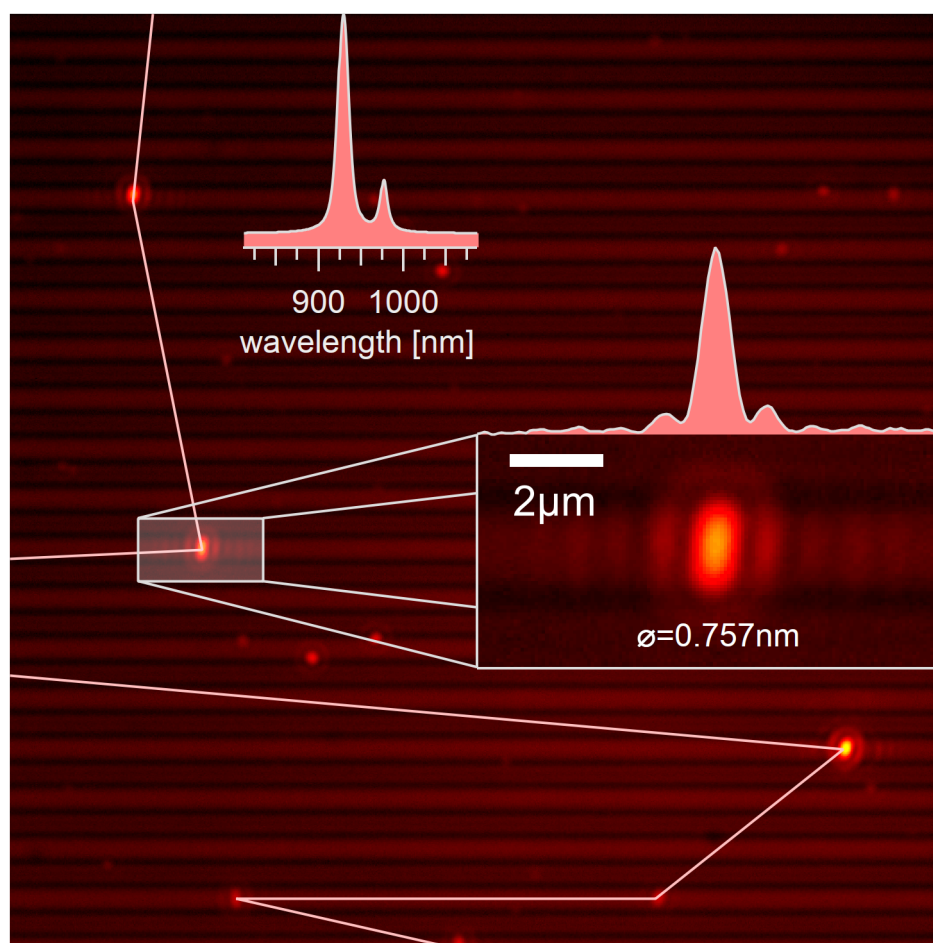
Fig. 50: The image is the base information on which a trench scan with rough nanotube positions is performed. The exact positions of the nanotubes are identified with a scan around the position from the image.

Given that the acquired positions always require an additional scan to determine their exact position, only the intensity of the acquired spectrum contains valuable information for the initial scan. An image can give similar information within a smaller time domain and with the use of fewer resources. Images also have the advantage of identifying suspended nanotubes easier as their distinctive emission is homogeneously distributed over the pit. At 660nm, excitation with the 660nm dichroitic beam splitter also attached a

characteristic airy stick Bessel function pattern is visible along the axis. The periodicity of the Bessel function can also be exploited for better identification of suspended carbon nanotubes in a large picture when applying a Wigner distribution to separate the phase space pattern along the trench. The maximum visible intensity of theses images also correlates with the spectral maximum of the excitonic emissions when taking spectra at these locations. Images are, therefore, always a must when identifying suspended carbon nanotubes and should be taken first to minimize processing times.

Exact Scan

Fig. 51: The exact scan technique is a scan along the trench. Eleven spectra are taken around a rough position with the goal of identifying the exact location of the single-wall carbon nanotube from the image. The scan in this image is ordered by the intensity with features of the highest intensity located on the right side.

After finding the rough position of a carbon nanotube, 11 spectra around that position are taken with 0.25μm spacing, and the rough position centered using a broad excitation from 550 to 725nm. It has to be mentioned that the z position for these coordinates can be calculated from the already measured tilt plane. Each of the acquired spectra is manually analyzed to determine the exact position of the nanotubes within 0.25μm accuracy. The fairly narrow excitonic emission spectrum from the E_{11} state also allows for rough identification of the chirality.

Most carbon nanotubes have their emission in the SWIR range, but although the number of visible nanotubes in this range is higher, their peak area is generally also smaller by
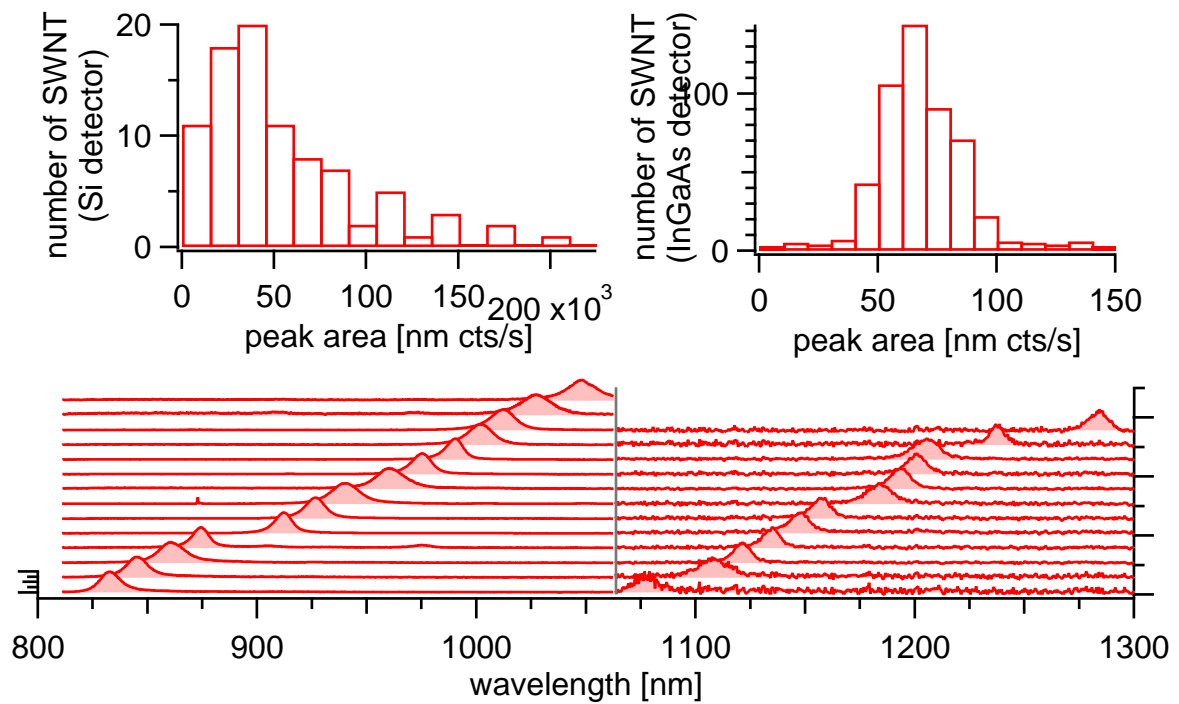
Fig. 52: Overall smaller peak areas are accomplished with the InGaAs detector if the spectra are normalized to the exposure time. The detection area for both detectors is roughly the same, and the quantum efficiency within the measured range is generally higher by one order of magnitude for the InGaAs detector. Thermal (Johnson) noise and low signal digitization lead to these general culprits of the InGaAs detector.

three orders of magnitude. The peak area was measured on the wavelength axis and is expected to be even more on the energy axis. The adsorption measurements in solution are sensitive to emission drops and require a high resolution of the nanotube emission intensity. Considering the inferior emission properties in the SWIR range, only nanotubes from the NIR range were used for adsorption measurements.
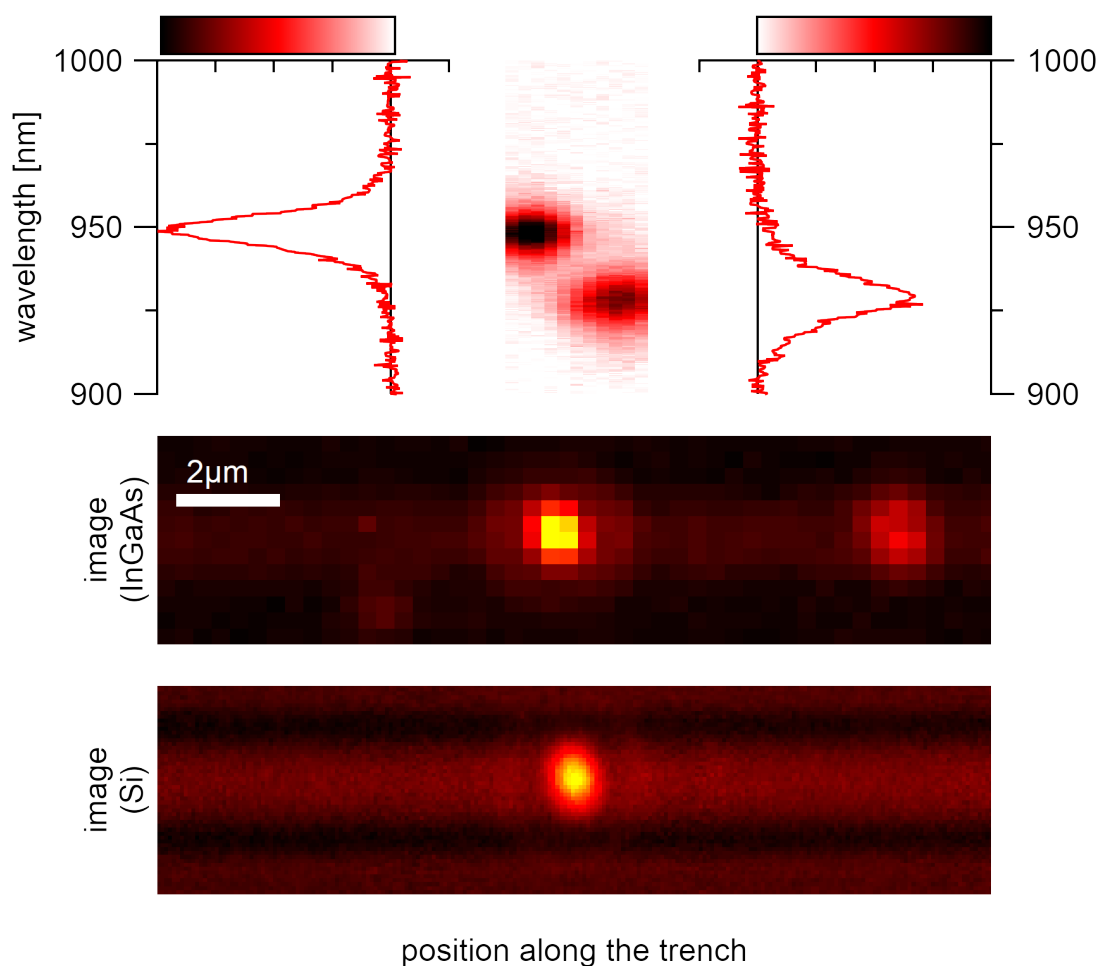
Fig. 53: Two nanotubes that seem like a hetero aggregate when taking image and spectrum at their mean position. Using the exact scan technique, it becomes evident that these nanotubes are the (9,1) type at the right and the (8,3) type in vicinity emitting at a similar wavelength.

The spatially resolved acquisition of spectra allows differentiating between the emission from bundled and unbundled nanotubes locally. Even though the spectrum from the position that was determined by the camera images can show two excitonic peaks, this does not necessarily mean that these nanotubes are bundled. The resolution limit of the light microscopy is simply not enough to clearly differentiate the two emissions, and their spectra merge and overlap to a combined emitter. The spacial information also identifies carbon nanotubes of the same type that are in close vicinity to each other, which is not visible from the pure spectrum but can significantly disturb single molecular spectroscopy as any resulting adsorption measurement would include the combined emission from two

nanotubes. Nanotubes located in close vicinity ($<2\mu$m) to the same and other chiralities are typically excluded from further analysis.

2.8.3 Analysis

The chiral assignment of a single spectrum is nearly impossible and often leads to mistakes. A wide range of publications have reported chiralities differently which is why today mostly statistical analyses are performed for single molecule measurements. If not done on a comparative base to other single spectra, the interpretation about the diameter is vague. Not differentiating between nanotubes suspended in air and nanotubes in vacuum has been found to be the most prominent mistake that is handled in its own chapter. As shown in the following graph, these mistakes can not be avoided using photoluminescence-excitation spectroscopy solely.
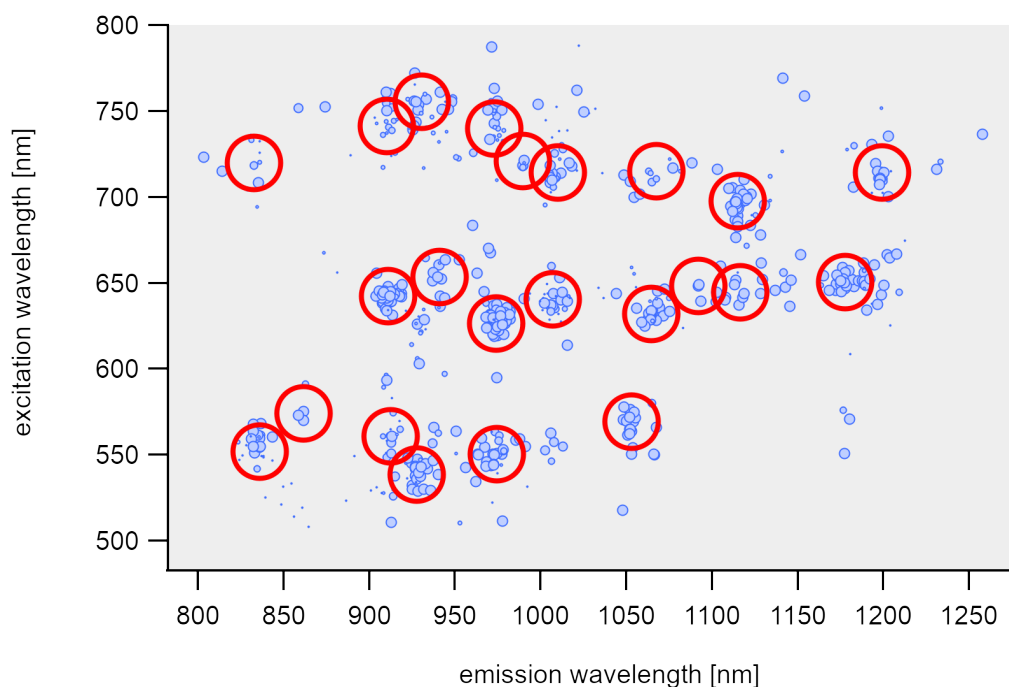
Fig. 54: A peak fit shows that the photoluminescence reaches a maximum for specific excitations. These positions originate from different chiralities. Their distinct assignment needs further elaboration.

The selections of best spectra and best PLE maps are available online.

A red-shift of the signal can either be allocated to defect generation [157], the dielectric screening of bundled nanotubes [158] or to a change in the outer dielectric environment [159].

The graph above shows a collection of best measuerements. All are of best quality from an extracted dataset and considered mostly unbundled. The measurements show an inhomogenious set of nanotubes with certain statistical evident peaks in the clustering.

K-means clustering should be performed here so the fitting routine needs to be improved to better match the maximum PLE intensity but a grouping into distinct spots is visible. I want to address the reason for this inhomogeniousity in more detail here and in the next chapter. The formation of bundles during a measurement can be neglected and the concentration of nanotubes on the sample was helt low to minimize intrinsic bundling.

As intrinsic bundling as the effect of emission quenching can be excluded here, I want to discuss defect generation in this chapter which is an inherent problem in these measurements. Time-dependent measurements of the photoluminescence from one suspended nanotube on the sample have already shown different effects. Suspended nanotubes are known to undergo irreversible blinking due to photoinduced oxidation [147] upon laser irradiation. This generally also broadens the collective excitonic emission due to a mixing of local defective states with lower energies. At laser powers of 70μW on the sample, the emission intensity rapidly but continuously diminished. The bleaching is accompanied by a correlated red-shift of the emission energy and broadening of the FWHM. Strong r values support this finding. A statistical analysis of the involved peak features can, therefore, help to find a sufficiently low excitation power that avoids irreversible defect formation. In the following chapter in air, the power on the sample was kept below 10μW (laser spot 2μm). These samples show a reversible effect in energy and bleaching that is addressed in more detail in the following chapter.
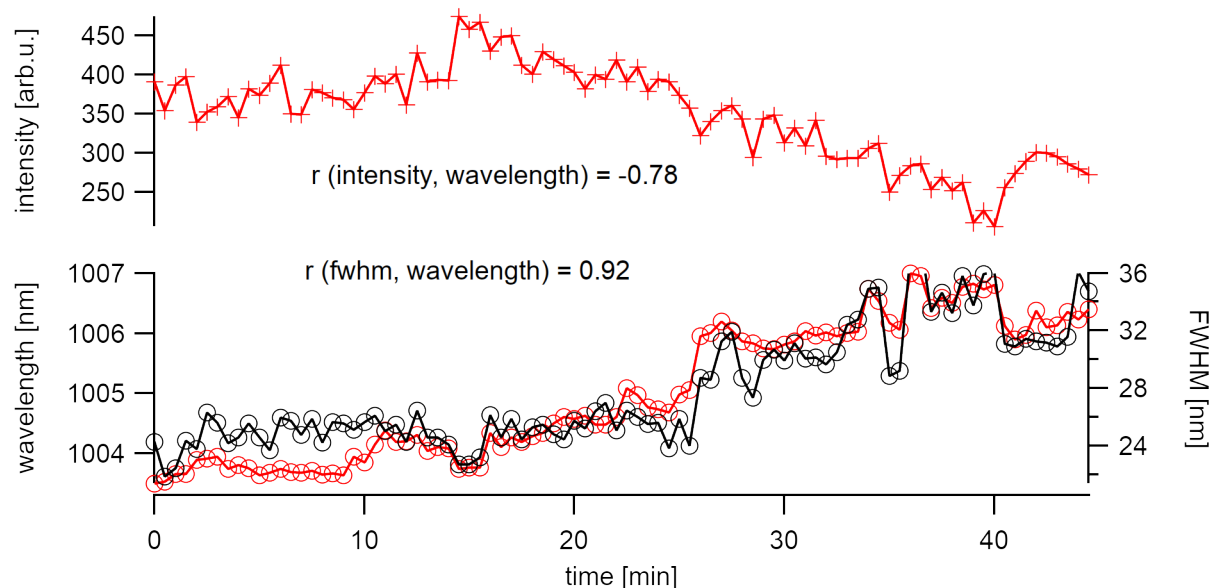
Fig. 55: Bleaching of the photoluminescence at 70μW laser excitation strongly correlates with peak broadening and a shift to lower energy. The bleach happens on a rather rapid time scale with a half-life decay of τ=10min.

The emission energy of a carbon nanotube is not stable in energy over time when observed at low exposure times. This behavior is more widely known for low-temperature measurements [13] where excitons are better localized. However, it has also been shown to apply

for room temperature measurements.[136] Bleaching is continuous emission depleaching with strongly correlated broadening of the FWHM at high excitations. Bleaching is usually considered irrreversible. In some samples, it is evident that the emission wavelength and FWHM are not anti-correlated with the intensity. This especially occurs at low excitation powers. The discussion of these effects and their impact on the measured spectral distribution will be the topic of the next chapter. Knowing about these changes to the emission energy will also help to assign specific chiralities.
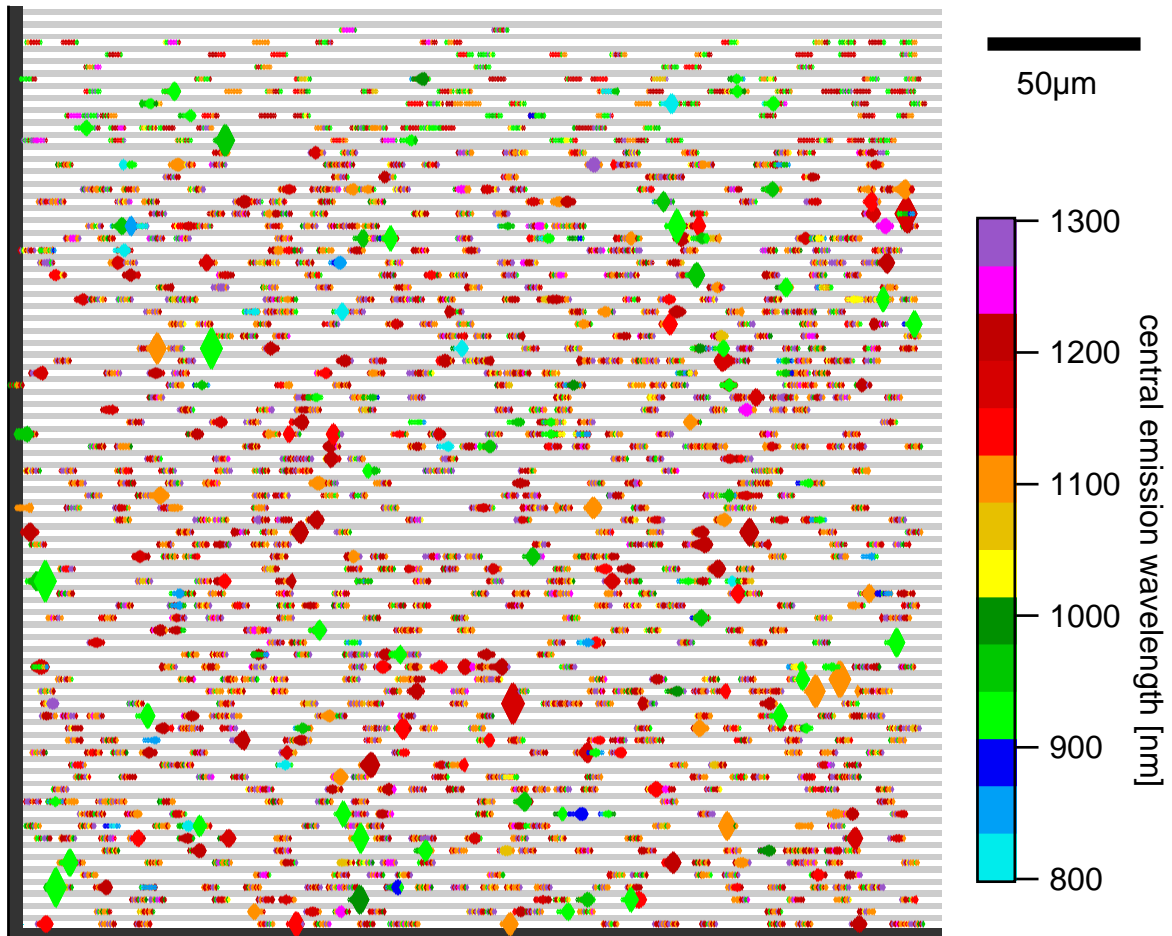
Fig. 56: The exact scan technique allows us to fully characterize, a sample area of $300\mu m \times 300\mu m$ in a short amount of time. The found locations of these nanotubes are the base for further analysis using subsequent experiments where only a fraction of these nanotubes will survive, and their emission strength is significantly reduced.

Nevertheless, recent investigations demand that measurements like the ones present in this study need to be carried out under a protective gas environment. Such changes in the setup design allow to increase the excitation power and thus the emission intensity and reset the system to a save desorbed state without bleaching.

2.8.4 Conclusion

The "exact scan" [136] is an essential technique for finding suspended nanotubes. With the performed alteration, mostly automated analysis of a single sample becomes feasible, which is only limited by the range of the nano stage. Such extensive analyses usually take long time scales to perform. The suggested method yields better results within a smaller time frame giving access to a large pool of suspended nanotubes. Only nanotubes with the most vigorous emission intensity and best camera images from this selection are chirally identified using photoluminescence excitation maps and used for further investigations.

As the emission intensity is significantly reduced in solvents, and it is also crucial to reduce the excitation power, such experiments are only possible with The Perfect Nanotube. The definition of a perfect nanotube can be that it is of a pristine surface, which is discussed in the next chapter. A perfect nanotube may also be a tube that can survive destructive methods such as the ambitious wetting process in the chapter following. The here described method is crucial for selecting the carbon nanotubes that are suitable for carrying out experiments on.

SURFACE ADSORPTION
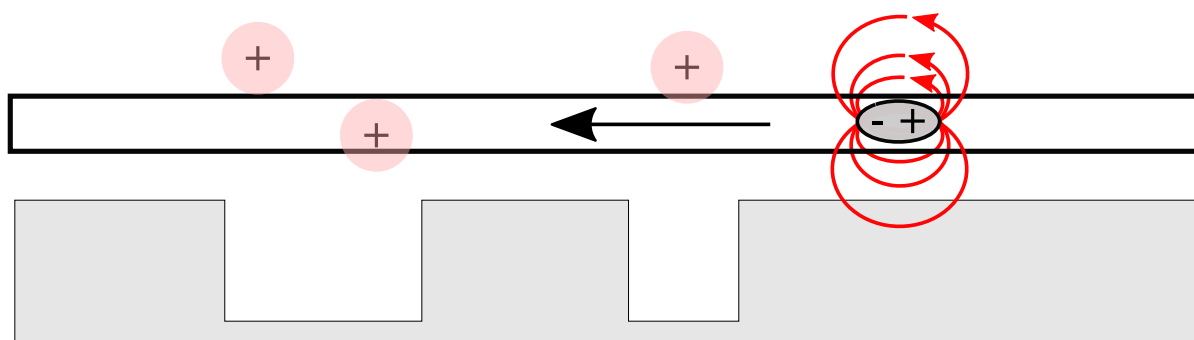
Fig. 1: Changes on the surface of a carbon nanotube form trap states that lead to a non-radiative decay of the excitonic state and changes in the dielectric surrounding influence the exciton energy.

Interactions with the surface of a carbon nanotube are predominantly dispersion (London) interactions.

These strong intermolecular forces are responsible for stable suspensions of carbon nanotubes in various solvents where non-covalently bound surfactants are wrapped around the nanotube. Such wrappings prevent bundling and preserve the excitonic emission features of carbon nanotubes in solution and films over months. The exact mechanism and the kinetics of surfactant sorption on the surface of carbon nanotubes is rather complex and not fully understood [7] as it usually includes concomitant effects. The separate study of such effects is important and will be delved deeply for the Adsorption of Solid.

A downside for the use of surfactants is that a significant percentage of photoluminescence quantum yield is lost [160] to exciton quenching at the sites of adsorbed solvent and surfactant molecules. Placing carbon nanotubes in solvents is, however, inevidable for most wet processing methods or for contacting nanotubes to electrolytes. The effect of the Adsorption of Liquid is therefore handled in more detail in its own chapter.

The use of surfactants reduces and alters the available free nanotube surface. A clean surface, however, is required for sensing molecular interactions [161]. A clean surface serves as a clear reference point for studies on the adsorption process. The search for this

initially clean surface and its definition as a reference is discussed in the Adsorption of Gas.

3.1 Adsorption of Gas

Carbon Nanotubes show strong adsorption to gaseous molecules like nitrogen dioxide [162][163], carbon monoxide, ethylene [163], ammonia [162][164][161], oxygen [165][166], noble gases [167][168], methane, or molecular nitrogen [168] and have therefore been discussed for their usage as gas sensors. The advantage of carbon nanotubes over commonly used sensors is that they can be operated at room temperature, do not corrode, and - due to their confined structure - offer large surface areas for the adsorption of molecules with good coverage percentages and high response speed.

In addition to its use for sensors, the same adsorption has been demonstrated to be applicable for non-volatile optical memory [169]. Even though there are better materials for this purpose, carbon nanotube-based systems offer state stability over long time-scales without continuously applied voltage and stepwise intensity changes that are ideal for storing bitwise information in a nanometer-scaled system.

Their binding mechanisms generally differentiate two types of adsorption. The dispersion interaction of carbon nanotubes with different molecules allows strong physisorption of water or ethanol. These molecules can reversibly be released by lowering the pressure [170] or increasing the temperature [169].

The high amount of double bonds in carbon nanotubes allows various chemical functionalizations [171][172][173][174]. If these reactions are completely reversible without damaging the carbon network, the process is called chemisorption. The saturation of C=C double bonds using hydrogen was proven to be reversible at temperatures of 600°C [19] and can, therefore, be considered a chemisorption process even though permanent damage to the nanotubes was also reported.

In the following, I will discuss the release of the physisorbed layer that is inherently present if carbon nanotubes are investigated in air. I will also discuss the influence of chemisorbed hydrogen to the excitonic emission.

3.1.1 Adsorption of Water

Carbon Nanotubes not kept under a protective atmosphere, contain a shell of adsorbates on their surface. Right after carbon nanotubes are synthesized, they are statically charged, which favors the adsorption of various adatoms. In air, this layer is usually considered to consist of water [100]. It is also reasonable to assume a layer of argon or molecular nitrogen that adsorbs directly after synthesis as such atoms are known to show similar adsorption as water [175]. However, it is not of too much relevance for my experiments what molecules this layer is composed of exactly but rather how it influences the experiments and how it can be successfully removed not to act disturbing.

All experiments were carried out under the usual oxygen-containing atmosphere. A continuous degeneration of the nanotube surface due to the reaction with adsorbed oxygen is possible at any point.[147] Therefore, the excitation power was kept at around 3-7μW (25nm bandpass) to reduce the irreversible introduction of oxygen defects. The chosen power is at least one order of magnitude lower than in other similar experiments. Because of this defect generation experiments with suspended nanotubes are usually carried out under a protective nitrogen environment.[169] The irreversible degeneration of the emission due to oxygen defects will therefore always have to be considered during the following investigations.

Total Energy Shift

In vacuum, excitons in Carbon nanotubes are influenced by an intrinsic dielectric filling around 70% of the inner cylindric volume of the nanotube with $\epsilon_{\text{in}} = 3.25$ and a dielectric medium surrounding the nanotube with $\epsilon_{\text{env}} = 1.26$ [100]. Gas adsorptions on a clean surface induce a change in this outer dielectric environment. This change in the dielectric constant influences the prefactor of the Coulomb energy and causes a shift of the excitonic emission energy to the red.[176] Changes in the cylindric dielectric surrounding can be calculated using approximations to the Bethe-Salpeter equation.[177] They are found to cause a modification of the excitonic binding strength E_{b} in the system by $E_{\text{b}} \propto \epsilon^{-1.4}$ and scale inversely with the diameter d of the nanotube.[178] Thus, by observing the excitonic excitation and emission energies, it is possible to detect changes in the dielectric environment.

Analyzing a sufficiently large set of suspended carbon nanotubes consisting of chiralities with different diameters, it becomes evident that there are satellite peaks slightly redshifted to the emission from the first and second excitonic subbands. These emissions each originate from a distinct PLE map that shows resonance to a specific excitation/emission energy, unlike every other nanotube. The existence of this second type of nanotubes made the identification of air suspended nanotubes difficult if only a small number of spectra is
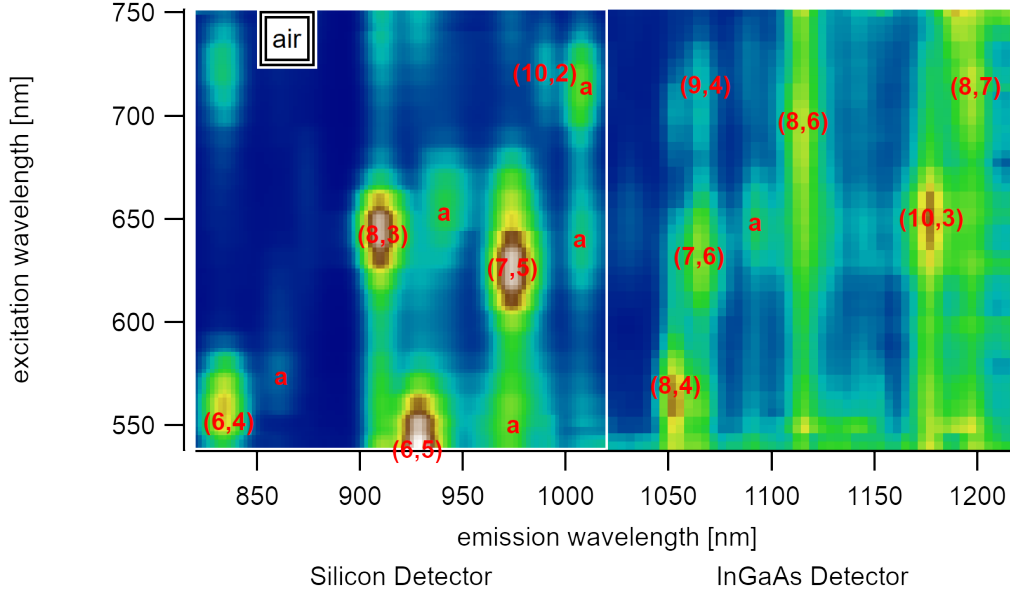
Fig. 2: A variance spectrum shows the squared deviation of the spectral intensity of 350 PLE maps from the mean value. Adsorbed satellite peaks are marked with a.

considered. On better datasets with over 350 good PLE maps in the range between 830-1250nm, however, the satellite peaks can be identified to follow a specific pattern. While carbon nanotubes with larger diameters like the (7,6) type show small shifts of 25meV, nanotubes with smaller diameters like the (8,3) type show much higher shifts of up to 65meV. The shift can be interpreted to depend inversely on the diameter, but the dataset size (consisting of 6 chiralities) is too low to make assumptions about the curve form. The energy shift can be explained by the lowered exciton binding energy after the introduction of adatoms. To facilitate a more visual model, the diameter dependence could be caused by the higher penetration of excitonic electrical field lines into the dielectric surrounding.

Adsorbed water is known to cause shifts of 25meV for E_{11}, and 47meV for E_{22} [170]. These changes are proportional to the inverse energy and are therefore sometimes given on a wavelength scale as 34nm for E_{11} and 23nm for E_{22} [179]. The discrepancy of the energy-difference between ΔE_{22} and ΔE_{11} was also found for aerogel dispersed [180] surfactant-free nanotubes and could be explained through stress and strain effects [181] caused by the surfactants. It is reasonable to assume that the overall shift strongly depends on the coverage percentage and the reference of the clean surface in vacuum. The measured adsorbed energies in air are in good agreement with suspended nanotubes reported by Liu et al.[41]. In their analysis, the PLE absorption of the (7,5) type to E_{22} is located at 1.94eV (640nm), and the emission is at 1.23eV (1008nm). This energy is roughly the same as found here (640.5nm and 1007nm) but clearly shows that these suspended nanotubes also had a water layer adsorbed during the measurement. Measurements in air often do not account for this layer [159], which causes successive flaws. Energy comparisons in

newer studies are mostly aware of this adsorption effect.

The investigations by Miauchi et al. [159] were focussed on SWIR active carbon nanotubes with diameters above 0.9nm where the changes to the energy were found to be nearly constant for all chiralities. This study concentrates on the silicon-active nanotubes with diameters below 0.9nm. If the exciton size is approximated to stay constant for different diameters, changes in the outer dielectric become more substantial for smaller diameters as their penetration into the medium is more substantial than for larger diameters. Although data for the (6,4) and (9,1) type are at the lower edges of the detectable range, a diameter dependence is visible. However, for some larger chiralities with diameters above 1nm, the statistical spread of ±10nm for the excitonic peak in the investigated PLE maps does not allow us to differentiate between adsorbed and desorbed states. To fully describe this behavior in more detail, the experiment needs to be performed in a defined environment where the switch between gas adsorption and vacuum is possible. Besides, the measurement range needs to be extended to allow recording more significant data for diameters above 1nm and below 0.7nm. However, the advantages of an investigation of smaller diameters were shown in this analysis.

Table 1: freely suspended SWNT in air

label	chirality	excitation [nm]	emission [nm]	error (exc) [nm]	error (emi) [nm]
a	(6,4)	552	836	15.5	13.5
a↓		720	832.5	13	10.5
b	(8,3)	642.5	911	19.5	9.5
b↑		561	912.5	19	10.5
b↓		741.5	910	12.5	15
c	(6,5)	538.5	927.5	10	13
c↓		755.5	930.5	10.5	12
d	(7,5)	626.5	974	11.5	9.5
d↓		740	973	10.5	12.5
e	(10,2)	721	989.5	17	14
f	(8,4)	569.5	1053	13.5	6
g	(7,6)	632	1064.5	7	7
i	(8,6)	697.5	1115	11	15
i↑		644.5	1116.5	40.5	18.5
j	(10,3)	650.5	1177.5	14	15
k	(8,7)	714.5	1199	31	18.5
m	(9,4)	715	1067.5	3.5	15
↙a	a	574	861.5	9.5	2
↙b	a	653.5	941	12.5	10
↙c	a	550.5	974.5	23.5	31
↙d	a	640.5	1007	9	13
↙e	a	714.5	1010	18.5	13.5
↙g	a	648.5	1092	7.5	13.5

Stepwise Energy Shift

One advantage of having nanotubes fixated on a substrate is that while keeping the emission of a specific nanotube in focus, the direct observation of ad- and desorption of single molecules is feasible. A rapid but continuous shift of the energy to the blue [182][169] followed by a much slower shift to the red is generally observed during heating of nanotubes with adsorbed surfaces [175]. With the results outlined above, a total shift of up to 50nm for smaller diameters should be observable if complete desorption is possible in air using laser irradiation solely to increase the heat on the sample.

Recent studies by Uda et al. have shown that the rapidness of this desorption step can be increased by de-tuning the initial E_{22} absorption to induce an increased resonance during
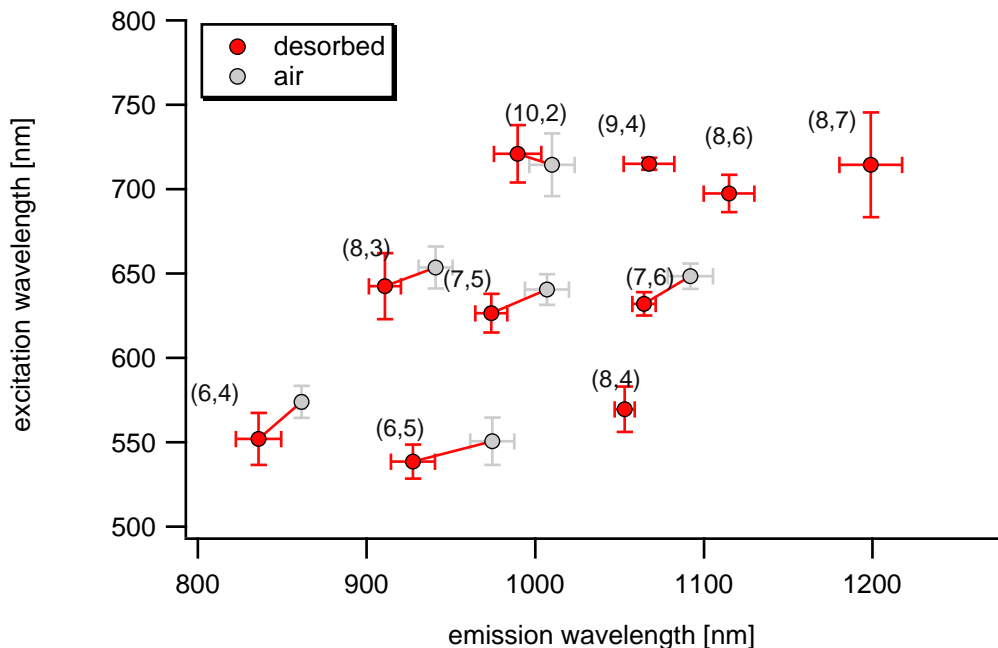
Fig. 3: Carbon Nanotube photoluminescence-excitation resonances for different chiralities in the observed range. This map allows better identification of air-suspended carbon nanotubes that are adsorbed by a water layer.

the desorption.[169] This also means that the heating efficiency usually has to take the absorption cross-section into account.

Therefore, to investigate the desorption process of the water layer in small steps, an excitation into the upper K-phonon sideband of the E_{22} level was chosen, and the emission from the first excitonic subband was continuously observed over two hours.

The (7,5) type in this experiment is excited at 570nm with a power of $7\mu W$ at the sample. The reasonably high reversible steps reduce the emission intensity by 10%. In between these large drops, there are drops of around 3% visible that indicate the formation of quenching centers in the close neighborhood of already existing quenching sites. A simple approximation for these $2\mu m$ long carbon nanotube suggests that the steps originate from large segments of around 200nm that desorb from the surface. Each shift correlates with an energy shift of around 0.5nm. The newly freed surface area is open for further adsorptions making the process fully reversible. The resolution for detecting small gaseous molecules is limited by the considerably long diffusion length, which was estimated to be more than 350nm in these systems.

A type of desorption with a cooperative desorption mechanism is also visible. After the slow desorption of at least three segments of adatoms from the surface without any changes to the emission energy, a swift shift of 3nm is observable. After this shift, the nanotube is still adsorbed with molecules judging from its usual vacuum emission wavelength and the successive steps that occur even after the energy shift. The intensity
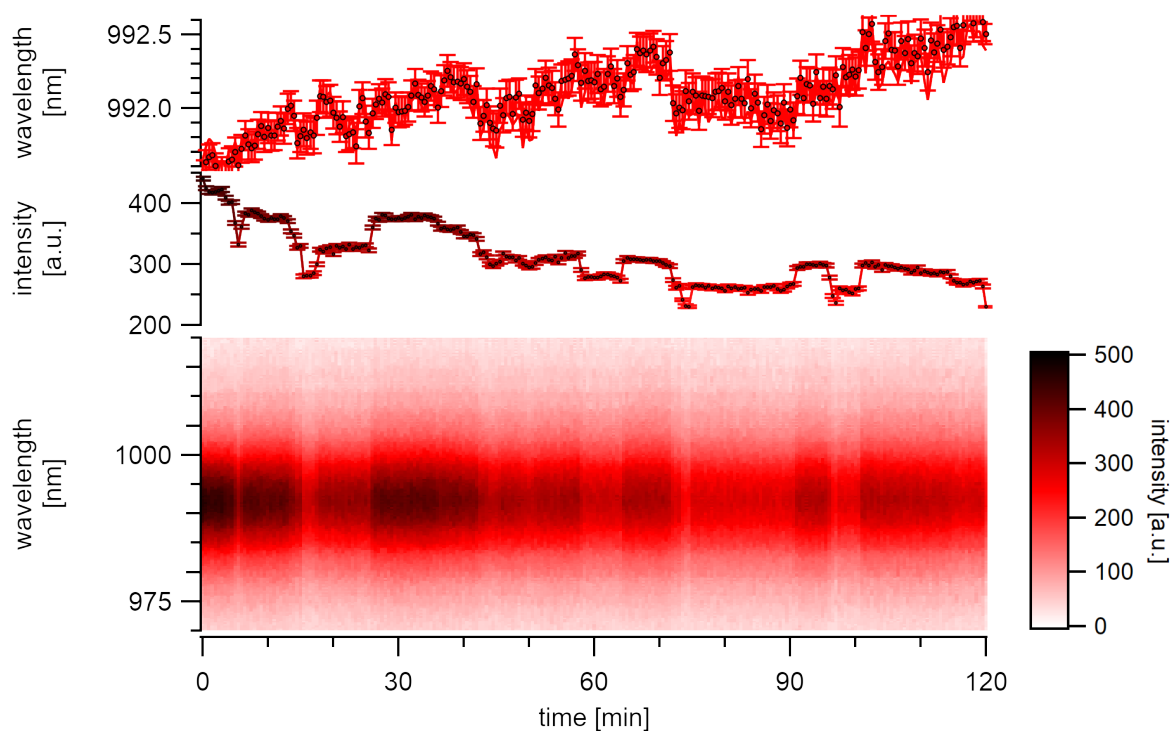
Fig. 4: A (7,5)a type with high emission intensity undergoes continuous stepwise bleaching in air. Changes in emission energy mostly follow the stepwise bleach but also show an underlying continuous redshift.
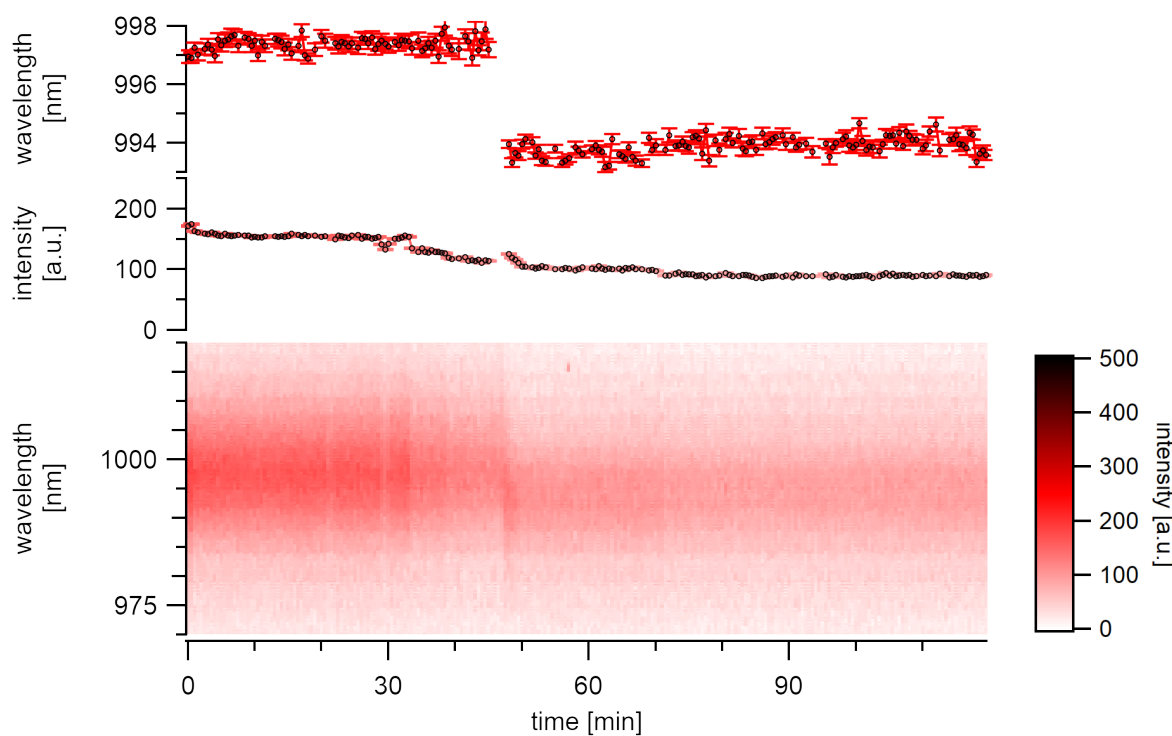
Fig. 5: A (7,5)a type whose emission is shifting towards the energy of its desorbed state. The spontaneous shift is about 3nm to the blue and occurs within less than 30s

bleaching continues until around 40% of the initial emission intensity is lost. After that, no step-wise decreases are visible anymore, and at this point, the emission energy also stabilizes.

Finnie et al. proposed a critical adsorbate coverage that is necessary to induce a shift.[175] Such findings are in agreement with the described stepwise intensity decrease before the blue-shift. The fact that the time series steps do not correlate with the energy before this shift suggest that the gas molecules do only desorb from the surface unto as far as necessary to release the exciton traps. The adatoms are still bound to each other, keeping the dielectric environment in a close distance from the surface intact. The complete release of this cluster finally causes a spontaneous and good resolvable change in emission energy.

Gas adsorption and desorption were studied into detail by Uda et al.[169]: The overall shift in emission energy was estimated to be around 25meV at excitations of 500μW. This gas desorption was found to be reversible in a protective gas environment, and adsorptions could get triggered by lowering the laser excitation power.

The energy shifts in these experiments were found to be mostly smaller than 5meV for the given wavelengths. These small shifts show that the rapid process may consist of step-wise desorption that indicates that the desorption is very slow, and the surface was still covered with gas molecules in these experiments. It may also indicate that the defect generation, which induces contrary shifts, curtains the overall shift. It is notable, though, that the same quick resonant sweep of the emission energy to the blue as described in literature is observed as the last identifiable emission feature indicating the state where all molecules are desorbed from the surface.
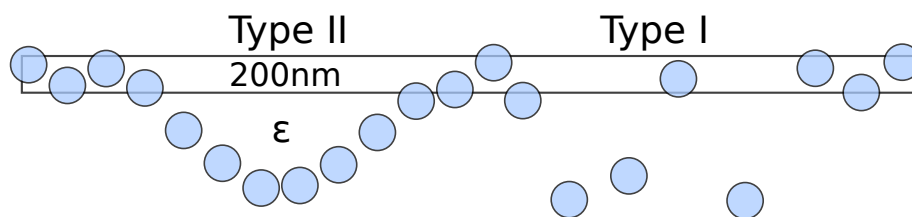
Fig. 6: Two desorption mechanisms can be differentiated: Type I is stepwise desorption with a coverage length far below the resolvable limit, which is given by the exciton diffusion length. Type II follows a cooperative mechanism with coverages in the range of the exciton diffusion length.

The reversible step-wise change in emission intensity is explained by the reversible ad- and desorption of a water layer. The findings suggest that the change in the dielectric environment and the step-wise intensity drops originate from the same desorption process. However, the steps during this process can originate from a correlated (Type I), or a cooperative (Type II) mechanism. After the surface has been thoroughly cleaned from adsorbed molecules, the emission stabilizes in energy and intensity as no further desorption processes are possible. This point is considered to be the adsorption equilibrium at

the given temperature, with the outer dielectric constant approaching 1.

Adsorption In Air

Given that the excitation power is low enough (3μW), neither intensity drops nor substantial energy changes are observed over the same measurement time. Instead, light but continuous red-shifting of the emission center by 0.25nm/h is observed while the intensity stays nearly at the same level. Following the explanation of laser-induced heat, this may indicate the slow adsorption of a water layer.
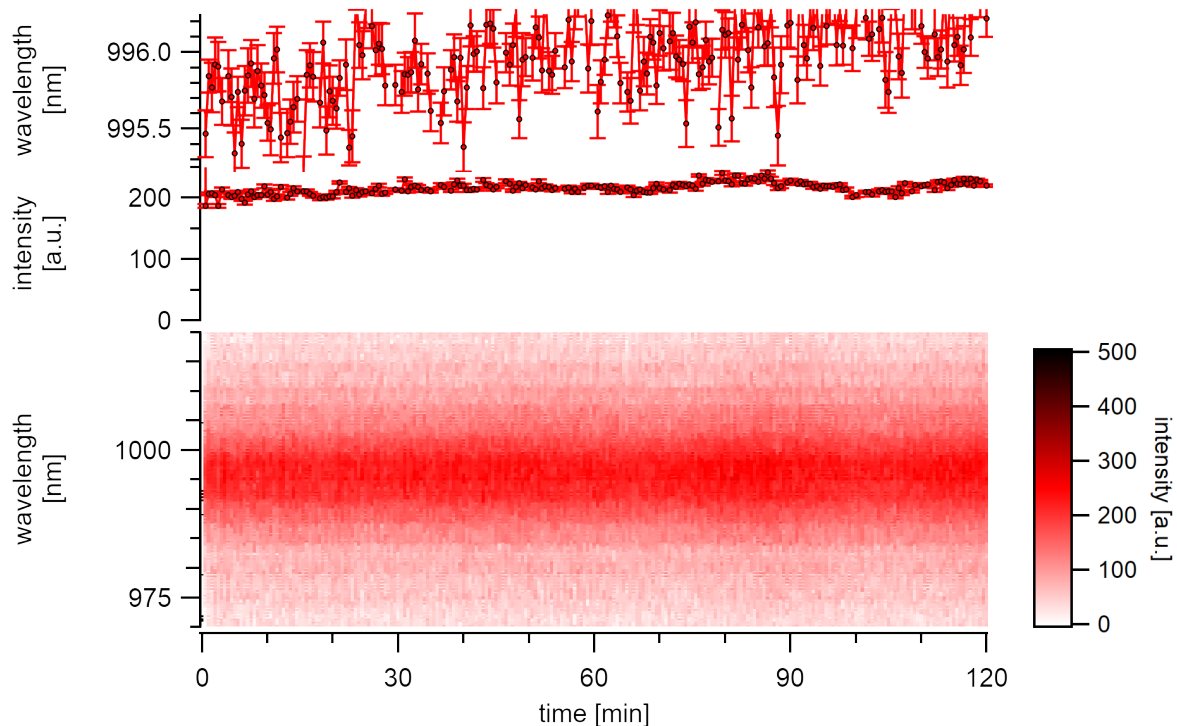
Fig. 7: A (7,5)a type excited below 3μW is stable in its emission intensity over two hours. The emission energy changes slowly but steady to the red.

The influence of heating from the laser excitation can be proven with a simple experiment. The laser is moved along the trench, 5μm around the central position of a suspended nanotube. Spectral shifts of the excitonic emission energy become visible that increase to their highest energy as the laser spot hits the position of the emitting suspended nanotube. These spectral shifts happen within the first 6s of the initial excitation and are only visible if the setup is perfectly aligned (250 cts/s/nm). A gaussian peak fit over this emission shows a fundamental shift of 1-4nm to lower wavelength, followed by a relaxation of up to 4nm to a higher wavelength. The fixed nanotube location and the moving laser focus are taken to estimate the power uptake for each spectrum. At the chosen excitation bandpass of 550-725nm, the power of the laser spot on the sample is 250μW with a diameter (1/e) of 2μm. Assuming a homogeneous spectral weight over the

excitation range, the spectral absorption of the nanotube is estimated to be below 30μW and, therefore, in the linear range. Assuming that the spectra were recorded in the linear range allows for centering the maximum emission intensity of the nanotube (displayed as heat-map colors in the graph) to the intensity profile of the laser.
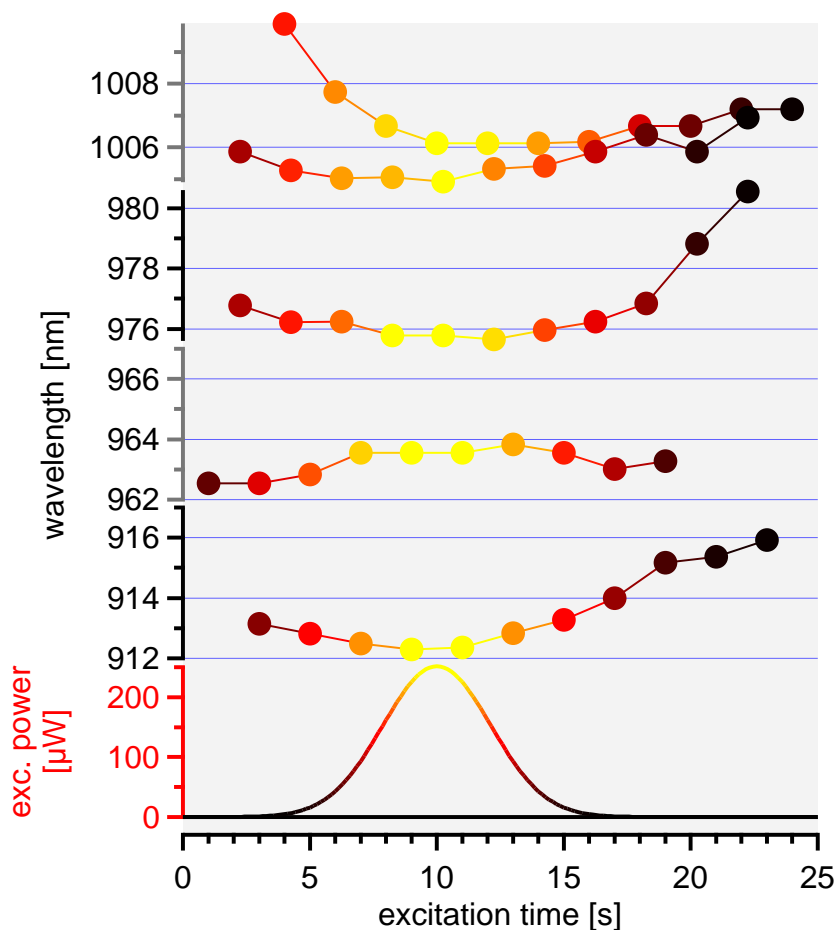
Fig. 8: The central emission wavelength shifts to the blue as the laser reaches the position of the nanotube. After removing the laser spot from the nanotube, the energy maximum shifts back to the red, indicating a reversible process.

Laser-induced heat is responsible for an increased temperature on the sample. Such changes in the available thermodynamic energy leads to reversible desorption and adsorption of the water layer in air. The process is fully reversible and typically happens within a few seconds for high excitation powers.

Conclusion

The adsorption of gas molecules takes place readily after the samples are taken out of the CVD reaction chamber and are inherent to all experiments in air. The laser can thermally heat these adsorbed molecules, eventually overcoming the adsorption energy potential leading to step-wise desorption of these gas molecules. This desorption induces changes in the dielectric environment around the nanotube that cause a blue-shift of the excitonic emission energy.

The rapid blue shift was observed in more detail and is expected to originate from the desorption of large clusters of adatoms from the nanotube surface. These clusters are expected to extend over a few hundred nanometers along the nanotube.

3.1.2 Adsorption of Hydrogen

Chemisorbed hydrogen creates sp^3 defects in the carbon lattice. Calculations using density functional theory show that a high amount of hydrogen chemisorption with coverage values of 50-100% [183] is possible by saturating the C=C double bonds. This chemisorption was proven to be reversible at high temperatures of 600°C [19]. These defects show emission at lower energies than the emission of the E_{11} exciton.[184]

The defined introduction of defects to the carbon lattice is vital for various applications. In biological tissues defect states can be used to achieve better image contrast by efficiently reaching different NIR regions for excitation and emission with higher transparency than in the visible range.[15] In addition, single-wall carbon nanotubes have shown photon anti-bunching [12] in the wavelength range for fiber optic communications which enables their usage as single-photon emitters. However, carbon nanotubes exhibit a relatively low quantum yield of 1% from various non-radiative exciton decay channels. The localization of excitons at defect sites is able to increase the quantum yield [149] which has been shown to also be usable for photon antibunching [16]. Carbon nanotube-based light sources are considered ideal systems for quantum cryptography applications [18]. Investigations on defects and their synthesis conditions are, therefore, essential for the understanding of these systems.

Synthesis

The effect of hydrogen on carbon nanotubes strongly depends on the temperature. Atomic hydrogen is always part of decomposing ethanol [84] at the synthesis conditions of carbon nanotubes (>750°C). A significant amount of atomic hydrogen atoms are generated at the decomposing steps [87] before splitting the C-C bond [86]. Hydrogen is known to help to heal sp^3-defects [185] and is preserving the sp^2-carbon lattice down until temperatures of 500-600°C.[19][186] Below this temperature, it is possible to hydrogenate arylic carbon systems until around 450°C catalytically [187] but also desorption takes place. This leaves a small hydrogenation window at around 450°C, where the introduced chemisorption is kinetically stable on short exposures to the temperature. The direct generation of atomic hydrogen in plasma or with a hot tungsten wire would be more favorable.

Suspended carbon nanotubes were prepared using a typical ACCVD procedure with mixed molybdenum/cobalt catalyst on silicon wafers at 750°C to study the effect of chemisorbed hydrogen. A mixture of 3% hydrogen in argon was introduced after synthesis during the rapid cooldown of the reaction chamber to ambient temperature. The synthesized nanotubes are then analyzed in air and compared to evenly prepared samples where a flow of 100% argon was used as a reference.

Intense Sidebands
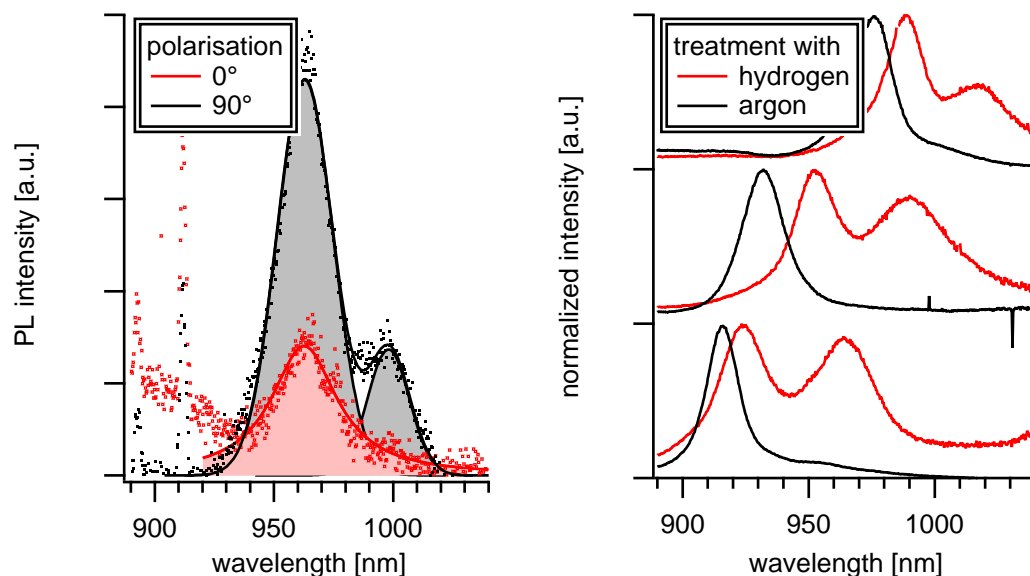
Fig. 9: Hydrogenation produces carbon nanotubes with an excitonic emission that is red-shifted to the usual vacuum level. The sideband shows polarisation dependence which proposes a phonon-assisted process.

The nanotubes show a moderately intense emission from their excitonic E_{11} state that is red-shifted by 15-20meV compared to the average emission in a vacuum. As outlined

above, the emission of excitons is sensitive to the dielectric surrounding. Statistical analysis confirms that the central emission energy is shifted for all nanotubes on the samples, regardless of chirality, which means that hydrogenation causes a fundamental change in the dielectric environment. The suspended nanotubes show a second peak slightly red-shifted to their E_{11} level. The sideband also has the same polarization dependence as the main peak and nearly vanishes if the excitation polarization is rotated by more than 45° from the nanotube axis.

By studying a single nanotube spectrum, it is not evident if two peaks originate from two nanotubes with a similar diameter or if the peaks are an intrinsic feature of an unbundled, single nanotube. Such differentiation can be accomplished using statistical fluorescence spectroscopy [188]. The most promising technique to show if two bands always show up together is correlation spectroscopy. In NMR spectroscopy (COSY) it is typically used to identify spin coupled cross peaks[189][190]. The very same technique was shown to be useful for the analysis of large amounts of single nanotube spectra[191][192].
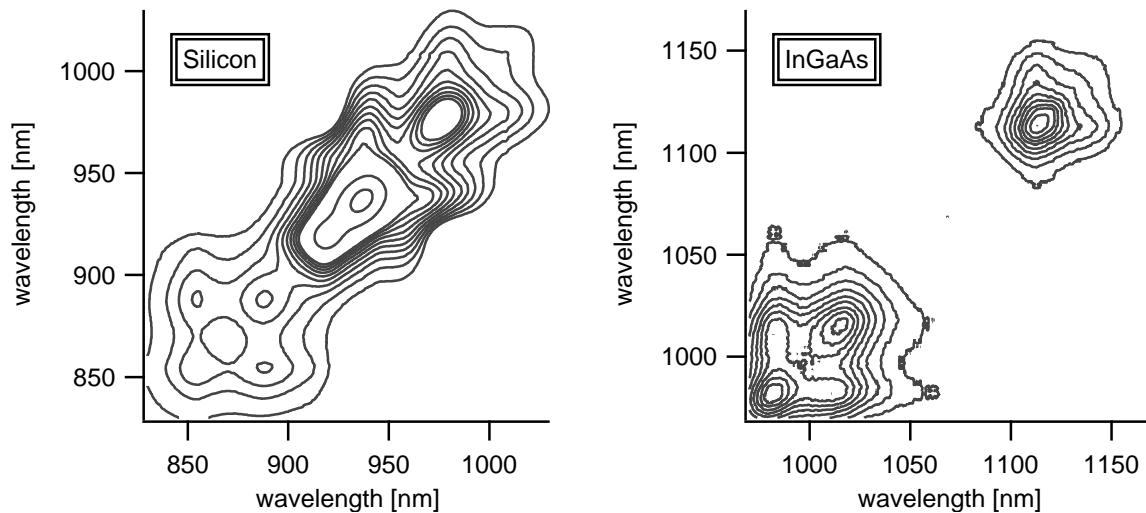
Fig. 10: A contour plot of the symmetric spectral covariance for one sample shows mouse ear-shaped correlated peaks slightly red-shifted to the excitonic emission. Left: Silicon detector Right: InGaAs detector

For the relevance of this statistical analysis, I assume that bundles consisting of two different chiralities are equally distributed over all chiralities, and correlated bundling to a specific chirality is unlikely. In addition, the synthesized samples show large spacing between the positions of the nanotubes, which allows assuming that a significant amount of unbundled nanotubes exists in the measured data set. With these reasonable assumptions, the analysis clearly shows that every nanotube that is synthesized by the hydrogenation process shows sidebands. With this analysis, bundling can be excluded as the origin of these bands. The spectral autocorrelation also underlines the observed energy shift of the E_{11} levels for all chiralities.

A disadvantage of correlation spectroscopy is that all peaks get weighted by their intensity, and spectra with close energies get merged. Although this can be overcome by measuring the spectral skew using the third momentum of the distribution[193], it is also evident that the direct analysis of every single spectrum using a peak fit is the preferred way. For this study, all spectra were analyzed by a custom multi-peak fitting routine to identify the intrinsic properties of every single nanotube without losing information by averaging before the analysis.
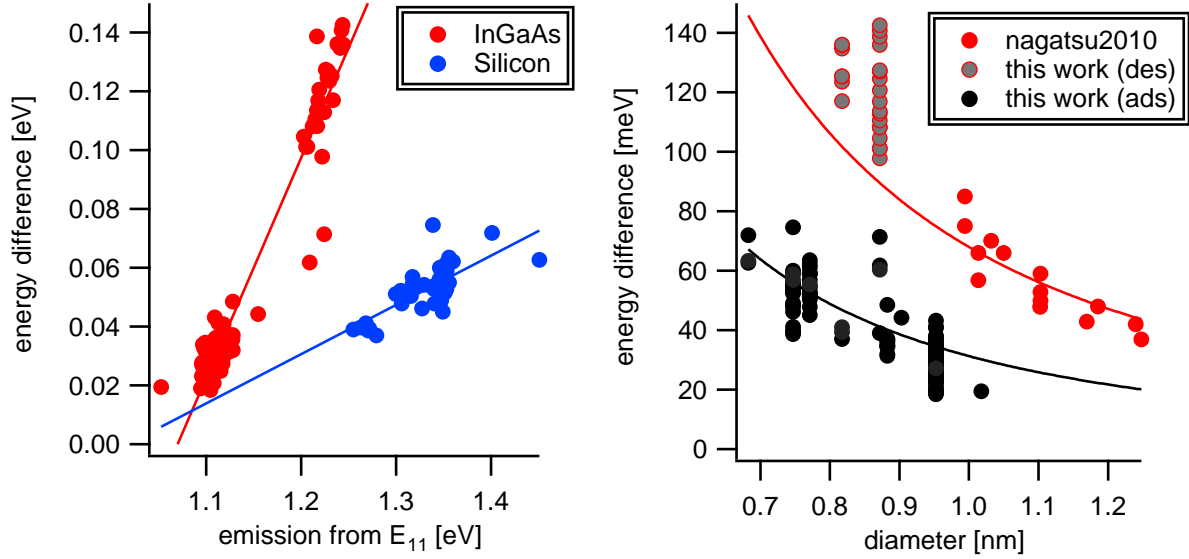
Fig. 11: The correlated sideband shows a near-linear dependence on the energy of the bright exciton. The emission from the sideband shows an inverse quadratic dependence on the diameter of the nanotubes. The effect is found to be lower in air compared to experiments measured in vacuum by Nagatsu et al.[184].

Dark Excitons

The correlated side bands show shifts of 20-140meV. Within this vast range, various origins are possible. The polarization dependence suggests a phonon-assisted process, but a synthesis using ^{13}C is needed to substantiate this finding further. While the HEM (G-Band) at 200meV and the defect band (D-Band) at 160meV [194] are too high in energy to be involved, a coupling to the RBM at 21meV would not explain the higher sidebands.

The lower K-phonon sideband (KPS) is located at 130meV [195] and is often discussed to be involved in the formation of defect bands in arylic and oxygen defects. Arylic sp^3-defects on the sidewall of carbon nanotubes are known to form localized states at 150-266meV [196][197][198] below E_{11} and chiralities with lower diameters show higher shifts than chiralities with higher diameters. Also, oxygen defects from UV/O$_3$ or milder oxidating agents like H$_2$O$_2$, or K$_2$CrO$_4$ can form similar defect bands at 100-200meV

[199][149] and are also found to increase with the E_{11} energy. Also, the cooling of defective nanotubes was shown to brighten the KPS [200].

Due to the enhanced spin-orbit coupling of these sp^3-defects [47][201], a brightening of the dark exciton is usually discussed [184][200] as the origin of the bright KPS bands. A dependence on the inverse quadratic diameter should be visible, to substantiate this suggestion, which was theoretically predicted [3] for the bright-dark splitting using the Bethe-Salpeter equation. For carbon nanotubes in air, a fit to a/d^2 with a=30nm^{2}meV was found to give decent chi-square values. This prefactor is in good agreement with the singlet-triplet splitting proposed by Capaz et al. for adsorbed dielectric environments of ε≈3. Nanotubes with a diameter of 1nm show this band at 40meV and nanotubes with a slightly lower diameter of 0.8nm show the band at 60meV. The nanotubes in this sample set are considered to be physisorbed with a water layer that sometimes desorbs due to laser heat. Acquisitions with the InGaAs detector typically take long exposure times, which is why almost no adsorbed states are observable in these PLE maps. The higher energy differences that presumably originate from the desorbed states show more agreement with the suggested curve that was found by Nagatsu et al. [184] for measurements in vacuum (ε≈1.8). The prefactor a is estimated to be even higher at around 85(4)nm^{2}meV when accounting for the extension to smaller diameters in this study.

Conclusion

Hydrogenation causes a shift of the outer dielectric environment of the bright exciton. A brightening of dark triplet excitons from the enhanced spin-orbit interaction between sp^2 and sp^3-carbon was found to give rise to a new emission pathway slightly red-shifted to the bright exciton by 20-140meV. The energy splitting intensifies for nano tubes with smaller diameters. The results are in good agreement with theoretical calculations and support other investigations on the topic eventually leading to better applications in spintronic devices.

3.2 Adsorption of Liquid

The influence of solvents on carbon nanotube is the most substantial process during the study of carbon nanotubes. Dispersing nanotubes in a solvent allows various wet processing techniques that are necessary for the integration into devices. The dielectric environment of the used solvent plays a significant role as it directly adsorbs on the outer surface of the nanotube. However, solvent influences are often not distinguishable from the natural effect of the wrapped surfactant. Besides, insufficient de-bundling can intercalate solvent molecules between nanotube bundles [202], which makes simple investigations

on this topic nearly impossible. In this experiment, air-suspended carbon nanotubes were placed into different solvents to study the effect of the dielectric environment.

Carbon nanotubes suspended over trenches provide an excellent system for such an investigation. However, the transfer to a solvent typically destroys around 95% of the suspended nanotubes, which is believed to originate from the high capillary forces at the trench sites. The system is, therefore, not ideal for such an investigation. More recently, surface-attached nanotubes were shown to exhibit an extremely narrow linewidth of 0.2meV at cryogenic temperatures [203]. Due to their mechanical stability, nanotubes that are directly attached to a surface seem to be a sound setup for the investigation of solvent effects. However, interactions with such nanotubes are always accompanied by surface effects, and the line widths enormously broaden to around 50meV for individualized nanotubes at room temperature [204] and an investigation in solvent inherently inhibits cryogenic cooling. For best results at room temperature and best comparability to solution-processed nanotubes, thus, air-suspended nanotubes were chosen in this study and placed into three different solvents with varying dielectric constants: hexane (1.89), toluene (2.38), and acetonitrile (37.5) [205]

Such an investigation was previously performed by Miyauchi et al. using a broad laser spot for the illumination of a large sample area [159]. Such an experiment gives a good statistical overview of the process. However, since all nanotubes inhomogeneously differ in their emission energy by different effects like varying water coverage in air or different defect concentrations, the effects on the energy, intensity and line width are impossible to differentiate. A comparison of the emission from the same nanotube before and after the transfer to a solvent will give more accurate insights. The technique for scanning a broad set of suspended carbon nanotubes [136] is crucial for detecting the remaining 5% of nanotubes that survive the wetting process. For the first approximation of solvent adsorption effects, spectra before and after the transfer to solvents were recorded. Other than with the measurement technique by Miyauchi et al., it is possible to exclude unresponsive nanotubes from further investigations. It is assumed that the strong capillary forces destroy most nanotubes at the trenches. The measurement then allows giving the solvation effect for a single nanotube with a still detectable spectral intensity.

It can be shown that the transfer to hexane decreases the photoluminescence intensity to 0.0002% of its initial intensity in air. Such a high value is somewhat reasonable as the aliphatic side chains were shown to play a major role for polymer-dispersions and were suspected of wrapping around nanotubes efficiently.[206] An efficient wrapping process also means that a higher surface of the nanotube is covered with the aliphatic chains which form exciton traps for non-radiative decay processes. Therefore, such a wrapping process could be responsible for the substantial luminescence decrease in hexane. The decrease in exciton lifetime was found by Ohno et al. [207] who measured the fs-time
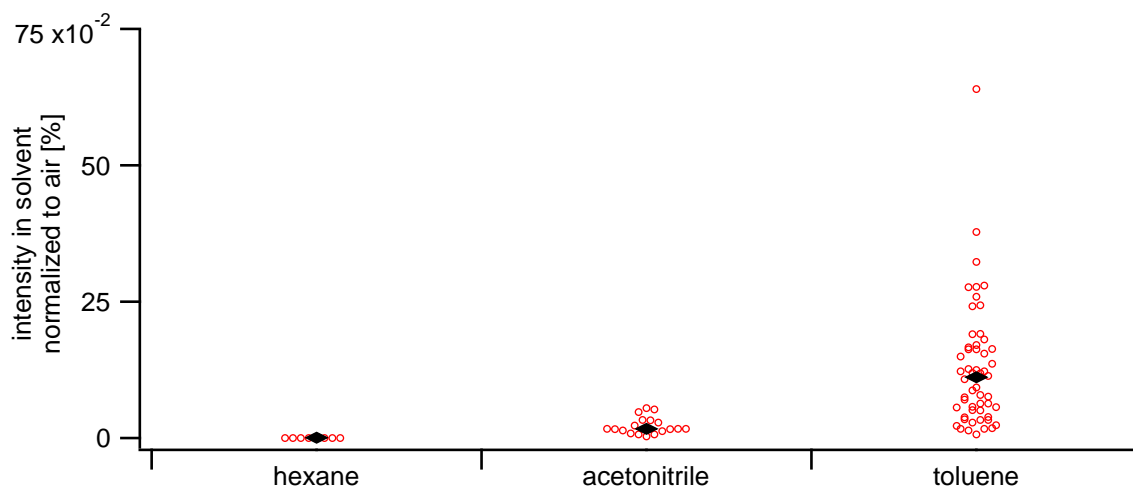
Fig. 12: The intensity drop at the transfer to the solvent was found to be the lowest in toluene compared to acetonitrile and hexane. Diamond symbols show the median of the set while circled dots depict the distribution of individual measurements.

correlation signal and found that it decreases from 293ps in air to 5.1ps in hexane. The intensity in acetonitrile only drops to 1.7%, while toluene shows the best results with a decrease to only 12% of the initial emission in air. Such high values for toluene are in agreement with the excellent emission properties of polymer-based nanotube solutions.
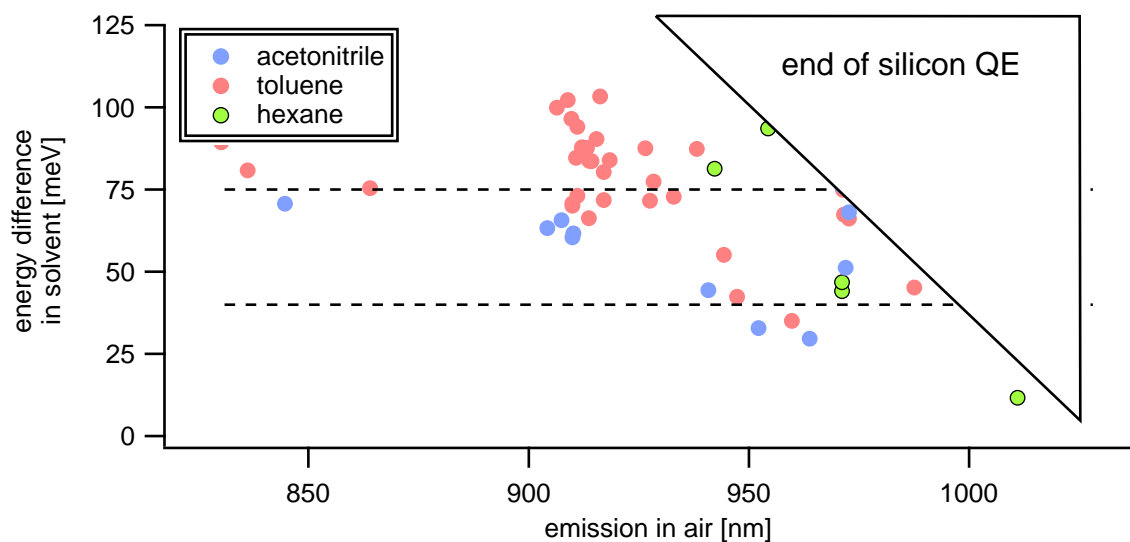
Fig. 13: The peak shift of the excitonic emission energy E_{11} is shown for three different organic solvents with two estimated distribution medians as a dashed line. A chiral assignment cannot be performed for this series.

The energy of the observed nanotubes shows shifts of around 40-120meV to the red. In the effective medium approximation [208], the exciton binding energy strongly depends on the Coulomb energy, which in turn is modified by the dielectric function ε. The energy

of an electron-hole pair with effective mass µ is thus given by the Hamiltonian

$$\mathcal{H} = -\frac{\hbar^2 \nabla^2}{2\mu} - \frac{e^2}{(4\pi\epsilon_0)\epsilon_r r}$$

If the dielectric environment is increased, the Coulomb energy of the particle separation is lowered. This mechanism should lead to a blue shift of the excitonic transition energy. However, it was shown that the free carrier continuum described by the Sommerfeld term [209] is also lowered but with a much stronger dependence on the dielectricum. This splitting is the reason for the redshift of the optical transition energy. Ohno et al. found that the shifts saturate at around ε=4 [207]. Hexane (ε=1.9) should, therefore, show lower shifts than acetonitrile (ε=38). However, this difference was reported to be minimal (1-10meV) [207]. In my measurements, the shifts were almost arbitrarily distributed among all solvents and did not show a significant dependence on the strength of the dielectric environment. The preparation of clean surfaces prior to the investigation in a solvent is thus crucial. Although the observed shifts suggest a saturation even for solvents like hexane leading to unresolvable differences, the shifts compared to air-suspended nanotubes are rather high, and they seem to accumulate at around 40meV and 75meV for all solvents. However, the silicon detector's quantum efficiency hinders a successful investigation for most of the smaller diameter nanotubes.
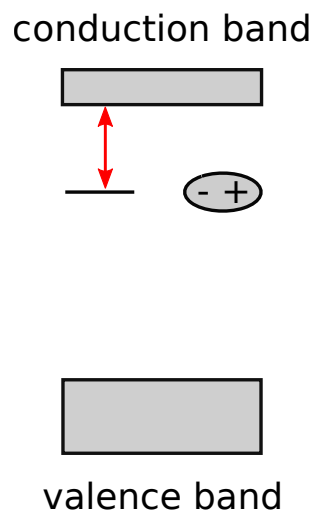
Fig. 14: The Coulomb energy depends on the dielectric medium, and Coulomb forces are responsible for the quantum mechanical exciton binding strength.

The obtained results could help to clarify the discussion [7] on various solvent effects during polymer dispersion of nanotubes. It is expected that the binding of solvent molecules to the surface has a stronger influence than the binding of polymers. The differences in dipole polarizability in the tested solvents also supports other findings for the binding to semiconducting and metallic species [210][211], but further investigations have to be carried out to more substantially make assumptions on the various effects of the solvent

during polymer dispersion.

The measured energy shifts show strong disagreement with previously reported shifts [159][207] of 20-40meV. Without making assumptions about the system, a spectra-based analysis is not enough to fully resolve chirality dependent differences. To shed light on the strong discrepancy between this investigation and the literature, as well as the interesting emission properties in toluene, a more detailed investigation was performed using photoluminescence excitation-emission (PLE) spectroscopy.

3.2.1 Adsorption of Toluene

In this section, carbon nanotubes with purely toluene adsorbed on their surface are analyzed in more detail. Toluene is an essential solvent for dispersing nanotubes with polyfluorene based (co-) polymers with high chiral selectivity, and its influence is under ongoing discussion [7].

Usually mechanical forces are used to separate nanotube bundles and surfactants are used to prevent re-bundling. The following analysis focuses on the line width and energy difference between pristine and toluene-wrapped nanotubes on clean surfaces.
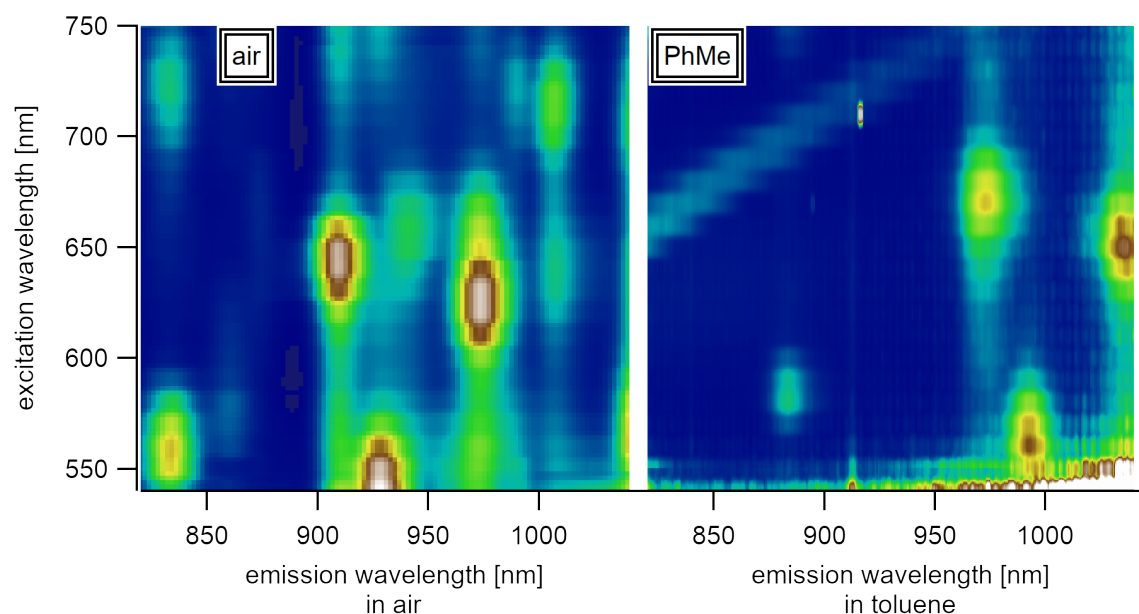
Fig. 15: The excitonic emission in toluene shifts significantly compared to the emission of nanotubes in air. The graph shows the variance of single suspended nanotube spectra in air and in toluene.

The analysis is based on an investigation of full PLE maps of individually suspended carbon nanotubes. PLE maps have already been shown to be a good measure to determine the coverage of the surface with adatoms as they allow exact chiral assignment. It also allows shedding light on the diameter dependence and the exact shift caused by the

dielectric environment of toluene between different chiralities.

Small Line Width

The direct comparison of air-suspended nanotubes to toluene-suspended nanotubes allows estimating the effects caused by the change in the dielectric environment from pure toluene without surfactant influences. The median line width in air is 15(1)meV (13nm). The inhomogeneous broadening in toluene causes a line width of 22(1)meV (18nm). Errors are given as the median average deviation (MAD). The transfer to toluene, thus gives a significant increase in the FWHM by 7meV.
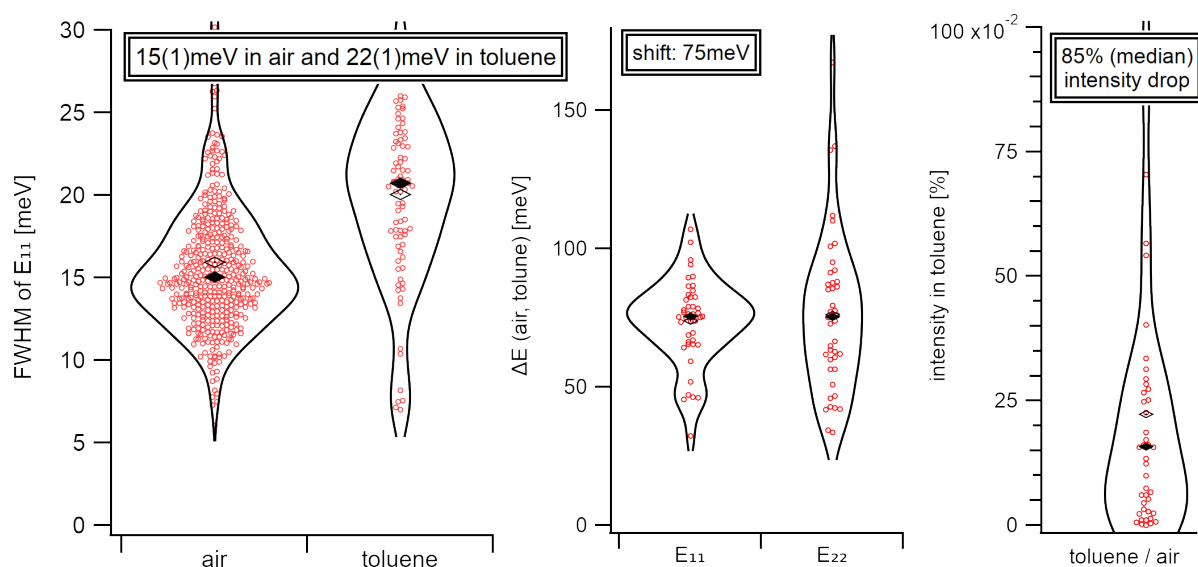
Fig. 16: The overall FWHM of the E_{11} peak increases from 15meV (median) in air to 22meV (median) in toluene (left). This peak broadening is accompanied by a shift of 75meV to the red for both, E_{11} and E_{22} (middle). In toluene, the intensity drop drops to 15% (median) while the distribution maximum is more likely to be at around 5%. The distribution is shown as violin plot which is similar to a symmetrical histogram.

The full line width at half maximum (FWHM) in air is in agreement with the line widths of 12meV [127][139] of nanotubes individualized using surfactants and the range of 10-15meV reported for suspended nanotubes [212] at room temperature. Although, lower line widths of 8nm are reported for individualized nanotubes even at room temperature [156], the line width decreases during cooling [213], and reaches its homogeneous width of 1-0.2meV at cryogenic temperatures [212][214][13][215][17] because of exciton localization. The homogeneous linewidth is also known to broaden from electronic many-body effects like exciton-exciton annihilation (EEA) via Auger recombinations [214]. In this experiment, the excitation power was kept lower than $30\mu W$ (even in solution) as discussed previously to avoid such influences on the FWHM. Microscopy measurements on single surfactant wrapped nanotubes (attached to a surface) show line widths of 24meV in

sodium dodecylbenzene sulfonate [139], and 13meV [216][217] for ssDNA/SDS wrapped nanotubes. However, a detailed investigation on the line width of single polymer-wrapped SWNT showed a widespread between 20-30meV (16-24nm) for an investigation on over 100 chiralities of the (6,5) type [218] which is typical for single-molecule microscopy. Although the experiments in this study were performed in a solvent, the line widths in pure toluene (22meV) are lower than the average value seen in the aforementioned study (26meV). This is expected as these samples suffer from defect inhomogeneously through mechanical processing, partly desorbed surfaces in air, stress/strain and dielectric effects from the surface attachment, and the widespread in length distribution, which by far exceeds the exciton diffusion length. Considering these effects, a comparison with surfactant wrapped nanotubes is nearly impossible. The investigation in this study is expected to be more accurate than any of the previous as the experiment design excludes all of the culprits as mentioned earlier and allows us to estimate the effect of purely attached solvent molecules.

High Intensity

A reduction of the emission intensity accompanies the described linewidth broadening. The emission after the transfer to toluene is reduced by 85% leaving only 15% of the initial emission. The spreading of the observed emission bleach is rather high and may depend on the varying defect concentration in the observed nanotubes resulting in a varying amount of additional exciton quenching sites. The wide intrinsic spread in intensity could also originate from varying reductions of the exciton lifetime caused by a varying solvent coverage. A comparison of the statistical intensity spread in air with the spread in a solvent was not performed as the results from such an analysis could be interpreted ambiguously.

As shown before, nanotubes in toluene are more easily investigable than in other solvents like hexane, as they preserve the excellent emission properties of air-suspended nanotubes. The reason for the bright excitonic emission from carbon nanotubes in toluene might be related to the efficient coupling to the solvent phonon. The coupling comes from the Raman active CH stretching vibration and leads to an efficient luminescence down-conversion. It is tempting to assume that in the laser spot focus of carbon nanotubes in solution, the solvent phonon from toluene might be able to cause luminescence enhancements of the excitonic E_{11} emission at least partly. Such observation is only possible if the nanotube is fixated during the recording of its emission as it usually quickly diffuses out of laser focus [219] during a recording.
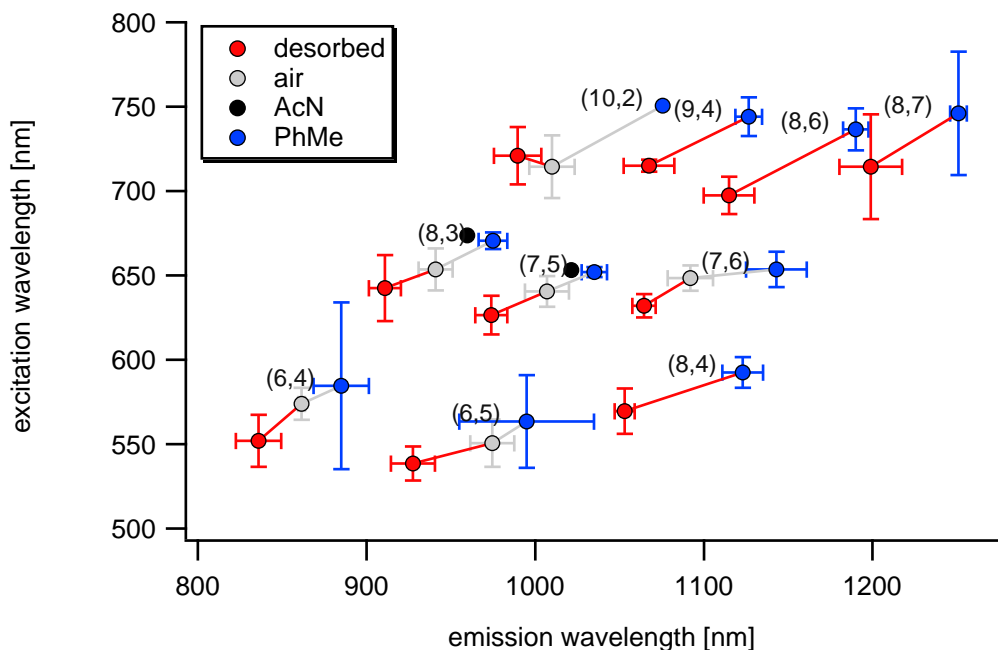
Fig. 17: The figure shows the shift of the excitonic transition energies to lower energies upon the transfer from air to toluene. The nanotubes in air are clearly assignable into two classes that experience two different dielectric surroundings.
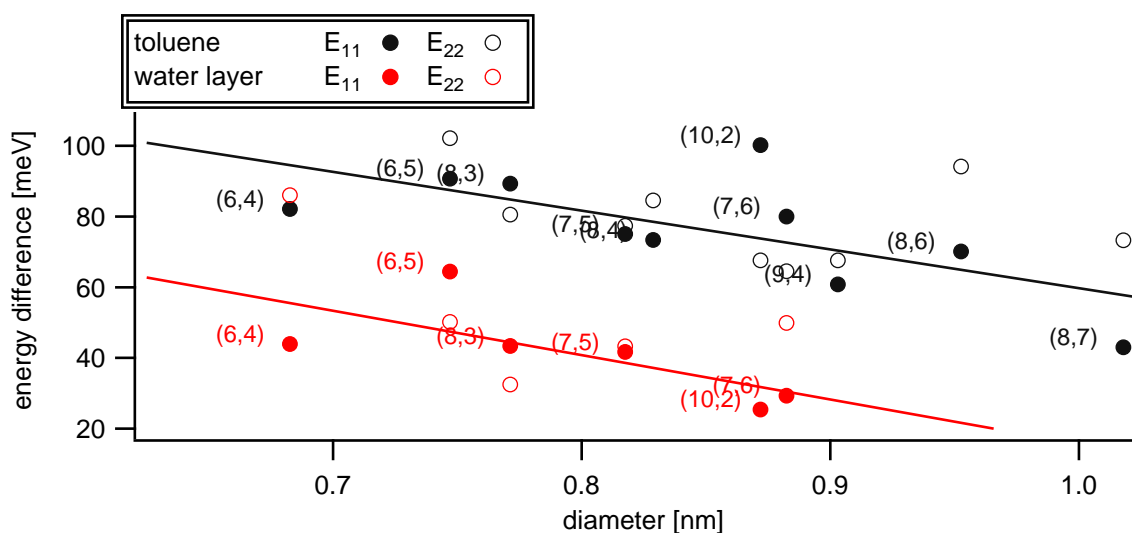
Fig. 18: Both states that experienced different dielectric surroundings in air shift to the same final energy in toluene.

The total energy shift for initially adsorbed molecules is lower than the energy shift for nanotubes with a clean surface and depends linearly on the diameter.
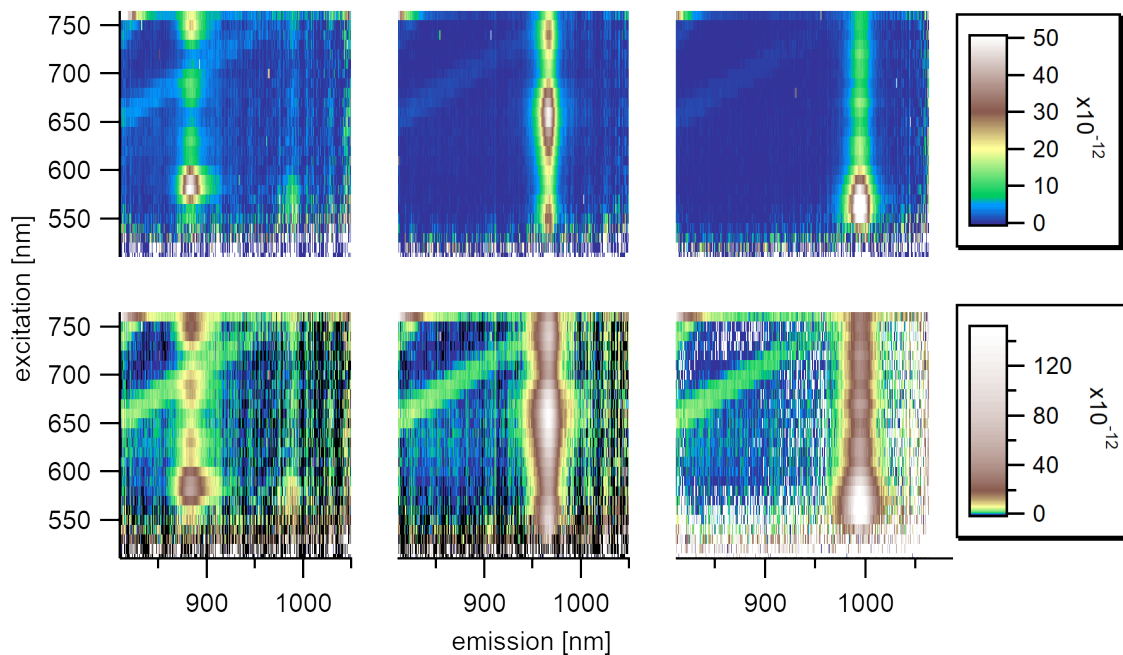
Fig. 19: Single PLE maps showing resonant energy transfer from the solvent phonon in toluene to the exciton in the first subband for the (6,4), (8,3), and (6,5) types.

Red-Shifted Energy

The transfer to toluene causes a peak shift of around 60-90meV to the red. The peak shift is lower by 50meV for chiralities that were initially adsorbed with a water layer. The emission of chiralities with an energy that was initially shifted to the red from an adsorbed water layer meets at the same excitonic energies than the nanotubes with an initially clean surface. This suggests that the water layer is completely desorbed in solvents and exchanged by a toluene layer. Although desorption of the water layer in toluene is entropically hindered, the gain in enthalpy from increased London interaction with toluene overcomes the desorption barrier of adsorbed water.

The excitonic states are formed at the π-orbitals of the carbon lattice. From a first estimate, the influence of the dielectric surrounding should, therefore, be equal. The measurement, however, shows a clear dependence on the diameter. Smaller diameters show more substantial shifts in their E_{22} and E_{11} energies. The E_{22} absorption is widely broadened and has a higher error value. Nevertheless, the energy shift coerces with the corresponding E_{11} emission levels. Since excitonic states on nanotubes with smaller diameters are likely to extend further into the dielectric medium, the excitonic emission is expected to have such a dependence on the diameter of the observed chiralities.

Conclusion

The measured dataset gives insight into pristine and unbundled carbon nanotubes without adsorbed surfactants other than the solvent itself. The measurement bridges a gap between suspended nanotubes and various unbundling processes in solution. It is especially crucial as dielectric effects on the outer surface originating from solvent and the process of bundling are usually impossible to differentiate as they are superimposed. The acquired data may serve as a reference for studying various other effects that influence the line width, intensity, or energy of excitons in carbon nanotubes.

Table 2: freely suspended SWNT in toluene

label	chirality	excitation [nm]	emission [nm]	error (exc) [nm]	error (emi) [nm]
a	(6,4)	584.5	885	49.5	16.5
b	(8,3)	670.5	975	5	8.5
c	(6,5)	563.5	995	27.5	40
d	(7,5)	652	1035	3	7.5
e	(10,2)	750.5	1075.5		
f	(8,4)	592.5	1123	9	12
g	(7,6)	653.5	1143	10.5	18
i	(8,6)	736.5	1190	12.5	7.5
k	(8,7)	746	1251	36.5	5
m	(9,4)	744	1126.5	11.5	8

3.2.2 Adsorption of Acetonitrile

Acetonitrile is a polar solvent with a dipole moment of nearly 4D [220]. It shows high solubility for charged molecules like tetrabutylammonium hexafluorophosphate and is, therefore, an ideal electrolyte for the exchange of charges. Molecular dynamics simulations are showing good solubility and fast diffusion characteristics for tetraethylammonium and tetrafluoroborate ions [221]. These are promising properties for various applications like supercapacitors or organic solar cells. As nanotubes can be electrically contacted [222], they can be used as electrodes where they exhibit a high active surface for high capacitance and faster ion diffusion velocities than typical activated carbon [223].

In order to test the behavior of nanotubes in acetonitrile, the vibration of the solvent can be used as a probe for solvent reorganization in the surrounding of the nanotubes. In a solvent like toluene or acetonitrile, the Raman active CH stretching mode (generated by the laser excitation) falls into resonance with the absorption of the nanotubes' E_{11} level
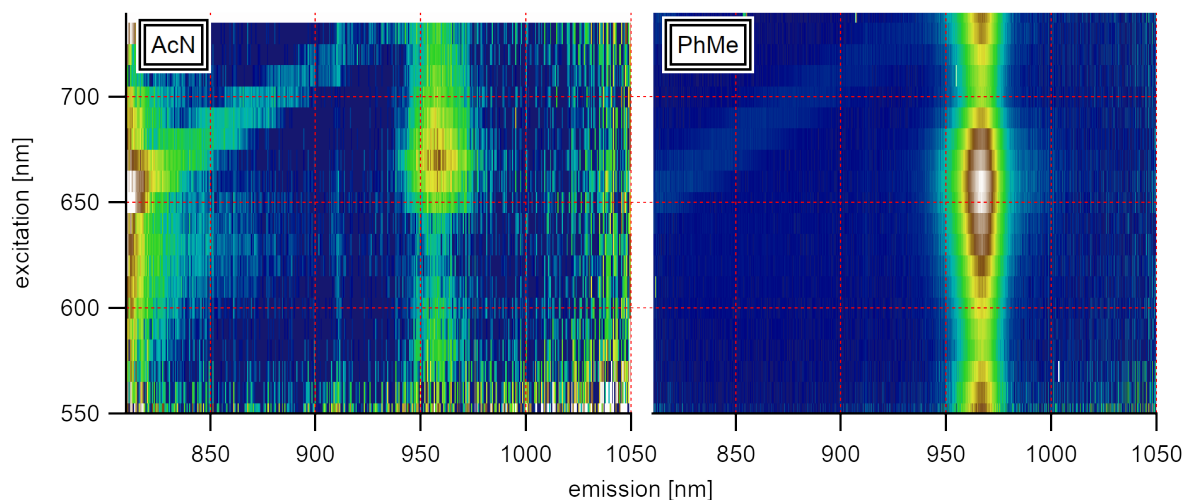
Fig. 20: A comparison of the influence of the solvent phonon on the (8,3) type in acetonitrile and toluene shows the resonance of the Raman-active signal (diagonal) at 750nm excitation.

for chiralities like the (6,4), (8,3), and (6,5) type. This resonance is nearly the same as observed in toluene. However, the different dielectric environment causes slightly different excitation/emission properties of the excitonic states.

Strong Emission

If the sample is kept at room temperature for 24h, an emission emerges at locations on the sample where carbon nanotubes are located. The intensity of this emission is comparable to the emission of air-suspended carbon nanotubes and can be even brighter. However, it does not show similar properties of excitons in single-wall carbon nanotubes. Even though the sample preparation technique synthesizes at least 80% of the chiralities with a diameter larger than 0.8nm, the emission was only observed for the (6,4), (8,3), and (6,5) types which are a minority species in this sample. This suggests that this phenomenon has a dependence on the diameter of the nanotubes.

The origin of the new signal is located at the spatial location of nanotubes. However, it is not originating directly from a typical excitonic state within the nanotubes as it is broad, shifted blue, and stays nearly the same within all observed chiralities. One similarity within the observed nanotubes is their absorption in air, which can be extracted from a vertical cut through the measured PLE maps. This profile strongly depends on the laser polarization.
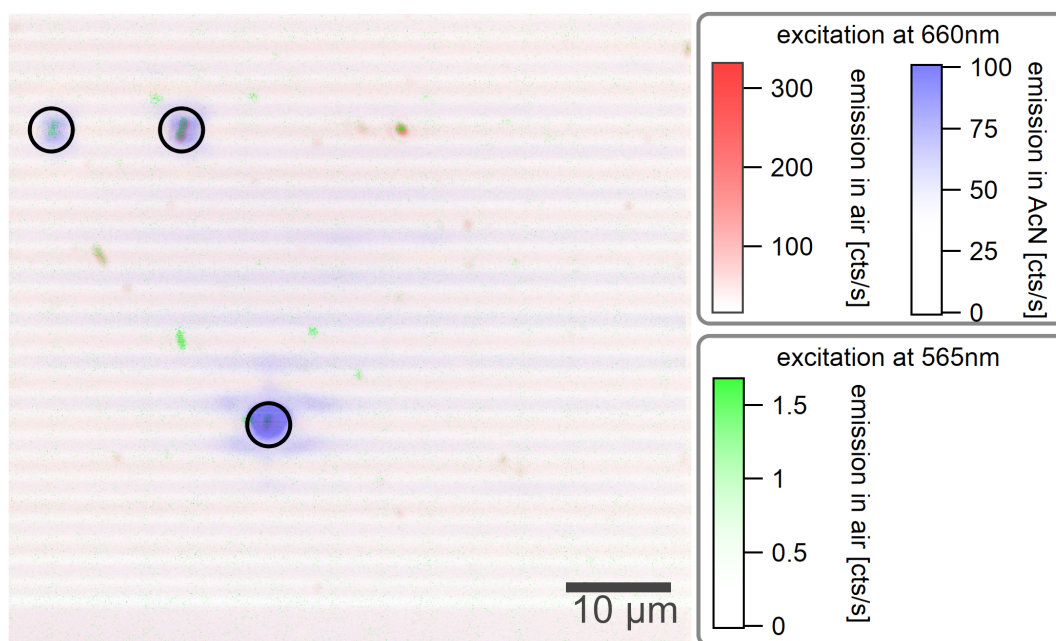
Fig. 21: After one day in acetonitrile, enhanced emission at the locations of carbon nanotubes is visible. The emission in toluene is shown in blue while the emission in air is shown as an overlay in red and green.

Nanotube Vibrations

In the following, I will discuss the intrinsic properties of the investigated samples in air in more detail to get a better understanding of the polarisation dependence of the nanotube emission and the relation to the absorption spectrum as well as on vibrational couplings.

A cross-polarisation analysis of PLE spectra has previously found two resonances for transversal polarized excitation that are blue-shifted [224] to the central E_{22} absorption. They are usually assigned to the E_{12} and E_{21} transitions. However, if depolarisation effect are considered the state is also sometimes assigned to an excited exciton state at higher coulomb energies [225].

The absorption resonances in the recorded spectra are found to be polarized parallel to the E_{22} resonance. This suggests that the resonances do not originate from E_{12} transition but rather from a K-phonon assisted scattering process involving dark excitons [226].
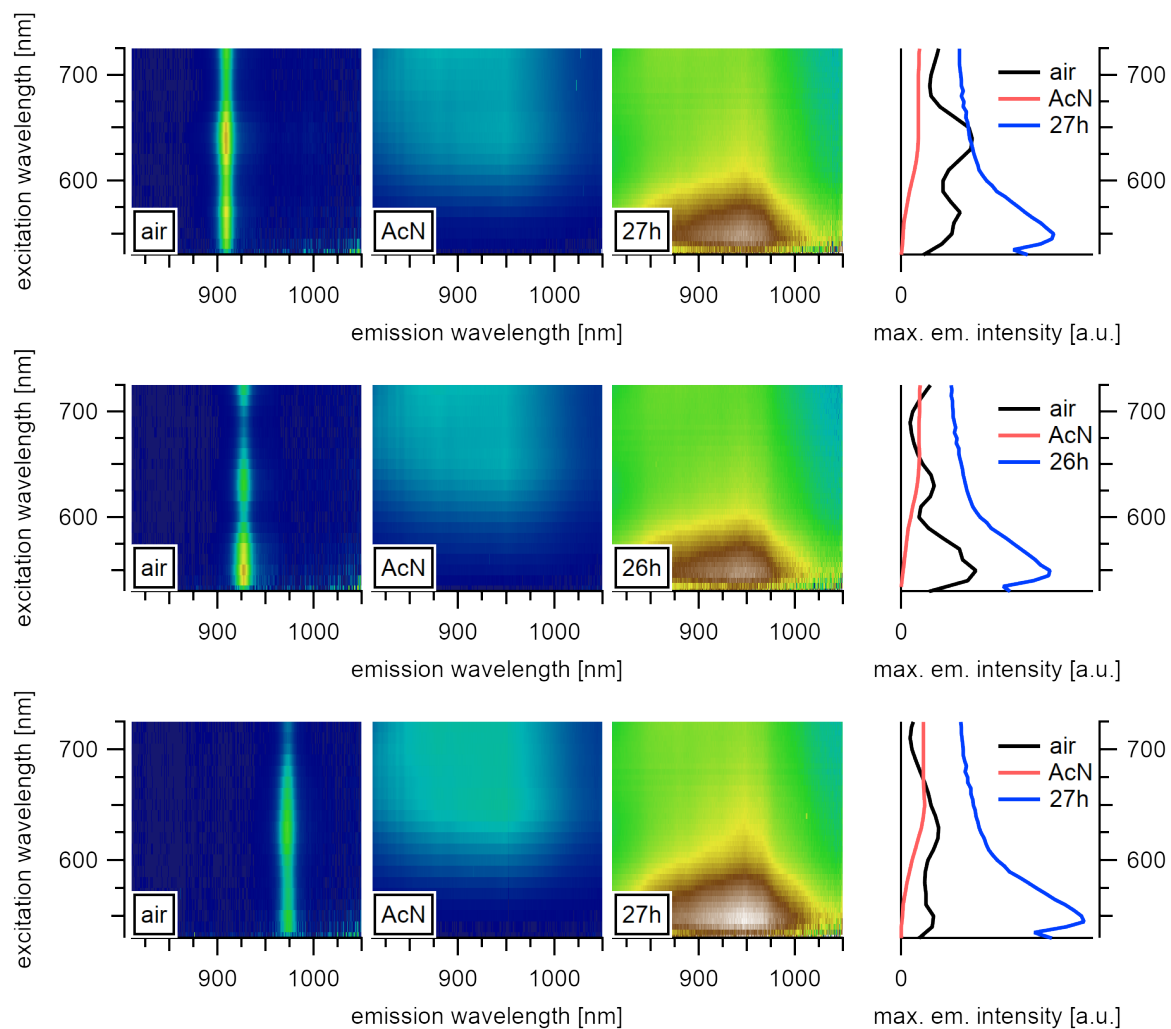
Fig. 22: A strong emission emerges for the (6,4), (8,3), and (6,5) types. The emission after one day of observation is chirality independent.
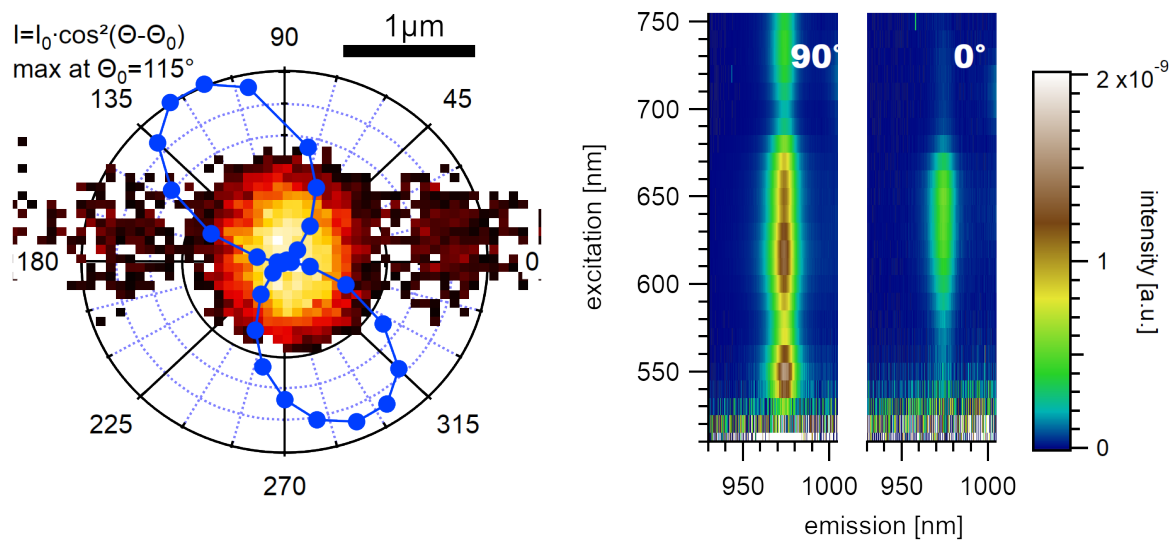
Fig. 23: A (7,5) type in air with a clean surface shows a distinct dependence of its emission on the excitation polarization angle. The camera image at the recorded location is shown as an overlay image (left). In a PLE map, the modes above and below the second excitonic transition vanish at an excitation perpendicular to the nanotube axis.
The measured polarization intensity in the left graph is normalized to the power of the elliptically polarized laser, measured after the polarizer. The measured excitation intensity is altered by the formula depicted in the top left, which gives the best agreement if the nanotube is assumed to be suspended over the trench at an angle of 115° to the propagation of the trenches. The angle is found mathematically through optimization by assuming that a nanotube exhibits maximum emission intensity if it is excited along its longitudinal axis.

band	wavelength	energy	difference
E_{22}+KPS	550nm	2.25(2)eV	230(40)meV
E_{22}	615nm	2.02(2)eV	
E_{22}-KPS	650nm	1.91(2)eV	110(40)meV
E_{22}-2D	735nm	1.67(2)eV	350(40)meV
E_{11}	974nm	1.273(1)eV	

The lower energy phonon depends on the dielectric electric environment [227], this explains the lower energy of 110meV for ε=2 (vacuum) compared to the typically seen 140meV [216] at ε=4 for the lower and 200meV for the higher phonon scattering process. Similar to Torrens et al., the sum of the splitting matches with the 2D mode at 326meV [216] as the transversal KPS mode is also responsible for the 2D mode.

The energy of the K-phonon was calculated to be at 170meV above the bright Γ-momentum excitonic state [227]. This allows calculating the binding energy of the dark exciton for a suspended (7,5) type to 60meV which is almost double the value compared to usual reports in solution.[200][228][216] but in good agreement to other reports in vacuum [184][229]. The fraction of the spectral weight that is transferred to the phonon sideband was estimated to increase significantly for smaller diameters like the 0.8nm of the (7,5) type. [227] The measured spectral weight of these absorptions bands is higher than in typical samples, which underlines the high phonon binding energies but does, however, not fully explain its origin. The formation of sp^3-defect from nitrogen poisoned catalysts or from the remaining ethanol after synthesis during the rapid cooldown similar to hydrogen defects in the reaction chamber is possible but could not be affirmed. To the best of my knowledge, these phonon sideband absorptions near the E_{22} level have never been reported. Neglecting its unclear origin, the excurse into the phonon sidebands of the investigated nanotubes showed that the samples have excellent coupling to the optically active K-phonon vibrations. In the following, I will show that such coupling might be necessary to get increased resonance transfer from solvent phonons to the nanotube.

Solvent Vibrations

In the previous analysis, I have justified that the investigated nanotubes show phononic vibrations with high binding strength in their optical absorption. Other than in air, however, in acetonitrile, the maximum of the spectral emission intensity changes only by 5-10% if the excitation polarisation is rotated by 90°. This is different from the emission of typical carbon nanotubes and suggests that the emission in acetonitrile happens via an initial excitation into a depolarizing state. As the emission signal does not originate directly from excitons on the nanotubes, the solvent is suspected to be the origin of this

depolarization effect. The vibrations are further analyzed to understand the possible effects of the solvent.
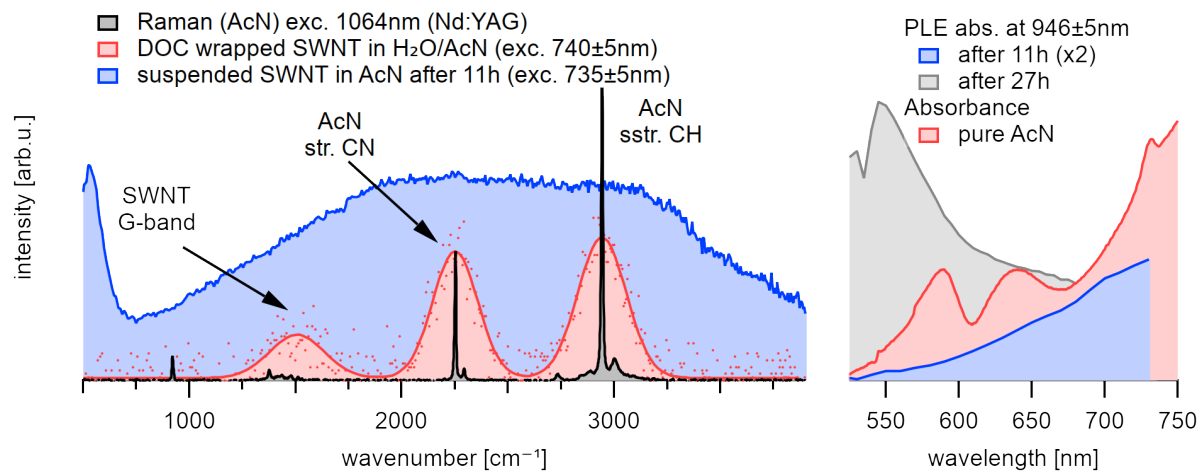
Fig. 24: The emission at an excitation wavelength of 735nm shows good agreement with the three phonon modes that are present in this system.
A comparison with the optical absorbance of the solvent shows that the PLE absorption is enhanced at similar wavelengths where the solvent absorption shows resonances.

Acetonitrile is a linear, polar molecule of $C_{3,v}$ symmetry. The stretching of the CH bond at $2942cm^{-1}$ and the CN bond at $2250cm^{-1}$ are both strong,[230][231] optically active infrared and Raman vibrations. Acetonitrile shows a good absorption to the 5th overtone at 625nm and moderate absorption to the 6th overtones of the CH stretching vibration at 540nm.[232] The 4th overtone of the CH stretching and the 5th overtone of the CN stretching vibration are located at the rising absorption at around 735nm.

After placing the sample in acetonitrile, the excitonic emission from nanotubes can be recorded similar to the emission in toluene. The solvent phonon from excitation to the virtual laser niveau is visible as two parallel diagonal lines in the PLE maps that are broadened from the intrinsically broad laser excitation profile of our white light source. A comparison with the emission in pure acetonitrile using 1064nm excitation of an Nd:YAG Laser and calculations using B3LYP confirms the vibrational origin.

After 11h, however, the observed emission intensifies towards the 4th and 5th CH stretching overtone resonances at 625(25)nm and 735(10)nm, and the PLE absorption becomes comparable to the absorbance of pure acetonitrile. The spectral weight of the emission follows the location of the two strongest Raman active stretching vibrations of the solvent molecules at 946nm and 888nm at 735nm resonance. Even though the excitation with our white light source broadens the emission signal, it also typically gives clearly differentiable peaks. In contrast, the observed solvent phonons around the nanotube are broadened compared to the liquid around. Moreover, the intensity is significantly higher at the location of the nanotubes than in the solvent surrounding.

After 26h, the spectral intensity even exceeds the emission properties of the nanotubes in air. The absorption resonance intensifies at the location of the 6th overtone of the CH stretching at 545(5)nm while the emission maximum at 946(2)nm intensifies for all observed chiralities.
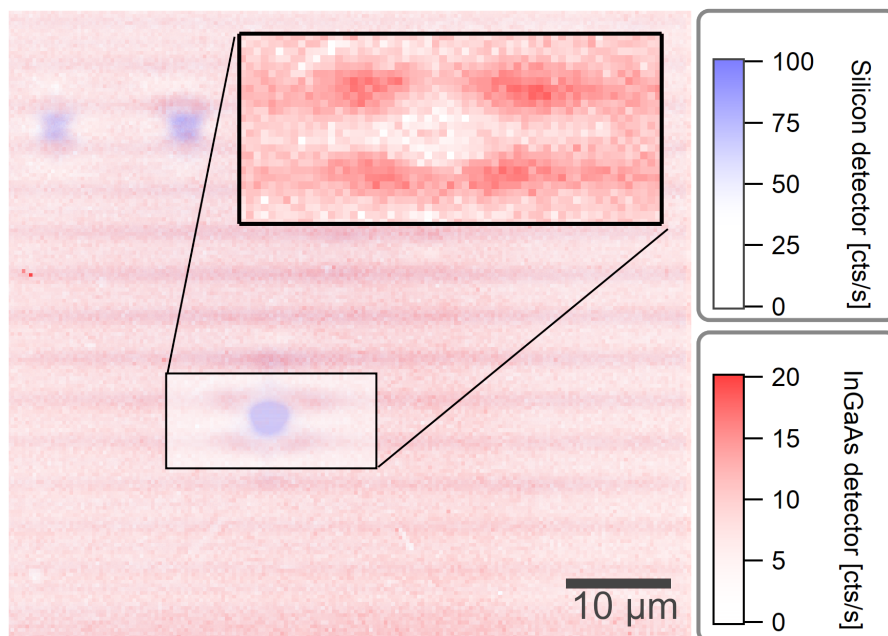
Fig. 25: The emission (0.85μm - 0.9μm) is centered at the location of the nanotubes, while the SWIR emission ($>$0.9μm) originates from the spacial surrounding of the nanotubes.

Cyanide Nanotubes

Due to its cylindrical shape, carbon nanotubes have two different surfaces: An inner and an outer surface. The outer surface is highly accessible for fast molecular adsorption and desorption processes. In contrast, the inner surface is only reachable through the two ends of the tube, which limits the speed of molecular diffusion.

A (6,6) chirality has only an accessible inner diameter of 0.48nm for solvent molecules to enter [233]. Therefore, only small molecules like water [234][235][236][237][100], acetonitrile [233], or fullerenes [238] of a suitable diameter are able to enter the inside of typical carbon nanotubes. This encapsulation technique is known as nanofluidics and useful i.e., for confining the dipole moment of dyes in a linear chain inside the nanotubes which enhances the dyes' absorption and emission characteristics.[239]

In solution, acetonitrile forms cyclic dimers with antiparallel orientations while collinear dimer formation is usually considered to be insignificantly low.[231] Collinear dimers, however, show substantial Mulliken charge differences between the two carbon atoms in

both, the donor (head) and the acceptor (tail) molecule [240] of the dimer configuration. The charge is reduced on the methylic donor carbon atom and increased at the nitrile carbon, which increases the net charge distribution of the dimer configuration by around 0.5e.

There have been predictions for the symmetric arrangement of acetonitrile inside and around carbon nanotubes: As acetonitrile is a linear molecule, inside of nanotubes with smaller diameters acetonitrile arranges in a uniform lateral head-to-tail pattern [10] whereas concentric structures form as the diameter increases [233]. Such a uniform arrangement can intensify the initial dipole moment by strong resonant coupling of the longitudinal stretching vibrations.

The evolution of this calculated uniform arrangement is expected to be limited by the diffusion speed through the ends of the nanotubes, which explains the slow time evolution of the observed luminescence. The infrared active higher modes of the solvent vibration are excited, depolarize the signal, and carbon nanotubes of the observed chiralities can resonantly couple to these vibrations. Strong coupling of the K-phonon sidebands with the bright exciton assists in an efficient excitation energy down-conversion to the stretching phonon resonances. From these modes, the vibration relaxes radiatively. The high structural confinement of the molecules in such a vibration causes a damped oscillation, which explains the observed broad line widths. Spatially resolved camera images of this emission suggest that there is also significant solvent interaction on the outer surface of the carbon nanotubes. Supercapacitors rely on the adsorption of molecules on an electrode surface and lossless conduction contact from this surface to an electrical circuit [221]. Due to their high dispersion interaction and binder-free adherent contact to the electric potential, carbon nanotubes are highly favored for this application [223]. Due to its assumed polarity, the discovered system should be suitable for efficient ion adsorption. It is notable, however, that polarized carbon nanotubes generally suffer from bundling in organic solvents [210], which is an expected major culprit. Indeed, so far, it was not possible to isolate these nanotubes in solution using established recipes. An adapted recipe should start by solvating the centrifugation residue after sonication and analyzing the outcome via density gradient centrifugation.

Conclusion

The low quantum efficiency of carbon nanotubes is their most prominent culprit and hinders their usage in photonic devices. The investigated system shows efficient energy down-conversion from 540nm to 950nm, which by far exceeds typical values of even air-suspended nanotubes. Nanofluidics is an emerging field that has shown to give astonishing improvements to the emission properties of individual nanotubes. Couplings of the E_{22}-exciton can explain the down-conversion in acetonitrile to the solvent phonon stretching

vibrations. Its significant enhancement over longer observation time scales allows suggest-ing solvent diffusion through the ends of the nanotubes. Such down-conversion could be useful for experiments in biological tissues [15] where blood and water absorption opens a window in the SWIR between 700-1300nm [11] which enhances the contrast ratio for nanotube-based fluorescence sensors. It should also be possible to harvest the electrons of the transitional excitonic states in the photoactive layer of bulk heterojunctions.

3.3 Adsorption of Solid

The strong adsorption forces on carbon nanotubes can also be used for binding other solid molecules. Similar to active carbon, the adsorptive properties can be used for the treatment of water contamination [241]. The most prominent usage, however, is the non-covalently functionalization of the surface, which enhances the solubility of individualized carbon nanotubes while mostly preserving their excitonic emission properties at room temperature.

3.3.1 Non-Covalent Functionalisation
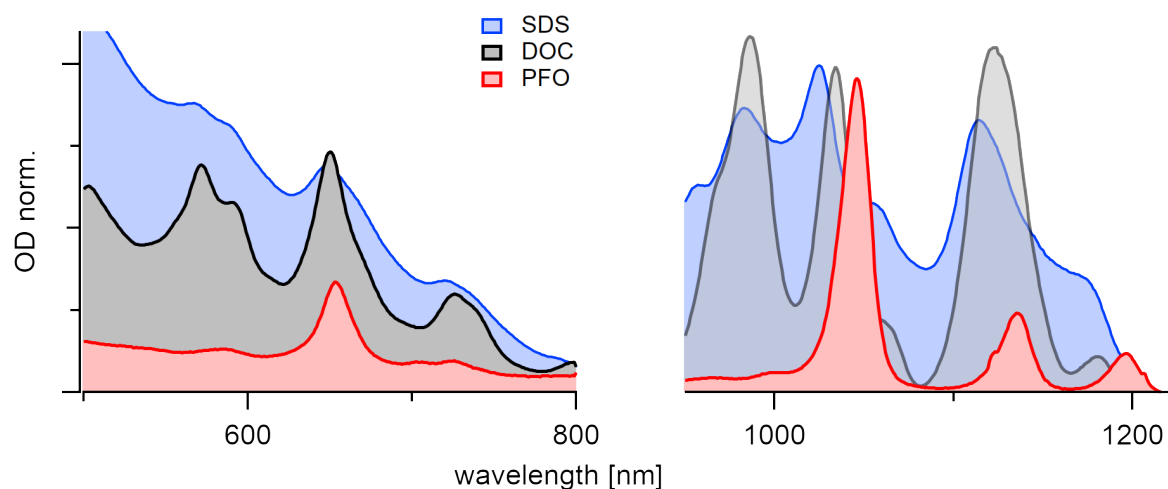
Fig. 26: PFO selectively binds to the (7,5) type while DOC almost equally suspends every chi-rality. The rise in absorption background comes from the dispersion of graphene flakes and metallic nanotubes.

The first successful individualization of carbon nanotubes was achieved using sodium dodecyl sulfate (SDS) [242] in D_2O which encapsulates the nanotubes in micelles. Other amphiphilic molecules with water solubility like sodium dodecylbenzene sulfonate (SDBS) [243] followed. Both of the aforementioned sodium salts are in constant equi-librium with the surroundings leading to continuous ad- and desorption of the sur-factants. Strong binding forces are crucial for creating kinetically stable suspensions

[244] that preserves their emission properties on long time scales. Nowadays, thermodynamically more stable surfactants are employed to the advantage of better emission properties. In H$_2$O dispersions, cholic acid derivatives [101] or single-stranded DNA (ssDNA) are used. Furthermore, in organic solvents thiophene based polymers [245] like poly(3-hexylthiophene) (P3HT), fluorene based polymers [6][246][247] like poly(9,9-dioctylfluorenyl-2,7-diyl) (PFO), thiophene-thiazol copolymers [248] like poly[2,6-(4,4-bis-(2- dodecyl)-4H-cyclopenta[2,1-b;3,4b']dithiophene)-alt-4,7(2,1,3- benzothiadiazole)] (P12CPDTBT), and carbazole polymers [249] are used in combination with various other block co-polymers.

If the emission properties from nanotubes wrapped with different surfactants are compared in the same solvent, it is found that the type of surfactant plays a significant role for the excitonic energy as it also influences the dielectric environment. The transfer from DOC to SDBS, for example, causes a shift of the excitonic emission by 8nm [138], and SDS shows a strong blue-shift [243]. A time-dependent measurement of the photoluminescence during dilution shows that the desorption barrier of a polymer from the carbon nanotube surface is by far higher in organic solvents than micellular systems like ssDNA in water.[250] Such observations emphasize the higher stability of suspensions generated with the use of polymers compared to micellular systems. Upon these polymers, polyfluorenes are most frequently applied for the isolation and chirality-specific dispersion of individualized SWNTs in organic solvents [6], which is why in the following I want to investigate this system in more detail.

3.3.2 Adsorption of Polymer

The interaction of polymers with SWNT plays a key role in providing the desired selectivity. The mechanism for the adsorption of polymers, however, is under ongoing discussion.[7] In this section, the different binding processes are summarized to understand the interaction of polymers on nanotube surfaces and introduce the experiment design that is used for this study to help in clarifying the ongoing discussion.

P3HT is known to bind more strongly to SWNTs than PFO but has less selectivity which is why a thiophene based polymer can exchange the fluorene polymer if both are available in the solution.[251] Such behavior is typically explained by the rigidity of the backbone of PFO which controls the covalent binding strength of the π-stacking.[252] A flexible backbone gives stronger binding enthalpies and thus more stable suspensions. Also, for their selectivity, the rigidity of the polymer backbone plays a significant role. PFO has a more rigid backbone giving looser π-stacking, but this very rigidity leads to selective interaction with the (7,5) type while its more flexible block copolymer with bipyridine (PFO-byp) binds better to the (6,5) type but is less selective. It can be

shown that the roll-up angle of an SWNT chirality influences the binding strength [247] of different co-polymers and thus alters the selectivity to certain chiralities. This roll-up angle dependence on the dispersion efficiency has been shown for various polymer combinations [249] which underlines the importance of both, π-stacking, and wrapping efficiency effects.
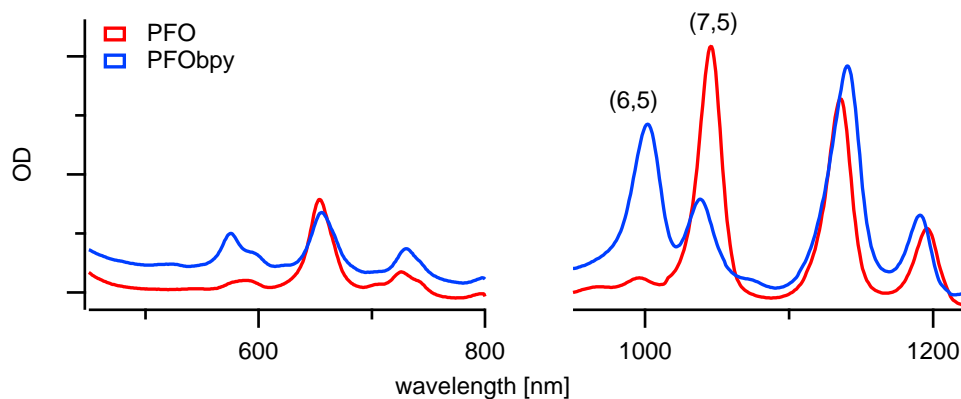
Fig. 27: The rigidity and structure of the polymer backbone cause selectivity differences between PFO-bpy and PFO: PFO-bpy preferentially selects the (6,5) type, PFO, on the other hand, is suitable for selecting the (7,5) type.

Metallic nanotubes are responsible for the exponentially increasing strong absorption background [253] that is visible for SDS and DOC dispersed samples between 900-450nm. Polymers generally show little to no such background absorption. The high polarizability of metallic nanotubes is thought to lead to the effective removal of bundles [210] in organic solvents during centrifugation. Therefore, for measuring the selectivity of polymers, the solvent effects usually have to be differentiated from the pristine polymer effects that depend on the binding energies during π-stacking.[7] Brunecker et al. [250] also showed that for polymers, the de-sorption is neglectable. Consequently, ad-sorption measurements have to be performed on a clean surface because otherwise, the two competing processes are indistinguishable.

The dispersion efficiency for all polymers also strongly depends on the length and functionalization of the side chains.[245][254][244] SWNT that were processed with polymers that have longer side chains also show stronger absorption after sonication.[206] As the side chain length plays little to no role for the intrinsic optical absorption of the polymer [254], charge transfer can be excluded, and it is expected that the side chain length only increases solubility. The finding is affirmed by TDDFT calculations [255] and allows us to suggest that polymers adsorb with the aromatic backbone to the SWNT surface. One side-chain wrapping the nanotube surface and one side chain stands out to the solvent. Such solubility advantage effect of the dispersive medium is also found at high coverages of ssDNA [250] where the majority of the oligomers stands out to the solvent and is not directly attached to the nanotube surface. In polymer suspensions, two decay rates of

the polymer fluorescence are observed [256], which can be explained with the difference of fluorescence between partly adsorbed polymer where some polymer trains are standing out to the solvent.

As outlined here, understanding the mechanism of non-covalent adsorptions on the nanotube surface is utterly important for the study of their emission properties. Single-molecule investigations were carried out using suspended carbon nanotubes to focus on this mechanism in more detail.

Single Molecules

A stable system that has gained considerable interest is the dispersion of carbon nanotubes with poly[(9,9-dioctylfluorenyl-2,7-diyl)-alt-co-(6,6'-{2,2'-bipyridine})] (PFO-bpy) in toluene.[247]. Investigations on the adsorption of to the (6,5) type show that the polymer wraps around the cylindrical nanotube at an angle of 14(2)° to the longitudinal axis.[257] Although the dispersion efficiency is low, these systems show more narrow line widths [218] than DOC wrapped nanotubes, and better quantum efficiencies than most other polymers.[213]

As outlined before, various effects during this adsorption process have to be considered, which is the reason for divergent interpretations and are mostly hard to distinguish. Most experiments in solution suffer from these overlapping phenomena. In this experiment, toluene-suspended SWNT are used as a defined starting point for studying polymer adsorption. The nanotubes are fixated on the substrate which hinders the nanotubes from precipitation and diffusion while maintaining the solvent environment during the investigation. It also allows to separate solvent and bundling effects from the usually concomitant polymer stacking and wrapping effects to investigate the undisturbed adsorption mechanism. Due to the selectivity for PFO-Bpy on smaller-diameter nanotubes, the experiment was performed with cooled silicon detectors to detect the emission between 830-1050nm. This allows investigating predominantly nanotubes of diameters between 0.7-0.8nm with a good quantum efficiency of the detectors to lower the integration times to 15-60s in solution with typical observation times of 5h. The high single spectrum acquisition time is owed to the generally lowered nanotube emission in solvents. For all SWNT with detectable diameters, PFO-Bpy is known to show selective dispersion. This allows investigating the rather low amount of nanotubes that survived the transfer to toluene while preserving their excellent emission properties.

The sample is placed into a quartz cuvette and wetted with an excess of 6mℓ toluene. After staying for at least 24h in the closed cuvette, 50-100$\mu\ell$ of a 1.5nM polymer solution with an average polymer weight of 33kDa (60 monomers trains per molecule) is introduced. The sample is located at the bottom of the cuvette, and the wafer hinders the polymer
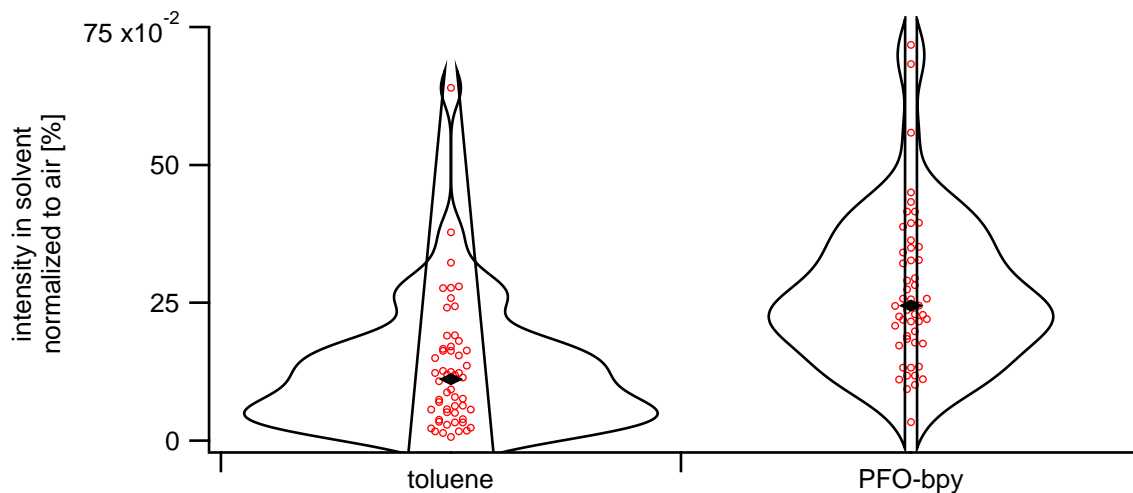
Fig. 28: The fluorescence of toluene-suspended carbon brightens after the addition of PFO-bpy. Some nanotubes even reach 75% of their initial emission in air.

from free diffusion to the area of observation. Nevertheless, the polymer is expected to reach the sample within a few minutes. After 24h of exposure to PFO-bpy, the emission intensity is around twice as high as in pristine toluene. This is most probably explained by the polymer leading to the desorption of toluene and preventing further adsorptions.
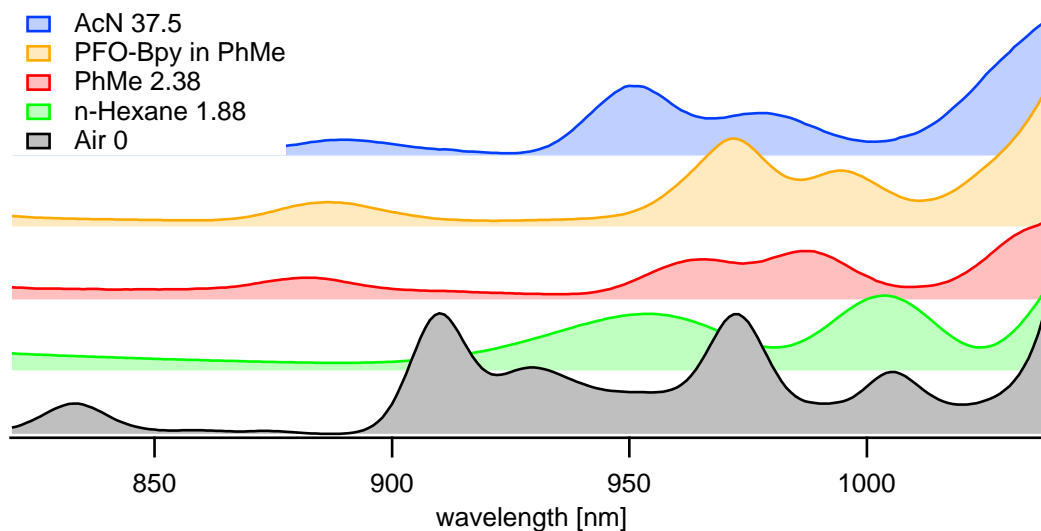
Fig. 29: The excitonic emission in toluene with adsorbed PFO-Bpy is shifted to the red compared to the emission in pure toluene. The graph shows the unweighted spectral autocorrelation of individual measurements.

The polymer wrapping increases the dielectric environment. This increase leads to a red-shift of the excitonic emission signal. Energy shift and emission intensity are used as a probe for polymer adsorption during the time-dependent observation on single nanotubes. For this measurement, the nanotubes are first observed for 2h until emission stability at low excitation energies (5-30μW/3μm^2). The adsorption of the polymer is observed in an

excited thermodynamic equilibrium caused by the laser heat. This elevated state allows observing the ad- and desorption process on a single molecule basis.
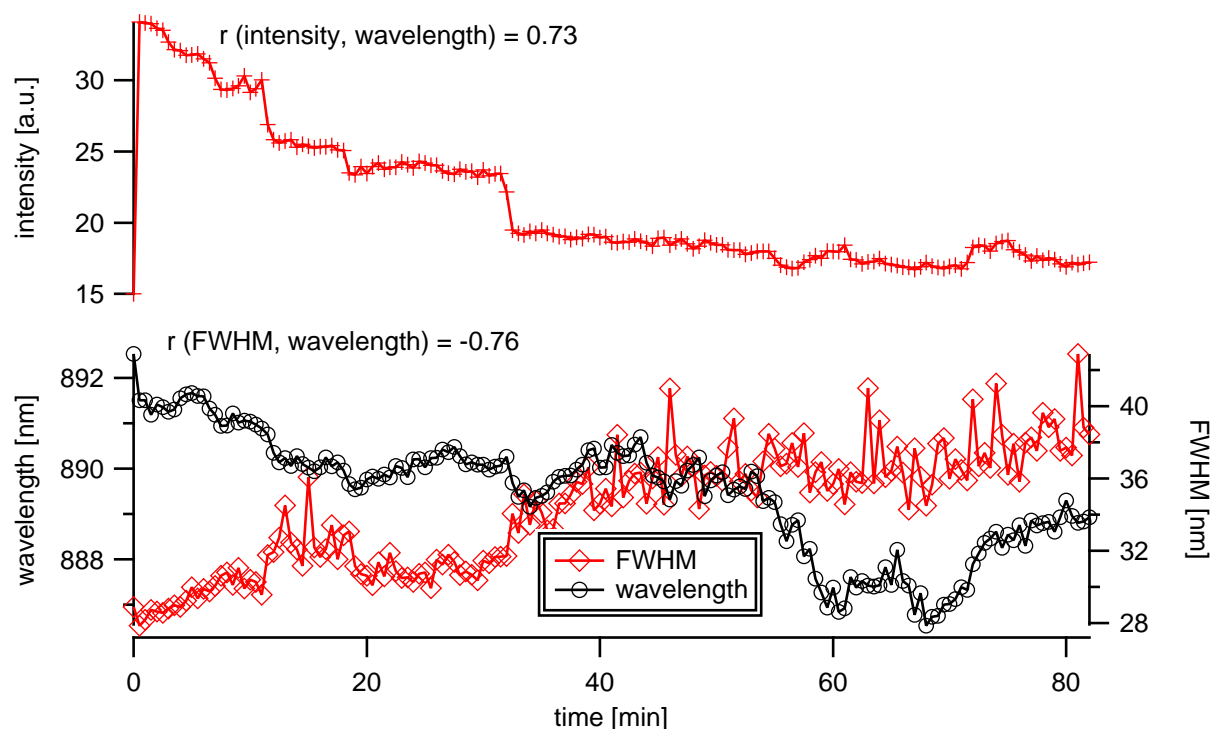
Fig. 30: Irreversible stepwise intensity decrease during the adsorption of PFO-bpy to a nanotube of the (6,4) type.

When observed over long time-scales, the emission intensity of the carbon nanotubes in solvents depleaches step-wise. Such depletion is probably caused by the generation of defects through reaction with oxygen which is known to generate irreversible steps.[160]

The time evolution of the energy is usually analyzed with the Allan deviation [258][259] to minimize the white noise in the emission spectra.[203] For nanotubes in toluene at room temperature with rather high integration times of 30s per spectrum, the energy fluctuations are minimal and are not expected to achieve a higher resolution with different statistics.

There are also reversible steps visible that are caused by diffusion quenching within a mean segment size of $\Lambda = 20/180 \cdot 2\mu\text{m} = 220(20)\text{nm}$. Such segment sizes are more than double the size as expected from the mean polymer train lengths. Unfortunately, high exciton diffusion lengths are expected for this system as proven with a simulation during image analysis. With such high diffusion lengths, the observation of polymer adsorption is limited. Nevertheless, the energy clearly shows a distinct shift to the red after the intensity fluctuations stop and the observed steps are partly reversibile. This allows assuming that we indeed observed polymer adsorption.

The vague insights do not allow to make assumptions on the exact binding mechanism.
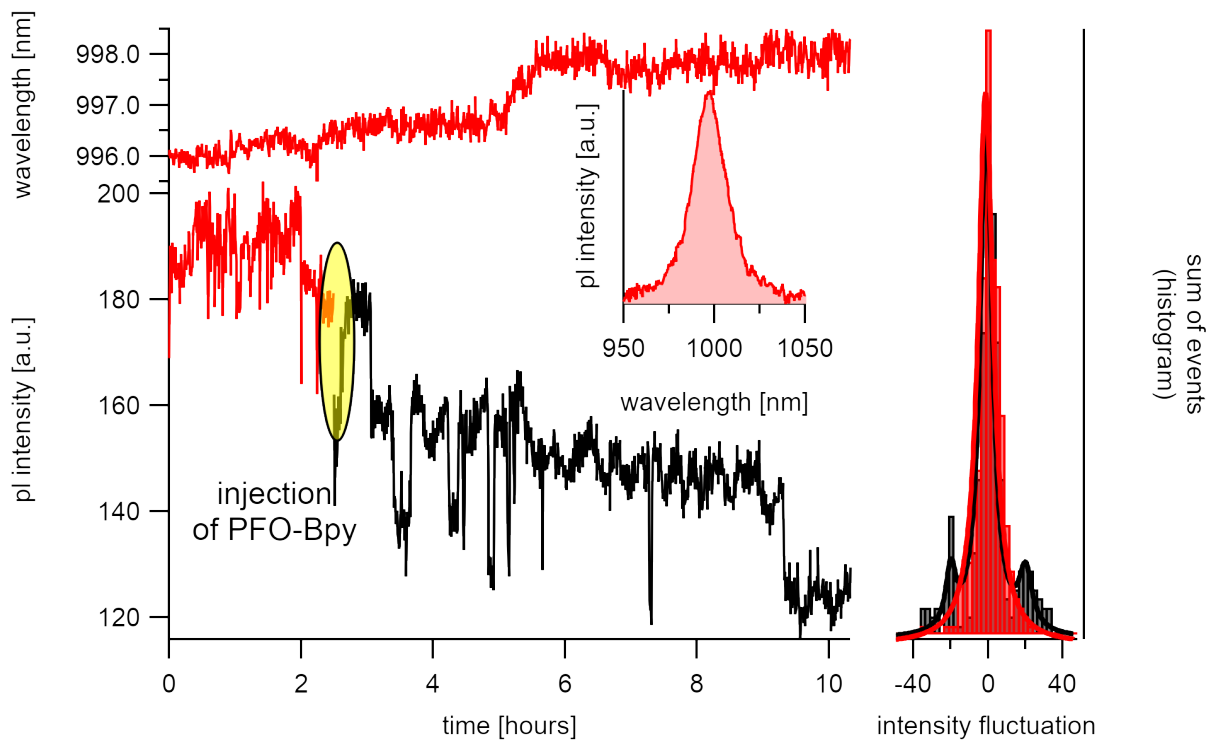
Fig. 31: The figure shows the time-dependent adsorption of PFO-bpy on the (6,5) type. Adsorption is identified by an increase in the emission intensity and a red-shift of the emission wavelength.
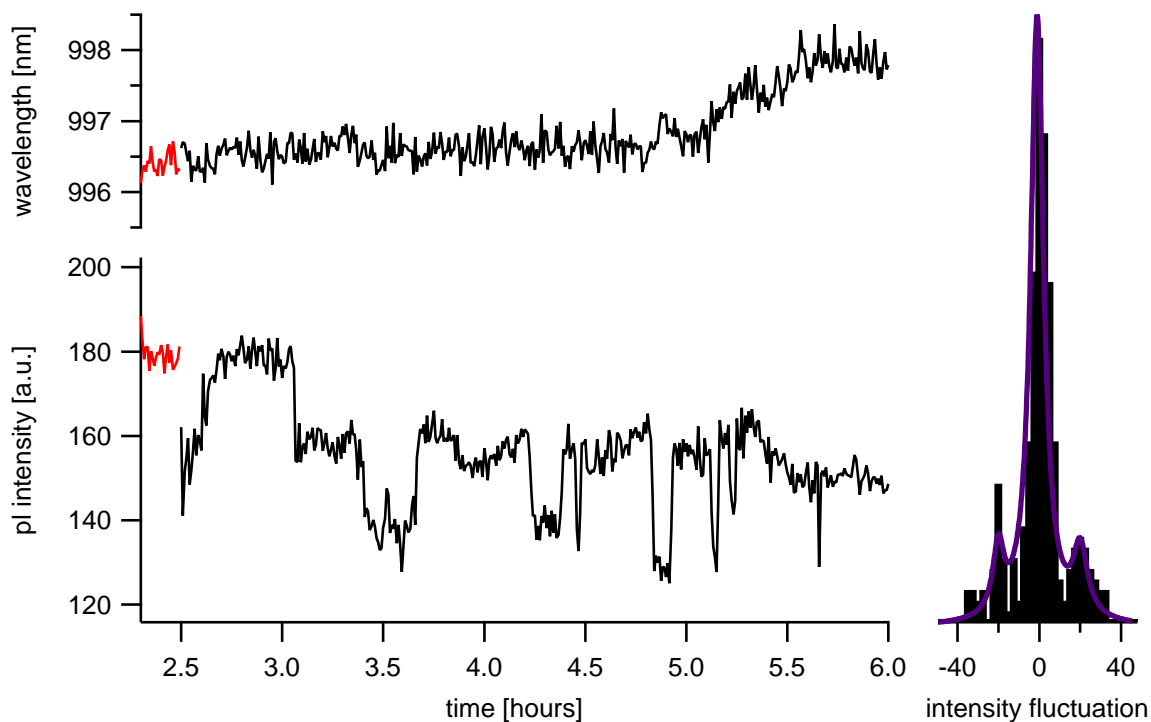
Fig. 32: The intensity decreases stepwise. The irreversible increase in intensity is followed by a shift of the emission wavelength to the red.

A possible explaination of the observed signal could be that the the octyl groups form an initial binding while the rearrangement of the π-stacking from the polymer backbone to the exact angle around the nanotube axis takes longer. As toluene gets displaced by octyl, the energy shifts to the red.

Conclusion

The adsorption of individual polymer molecules on suspended nanotubes is a tedious and complicated measurement. Nevertheless, we presented initial results of the individual adsorption of Poly(9,9-di-n-octylfluorenyl-2,7-diyl)bipyridine (PFO-bpy) on the surface of suspended SWNTs in toluene using single molecule fluorescence microscopy and spectroscopy with single molecule observations over more than 6h. Changes in the intensity and central wavelength of the excitonic emission was used as a probe for surface effects.

It could be shown that the polymer only minimally changes the dielectric environment of the system and causes a red-shift compared to a system in toluene. The segment sizes of the involved polymer trains were below the resolvable limit defined by the exciton diffusion length. Such long polymer trains take rather long time for the irreversible adsorption. A cooperative binding mechanism is evident, although the exact mechanism leaves room for interpretation.

SUMMARY

Nanoelectronics is an essential technology for down-scaling beyond the limit of silicon-based electronics. Single-Wall Carbon Nanotubes (SWNT) are semiconducting components that exhibit a large variety of properties that make them usable for sensing, telecommunication, or computational tasks. Due to their high surface to volume ratio, carbon nanotubes are strongly affected by molecular adsorptions, and almost all properties depend on surface adsorption.

SWNT with smaller diameters (0.7-0.9nm) show a stronger sensitivity to surface effects. An optimized synthesis route was developed to produce these nanotubes directly. They were produced with a clean surface, high quality, and large lengths of 2μm. The results complement previous studies on larger diameters (0.9-1.4nm). They allow performing statistically significant assumptions for a perfect nanotube, which is selected from a subset of nanotubes with good emission intensity, and high mechanical durability.

The adsorption of molecules on the surface of carbon nanotubes influences the motion and binding strength of charge-separated states in this system. To gain insight into the adsorption processes on the surface with a minimum of concurrent overlapping effects, a microscopic setup, and a measurement technique were developed. The system was estimated to exhibit excellent properties like long exciton diffusion lengths (>350nm), and big exciton sizes (8.5(5)nm), which was substantiated by a simulation.

We studied the adsorption processes at the surface of Single-Wall Carbon Nanotubes for molecules in the gas phase, solvent molecules, and surfactant molecules. The experiments were all carried out on suspended individualized carbon nanotubes on a silicon wafer substrate.

The experiments in the gas-phase showed that the excitonic emission energy and intensity experiences a rapid blue shift during observation. This shift was associated with the spontaneous desorption of large clusters of gaseous molecules caused by laser heat up. The measurement of this desorption was essential for creating a reference to an initially clean surface and allows us to perform a comparison with previous measurements on this topic. Furthermore, the adsorption of hydrogen on the nanotube surface at high temperatures

was investigated. It was found that a new emission mode arises slightly red-shifted to the excitonic emission in these systems. The new signal is almost equally strong as the main excitonic peak and was associated with the brightening of dark excitons at sp^3-defects through a K-phonon assisted pathway. The finding is useful for the direct synthesis of spintronic devices as these systems are known to act as single-photon emitters.

The suspended nanotubes were further studied to estimate the effect of solvent adsorption on the excitonic states during nanotube dispersion for each nanotube individually. A significant quantum yield loss is observable for hexane and acetonitrile, while the emission intensity was found to be the strongest in toluene. The reference to a clean surface allowed us to estimate the exact influence of the dielectric environment of adsorbing solvents on the excitonic emission energy. Solvent adsorption was found to lead to an energy shift that is almost twice as high as suggested in previous studies. The amount of this energy shift, however, was comparably similar for all solvents, which suggests that the influence of the distinct dielectric constant in the outer environment less significantly influences the energy shift than previously thought.

An interesting phenomenon was found when using acetonitrile as a solvent, which leads to greatly enhanced emission properties. The emission is more than twice as high as in the same air-suspended nanotubes, which suggests a process that depends on the laser intensity. In this study, it was reasonably explained how an energy down-conversion is possible through the coupling of the excitonic states with solvent vibrations. The strength of this coupling, however, also suggests adsorptions to the inside of the tubular nanotube structure leading to a coupled vibration of linear acetonitrile molecules that are adsorbed to the inner surface. The findings are important for the field of nanofluidics and provide an excellent system for efficient energy down-conversion in the transmission window of biological tissue.

Having separated the pure effect of solvent adsorption allowed us to study the undisturbed molecular adsorption of polymers in these systems. The addition of polyfluorene polymer leads to a slow but stepwise intensity increase. The intensity increase is overlapping with a concurrent process that leads to an intensity decrease. Unfortunately, observing the stepwise process has a low spacial resolution of only 100-250nm, which is in the range of the exciton diffusion length in these systems and hinders detailed analysis. The two competing and overlapping processes processes are considered to originate from slow π-stacking and fast side-chain binding. Insights into this process are essential for selecting suitably formed polymers. However, the findings also emphasize the importance of solvent selection during nanotube dispersion since solvent effects were proven to be far more critical on the quantum yield in these systems. These measurements can shed light on the ongoing debate on polymers adsorption during nanotube individualization and allow us to direct the discussion more towards the selection of suitable solvents.

This work provides fundamental insights into the adsorption of various molecules on the surface of individually observed suspended Single-Wall Carbon Nanotubes. It allows observing the adsorption of individual molecules below the optical limit in the solid, liquid, and gas phases. Nanotubes are able to act as sensing material for detecting changes in their direct surrounding. These fundamental findings are also crucial for increasing the quantum yield of solvent-dispersed nanotubes. They can provide better light-harvesting systems for microscopy in biological tissue and set the base for a more efficient telecommunication infrastructure with nano-scale spintronics devices and lasing components. The newly discovered solvent alignment in the nanotube surrounding can potentially also be used for supercapacitors that are needed for caching the calculation results in computational devices that use polymer wrapped nanotubes as transistors. Although fundamental, these studies develop a strategy to enlighten this room that is barely only visible at the bottom of the nano-scale.

4.1 Zusammenfassung

Nanoelektronik ist eine wichtige Technologie um das Größen-Limit gegenwärtiger Silizium-basierter Technologie zu überwinden. Einwandige Kohlenstoffnanoröhren sind halbleitende Moleküle, die eine Reihe von Eigenschaften dafür zur Verfügung stellen. Sie sind einsetzbar als Sensoren, in der Fernmeldetechnik und für elektronische Rechenoperationen. Aufgrund ihres hohen Verhältnisses von Oberfläche zu Volumen werden nahezu alle Eigenschaften von Kohlenstoffnanoröhren stark von Adsorption beeinflusst.

Einwandige Kohlenstoffnanoröhren mit kleineren Durchmessern (0.7-0.9nm) zeigen einen stärkeren Einfluss auf Phänomene, die an der Oberfläche auftreten. Um speziell diese Nanoröhren genauer zu untersuchen wurde eine Synthese Strategie entwickelt, die Nanoröhren mit hoher Qualität und Länge herstellen kann und dabei eine saubere Oberfläche gewährleisten ohne ihre Emissions-Stärke durch Bündelung zu verlieren. Die erhaltenen Ergebnisse unterstützen Studien aus der Literatur, die zumeist an Röhren mit größeren Durchmessern durchgeführt wurden. Die Größe des Datensatzes erlaubt es, Nanoröhren mit perfekten Emissions-Eigenschaften und großer mechanischer Stabilität auszuwählen.

Adsorptionen beeinflussen die Bewegung und Bindungs-Stärke der Excitonen, da sie ein Coulomb Potential an der Außenseite der Röhre ausbilden. Um die Adsorptionsprozess an der Oberfläche mit minimalen konkurrierenden Effekten zu untersuchen, wurde ein spezielles mikroskopisches Setup gewählt und eine Messmethode entwickelt um dieses System zu untersuchen. Das System wurde mit Hilfe von Bildern und Spektren charakterisiert. Über eine Simulation wurde außerdem gezeigt dass die untersuchten Nanoröhren große Diffusionslängen (>350nm) und Exciton Größen (<8.5nm) besitzen müssen.

Der Adsorptions Prozess an Kohlenstoffnanoröhren wurde sowohl mit Molekülen in der Gas-Phase untersucht, also auch in Lösungsmitteln und mit Feststoffen. Alle Experimente wurde dabei an frei hängenden Röhren durchgeführt, die auf einem Silizium Wafer Substrat aufgebracht wurden.

Die Experimente in der Gas Phase zeigten, dass die excitonische Emissions-Energie eine instantane und schnelle Blauverschiebung erfährt wenn die Nanoröhren mit einem Laser angeregt werden. Diese Verschiebung wurde auf die Desorption von Oberflächenverunreinigungen zurückgeführt, die an Luft inhärent die Messung beeinflussen. Durch die Annahme, nach der Untersuchung eine reine Oberfläche zu erhalten, konnte die Referenz der Vakkum-Emission erstellt werden, was es ermöglicht, den Einfluss der dielektrischen Umgebung genauer zu bestimmen. In einem weitern Experiment wurde die Adsorption von Wasserstoff getestet. In diesen Systemen bildet sich durch die Ausbildung von sp^3-Defekten eine neue Emissionsbande aus. Solche Emissionen werden derzeit für die Anwendung als Einzelphotonenemitter diskutiert. Die hier vorgestellte Methode erlaubt die direkte Synthese solcher Systeme im CVD Ofen.

Die frei hängenden Nanoröhren wurden weiter analysiert um den Effekt des Lösungsmittels auf die Emission detailiert zu untersuchen. Es wurde gezeigt, dass in Hexan und Acetonitril ein signifikant hoher Quantenausbeute-Verlust zu beobachten ist. Toluol hingegen zeigte sich hier am Besten. Die Energie-Verschiebungen waren insignifikant unterschiedlich zwischen den Lösungsmitteln. Ein Spezialfall war bei Acetonitril zu beobachten, in dem sich über den Zeitraum von 24h eine starke Emission herausbildet, die auf eine Kopplung mit Lösungsmittel-Schwingungen zurückgeführt wird. Die Stärke dieser Emission erlaubt die Vermutung, dass es sich um eine gekoppelte Schwingung von linear orientiertem Acetonitril in der Nanoröhre handelt. Eine solch starke Emission könnte zu Anwendungen in Zell-Gewebe führen, da weder Anregung noch Emission sich im Fenster der Blut- und Wasserabsorption befindet.

Durch die eindeutige Identifizierung von Lösungsmitteleffekten auf die Dispergierung von Kohlenstoffnanoröhren war es möglich, den Prozess der Anlagerung von Polyfluorene Polymeren direkt zu beobachten. Das Hinzufügen von Polymer zur Lösung führt zu einem schrittweisen reversiblen Anstieg der Emissions Intensität. Dieser Anstieg wird von einem gleichzeitigen irreversiblen schrittweisen Abfall der Emissionsintensität begleitet. Leider ist das System nur geeignet, Adsorptionen bis maximal 100nm Länge aufzulösen. Eine detaillierte Analyse ist daher schwer. Trotzdem wird vermutet, dass es sich bei dem langsamen Prozess um das Ausbilden von π-Stapeln handelt, wobei der schnelle Prozess mit der nicht-kovalenten Bindung der Polymer-Seitenketten an die Oberfläche assoziiert wird. Obwohl über die eigentliche Bindung des Polymers nur Vermutungen angestellt werden können, so wirft die Untersuchung doch einen Fokus auf die Wahl des Lösungsmittels, da diese Entscheidung einen viel größeren Effekt verursacht, als die

Bindung des Polymers selbst.

Diese Arbeit stellt fundamentale Betrachtungen zur Adsorption von verschiedenen Molekülen an Kohlenstoffnanoröhren auf. Die Betrachtungen wurden mit festen, flüssigen und gasförmigen Molekülen durchgeführt. Die Ergebnisse zeigen, dass Nanoröhren geeignet sind, als Molekül-Sensoren verwendet zu werden, da sie stark auf Änderungen in ihrer Umgebung reagieren können. Weiterhin wurden Lösungsmittel und Eigenschaften aufgezeigt, die die Quanteneffizienz signifikant beeinflussen. Eine Anwendung in der biologischen Mikroskopie ist denkbar, genauso wie für eine effizientere und sicherere Fernmeldeinfrastruktur. Weiterhin wurden Wege aufgezeigt, Super-Kondensatoren auf Nanorohr-Basis zu bauen, die als Anwendung in einem Kohlenstoffnanorohr-basierenden Computer von Interesse sein könnten. Obwohl die Erkenntnisse fundamental sind, zeigen diese Studien, dass es mit bestimmten Tricks möglich ist, den Raum am unteren Ende der Nanometerskala zu erforschen und zu entdecken.

FIVE

APPENDIX

All sources are available online https://gitlab.com/ukos-git/nanotubes. The built is deployed on https://ukos-git.gitlab.io/nanotubes with the most recent pdf version.

Built from git revision:

Commit 94d55e9

Changes after submission of thesis:

- 94d55e9 Merge branch 'review_hertel' into 'master' at 2020-09-16 16:41:28

  > Review Tobias Hertel
  >
  > See merge request ukos-git/nanotubes!11

- 1b7c714 Remove Github banner on html output at 2020-09-15 21:53:34

  > Alabaster theme is not able to handle gitlab refs. Remove the link to
  > gitlab page from the navigation bar.

- c825499 Update QR Code at 2020-09-15 21:50:14

  > Let QR code point to https://matthias-kastner.de

- bf360e2 Fill-in Chairperson and dates at 2020-09-15 20:18:35

  > Update dates of actual thesis defense, submission, and chair.

- 4f15d69 Fix Hamiltonian at 2020-07-26 19:21:55

  > Add negative sign to kinetic energy term in Hamiltonian.

- c7b3b43 Fix citation formatting at 2020-07-26 19:11:33

> The citation for Torrens et al. did not display correctly.

- fdf2135 Track Procedure Files For Changes at 2020-03-28 19:19:24

> Automaticall track `*.ipf` and `*.pxp` for changes instead of rebuilding
> the gitlab runner cache.

- 60b597f Optional Change Request by Tobias Hertel at 2020-03-21 19:24:12

> Optional changes suggested by the primary reviewer. These changes mainly
> contribute to readability of some passages.
>
> - include axis label 0,1 in gatevoltage graph
> - update right axis description to not be cut off
> - rewording
>   - "low amount" → "small number"
>   - "digitalization" → "digitization"
>   - clarify diameter and emission wavelength dependence on (6,5) type
>   - use *photoluminescece* quantum yield
>   - "strong influence" → "strong sensitivity"
> - typography error
>   - "ventile" → "valve"
>   - "dielectricum" → "dielectric"
>   - "Tanahaka" → "Tanaka"
>   - "spacial" → "spatial"
> - automatic rebuild of graph macros from stored ipf files
> - clarify diamond and circle symbols in violin plots
> - clarify faulty chiral assignment for spectra.
> - clarify strong emission as the phenomenon visible in the graph
>   `analyzed/mkl44/mkl44acnMaps/combined.png`
>
> For a detailed diff, go to the git repo.

- 26dad3d Change Request by Tobias Hertel at 2020-03-21 19:23:00

> Mandatory changes requested by the primary reviewer
> `tobias.hertel@uni-wuerzburg.de`.
>
> - replace dummy label (n,m) in figure
> - add missing radius r to Hamiltonian
> - include unit Debye

```
- clarify angle calculation
```

- 0c73a8e Include Changes Since Submission at 2020-03-21 20:12:11

```
To add transparency, any changes to the thesis after submission are
tracked using git. The repository is at
https://gitlab.com/ukos-git/nanotubes
```

BIBLIOGRAPHY

[1] Gordon E. Moore. Cramming more components onto integrated circuits. Electronics, 38(8):114ff, 1965. doi:10.1109/n-ssc.2006.4785860.

[2] Shigeo Maruyama, Ryosuke Kojima, Yuhei Miyauchi, Shohei Chiashi, and Masamichi Kohno. Low-temperature synthesis of high-purity single-walled carbon nanotubes from alcohol. Chemical Physics Letters, 360(3–4):229–234, 2002. doi:10.1016/S0009-2614(02)00838-2.

[3] Rodrigo B. Capaz, Catalin D. Spataru, Sohrab Ismail-Beigi, and Steven G. Louie. Excitons in carbon nanotubes: diameter and chirality trends. physica status solidi (b), 244(11):4016–4020, 2007. doi:10.1002/pssb.200776200.

[4] Bo Hou, Cheng Wu, Taiki Inoue, Shohei Chiashi, Rong Xiang, and Shigeo Maruyama. Extended alcohol catalytic chemical vapor deposition for efficient growth of single-walled carbon nanotubes thinner than (6,5). Carbon, 119:502–510, 2017. doi:10.1016/j.carbon.2017.04.045.

[5] Theerapol Thurakitseree, Christian Kramberger, Pei Zhao, Shohei Chiashi, Erik Einarsson, and Shigeo Maruyama. Reduction of single-walled carbon nanotube diameter to sub-nm via feedstock. Physica Status Solidi B: Basic Solid State Physics, 249(12):2404–2407, 2012. doi:10.1002/pssb.201200126.

[6] Adrian Nish, Jeong-Yuan Hwang, James Doig, and Robin J. Nicholas. Highly selective dispersion of single-walled carbon nanotubes using aromatic polymers. Nature nanotechnology, 2(10):640–646, 2007. doi:10.1038/nnano.2007.290.

[7] Darryl Fong and Alex Adronov. Recent developments in the selective dispersion of single-walled carbon nanotubes using conjugated polymers. Chemical science, 8(11):7292–7305, 2017. doi:10.1039/C7SC02942J.

[8] Aaron D. Franklin, Mathieu Luisier, Shu-Jen Han, George Tulevski, Chris M. Breslin, Lynne Gignac, Mark S. Lundstrom, and Wilfried Haensch. Sub-10 nm carbon nanotube transistor. Nano Letters, 12(2):758–762, 2012. doi:10.1021/nl203701g.

[9]   Max M. Shulaker, Gage Hills, Nishant Patil, Hai Wei, Hong-Yu Chen, H-S Philip Wong, and Subhasish Mitra. Carbon nanotube computer. Nature, 501(7468):526–530, 2013. doi:10.1038/nature12502.

[10]   Oleg N. Kalugin, Vitaly V. Chaban, Valentin V. Loskutov, and Oleg V. Prezhdo. Uniform diffusion of acetonitrile inside carbon nanotubes favors supercapacitor performance. Nano Letters, 8(8):2126–2130, 2008. doi:10.1021/nl072976g.

[11]   Ardemis A. Boghossian, Jingqing Zhang, Paul W. Barone, Nigel F. Reuel, Jong-Ho Kim, Daniel A. Heller, Jin-Ho Ahn, Andrew J. Hilmer, Alina Rwei, Jyoti R. Arkalgud, Cathy T. Zhang, and Michael S. Strano. Near-infrared fluorescent sensors based on single-walled carbon nanotubes for life sciences applications. ChemSusChem, 4(7):848–863, 2011. doi:10.1002/cssc.201100070.

[12]   Alexander Högele, Christophe Galland, Martin Winger, and Atac Imamoğlu. Photon antibunching in the photoluminescence spectra of a single carbon nanotube. Physical review letters, 100(21):217401, 2008. doi:10.1103/PhysRevLett.100.217401.

[13]   Matthias S. Hofmann, Jan T. Gluckert, Jonathan Noe, Christian Bourjau, Raphael Dehmel, and Alexander Hogele. Bright, long-lived and coherent excitons in carbon nanotube quantum dots. Nature nanotechnology, 8(7):502–505, 2013. doi:10.1038/nnano.2013.119.

[14]   Thomas Mueller, Megumi Kinoshita, Mathias Steiner, Vasili Perebeinos, Ageeth A. Bol, Damon B. Farmer, and Phaedon Avouris. Efficient narrow-band light emission from a single carbon nanotube p-n diode. Nature nanotechnology, 5(1):27–31, 2010. doi:10.1038/nnano.2009.319.

[15]   Noémie Danné, Antoine G. Godin, Zhenghong Gao, Juan A. Varela, Laurent Groc, Brahim Lounis, and Laurent Cognet. Comparative analysis of photoluminescence and upconversion emission from individual carbon nanotubes for bioimaging applications. ACS Photonics, 5(2):359–364, 2018. doi:10.1021/acsphotonics.7b01311.

[16]   Xiaowei He, Nicolai F. Hartmann, Xuedan Ma, Younghee Kim, Rachelle Ihly, Jeffrey L. Blackburn, Weilu Gao, Junichiro Kono, Yohei Yomogida, Atsushi Hirano, Takeshi Tanaka, Hiromichi Kataura, Han Htoon, and Stephen K. Doorn. Tunable room-temperature single-photon emission at telecom wavelengths from sp3 defects in carbon nanotubes. Nature Photonics, 11(9):577–582, 2017. doi:10.1038/nphoton.2017.119.

[17]   Xiaowei He, Brendan J. Gifford, Nicolai F. Hartmann, Rachelle Ihly, Xuedan Ma, Svetlana V. Kilina, Yue Luo, Kamran Shayan, Stefan Strauf, Jeffrey L. Blackburn, Sergei Tretiak, Stephen K. Doorn, and Han Htoon. Low-temperature single carbon

nanotube spectroscopy of sp3 quantum defects. ACS nano, 11(11):10785–10796, 2017. doi:10.1021/acsnano.7b03022.

[18] X. He, H. Htoon, S. K. Doorn, W. H. P. Pernice, F. Pyatkov, R. Krupke, A. Jeantet, Y. Chassagneux, and C. Voisin. Carbon nanotubes as emerging quantum-light sources. Nature materials, 17(8):663–670, 2018. doi:10.1038/s41563-018-0109-2.

[19] A. Nikitin, H. Ogasawara, D. Mann, R. Denecke, Z. Zhang, H. Dai, K. Cho, and A. Nilsson. Hydrogenation of single-walled carbon nanotubes. Physical review letters, 95(22):225507, 2005. doi:10.1103/PhysRevLett.95.225507.

[20] Ulrich Hofmann. Adsorptionsvermögen, katalytische aktivität und kristalline struktur des kohlenstoffs. Angewandte Chemie, 44(41):841–845, 1931. doi:10.1002/ange.19310444102.

[21] Ulrich Hofmann and Edeltraut Groll. Durch thermischen zerfall von benzin im gasraum dargestellter kohlenstoff. Berichte der deutschen chemischen Gesellschaft (A and B Series), 65(8):1257–1267, 1932. doi:10.1002/cber.19320650804.

[22] K. A. Hofmann and Curt Röchling. Die glanzkohle, eine besondere form des krystallinen kohlenstoffs. Berichte der deutschen chemischen Gesellschaft (A and B Series), 56(8):2071–2076, 1923. doi:10.1002/cber.19230560863.

[23] K. A. Hofmann and Ulrich Hofmann. Der glanzkohlenstoff als anfang der schwarzen krystallinen kohlenstoffreihe. Berichte der deutschen chemischen Gesellschaft (A and B Series), 59(10):2433–2444, 1926. doi:10.1002/cber.19260591002.

[24] Karl Fredenhagen and Gustav Cadenbach. Die bindung von kalium durch kohlenstoff. Zeitschrift fr anorganische und allgemeine Chemie, 158(1):249–263, 1926. doi:10.1002/zaac.19261580122.

[25] L. Persichetti, M. De Seta, A. M. Scaparro, V. Miseikis, A. Notargiacomo, A. Ruocco, A. Sgarlata, M. Fanfoni, F. Fabbri, C. Coletti, and L. Di Gaspare. Driving with temperature the synthesis of graphene films and nanoribbons on ge(110). URL: http://arxiv.org/pdf/1906.01571v1.

[26] nobelprize.org. The nobel prize in physics 1986. 1986. URL: http://www.nobelprize.org/nobel_prizes/physics/laureates/1986.

[27] M. v. Ardenne and U. Hofmann. Elektronenmikroskopische und röntgenographische untersuchungen über die struktur von rußen. Zeitschrift für Physikalische Chemie, 50B(1):1–12, 1941. doi:10.1515/zpch-1941-5002.

[28] Marc Monthioux and Vladimir L. Kuznetsov. Who should be given the credit for the discovery of carbon nanotubes? Carbon, 44(9):1621–1623, 2006. doi:10.1016/j.carbon.2006.03.019.

[29] Л. В. Радушкевич and В. М. Лункянович. О структуре углерода, образующегося при термическом разложении окиси углерода на железном контакте: about the structure of carbon formed by thermal decomposition of carbon monoxide on iron substrate. Журн. физ. химии (ЖУРНАЛ ФИЗИЧЕСКОЙ ХИМИИ), 26:88–95, 1952. URL: https://nanotube.msu.edu/HSS/2006/4.

[30] R. Iley and H. L. Riley. 274. the deposition of carbon on vitreous silica. Journal of the Chemical Society (Resumed), pages 1362, 1948. doi:10.1039/JR9480001362.

[31] W. R. Davis, R. J. Slawson, and G. R. Rigby. An unusual form of carbon. Nature, 171(4356):756, 1953. doi:10.1038/171756a0.

[32] P. L. Walker, J. F. Rakszawski, and G. R. Imperial. Carbon formation from carbon monoxide-hydrogen mixtures over iron catalysts.i. properties of carbon formed. The Journal of Physical Chemistry, 63(2):133–140, 1959. doi:10.1021/j150572a002.

[33] Roger Bacon. Growth, structure, and properties of graphite whiskers. Journal of Applied Physics, 31(2):283–290, 1960. doi:10.1063/1.1735559.

[34] H. W. Kroto, J. R. Heath, S. C. O'Brien, R. F. Curl, and Smalley, R. E. C60: buckminsterfullerene. Nature, 318(6042):162–163, 1985. doi:10.1038/318162a0.

[35] Sumio Iijima. Helical microtubules of graphitic carbon. Nature, 354(6348):56–58, 1991. doi:10.1038/354056a0.

[36] R. Saito, M. Fujita, G. Dresselhaus, and M. S. Dresselhaus. Electronic structure of chiral graphene tubules. Applied Physics Letters, 60(18):2204–2206, 1992. doi:10.1063/1.107080.

[37] Sumio Iijima and Toshinari Ichihashi. Single-shell carbon nanotubes of 1-nm diameter. Nature, 363(6430):603–605, 1993. doi:10.1038/363603a0.

[38] Tsuneya Ando. Excitons in carbon nanotubes. Journal of the Physics Society Japan, 66(4):1066–1073, 1997. doi:10.1143/JPSJ.66.1066.

[39] J. Maultzsch, R. Pomraenke, S. Reich, E. Chang, D. Prezzi, A. Ruini, E. Molinari, M. S. Strano, C. Thomsen, and C. Lienau. Exciton binding energies in carbon nanotubes from two-photon photoluminescence. Nano Letters, 72(24):6680, 2005. doi:10.1103/PhysRevB.72.241402.

[40] H. Kataura, Y. Kumazawa, Y. Maniwa, I. Umezu, S. Suzuki, Y. Ohtsuka, and Y. Achiba. Optical properties of single-wall carbon nanotubes. Synthetic Metals, 103(1-3):2555–2558, 1999. doi:10.1016/S0379-6779(98)00278-1.

[41] Kaihui Liu, Jack Deslippe, Fajun Xiao, Rodrigo B. Capaz, Xiaoping Hong, Shaul Aloni, Alex Zettl, Wenlong Wang, Xuedong Bai, Steven G. Louie, Enge Wang, and

Feng Wang. An atlas of carbon nanotube optical transitions. Nature nanotechnology, 7(5):325–329, 2012. doi:10.1038/nnano.2012.52.

[42] T. Guo, P. Nikolaev, A. Thess, D. T. Colbert, and Smalley, R. E. Catalytic growth of single-walled manotubes by laser vaporization. Chemical Physics Letters, 243(1-2):49–54, 1995. doi:10.1016/0009-2614(95)00825-O.

[43] H. Kataura, Y. Kumazawa, Y. Maniwa, Y. Ohtsuka, R. Sen, S. Suzuki, and Y. Achiba. Diameter control of single-walled carbon nanotubes. Carbon, 38(11-12):1691–1697, 2000. doi:10.1016/S0008-6223(00)00090-7.

[44] Sivaram Arepalli. Laser ablation process for single-walled carbon nanotube production. Journal of Nanoscience and Nanotechnology, 4(4):317–325, 2004. doi:10.1166/jnn.2004.072.

[45] C. Journet and P. Bernier. Production of carbon nanotubes. Applied Physics A: Materials Science & Processing, 67(1):1–9, 1998. doi:10.1007/s003390050731.

[46] Yiming Li, David Mann, Marco Rolandi, Woong Kim, Ant Ural, Steven Hung, Ali Javey, Jien Cao, Dunwei Wang, Erhan Yenilmez, Qian Wang, James F. Gibbons, Yoshio Nishi, and Hongjie. Dai. Preferential growth of semiconducting single-walled carbon nanotubes by a plasma enhanced cvd method. Nano Letters, 4(2):317–321, 2004. doi:10.1021/nl035097c.

[47] Yuhei Miyauchi. Photoluminescence studies on exciton photophysics in carbon nanotubes. Journal of Materials Chemistry C, 1(40):6499, 2013. doi:10.1039/c3tc00947e.

[48] Nasiba Abdurakhmanova, A. Mueller, S. Stepanow, S. Rauschenbach, M. Jansen, K. Kern, and K. Yu Amsharov. Bottom up fabrication of (9, 0) zigzag and (6, 6) armchair carbon nanotube end-caps on the rh(1 1 1) surface. Carbon, 84:444–447, 2015. doi:10.1016/j.carbon.2014.12.038.

[49] Chin Li Cheung, Andrea Kurtz, Hongkun Park, and Charles M. Lieber. Diameter-controlled synthesis of carbon nanotubes. Journal of Physical Chemistry B, 106(10):2429–2433, 2002. doi:10.1021/jp0142278.

[50] Konstantin Yu. Amsharov. Combinatorial approach for the synthesis of precursors for chirality-controlled synthesis of swcnts. Physica Status Solidi B: Basic Solid State Physics, 252(11):2466–2471, 2015. doi:10.1002/pssb.201552189.

[51] Chiang, I. W., Brinson, B. E., Huang, A. Y., Willis, P. A., Bronikowski, M. J., Margrave, J. L., Smalley, R. E., and Hauge, R. H. Purification and characterization of single-wall carbon nanotubes (swnts) obtained from the gas-phase decomposition of co (hipco process). Journal of Physical Chemistry B, 105(35):8297–8301, 2001. doi:10.1021/jp0114891.

[52] Hongjie Dai, Andrew G. Rinzler, Pasha Nikolaev, Andreas Thess, Daniel T. Colbert, and Richard E. Smalley. Single-wall nanotubes produced by metal-catalyzed disproportionation of carbon monoxide. Chemical Physics Letters, 260(3,4):471–475, 1996. doi:10.1016/0009-2614(96)00862-7.

[53] Jing Kong, Alan M. Cassell, and Hongjie. Dai. Chemical vapor deposition of methane for single-walled carbon nanotubes. Chemical Physics Letters, 292(4,5,6):567–574, 1998. doi:10.1016/S0009-2614(98)00745-3.

[54] J.-F. Colomer, C. Stephan, S. Lefrant, G. van Tendeloo, I. Willems, Z. Konya, A. Fonseca, C. Laurent, and Nagy, J. B. Large-scale synthesis of single-wall carbon nanotubes by catalytic chemical vapor deposition (ccvd) method. Chemical Physics Letters, 317(1,2):83–89, 2000. doi:10.1016/S0009-2614(99)01338-X.

[55] Jason H. Hafner, Michael J. Bronikowski, Bobak R. Azamian, Pavel Nikolaev, Andrew G. Rinzler, Daniel T. Colbert, Ken A. Smith, and Richard E. Smalley. Catalytic growth of single-wall carbon nanotubes from metal particles. Chemical Physics Letters, 296(1,2):195–202, 1998. doi:10.1016/S0009-2614(98)01024-0.

[56] Gayatri Keskar, Rahul Rao, Jian Luo, Joan Hudson, Jia Chen, and Apparao M. Rao. Growth, nitrogen doping and characterization of isolated single-wall carbon nanotubes using liquid precursors. Chemical Physics Letters, 412(4-6):269–273, 2005. doi:10.1016/j.cplett.2005.07.007.

[57] Mukul Kumar and Yoshinori Ando. Controlling the diameter distribution of carbon nanotubes grown from camphor on a zeolite support. Carbon, 43(3):533–540, 2005. doi:10.1016/j.carbon.2004.10.014.

[58] Rahul Sen, A. Govindaraj, and C.N.R. Rao. Carbon nanotubes by the metal-locene route. Chemical Physics Letters, 267(3-4):276–280, 1997. doi:10.1016/S0009-2614(97)00080-8.

[59] Yan Zhang, Weiwei Zhou, Zhong Jin, Li Ding, Zhiyong Zhang, Xuelei Liang, and Yan Li. Direct growth of single-walled carbon nanotubes without metallic residues by using lead as a catalyst. Chemistry of Materials, 20(24):7521–7525, 2008. doi:10.1021/cm801024c.

[60] Dongning Yuan, Lei Ding, Haibin Chu, Yiyu Feng, Thomas P. McNicholas, and Jie Liu. Horizontally aligned single-walled carbon nanotube on quartz from a large variety of metal catalysts. Nano Letters, 8(8):2576–2579, 2008. doi:10.1021/nl801007r.

[61] Feng Yang, Xiao Wang, Daqi Zhang, Juan Yang, LuoDa, Ziwei Xu, Jiake Wei, Jian-Qiang Wang, Zhi Xu, Fei Peng, Xuemei Li, Ruoming Li, Yilun Li, Meihui Li, Xuedong Bai, Feng Ding, and Yan Li. Chirality-specific growth of single-

walled carbon nanotubes on solid alloy catalysts. Nature, 510(7506):522–524, 2014. doi:10.1038/nature13434.

[62] Codruta Zoican Loebick, Salim Derrouiche, Nebojsa Marinkovic, Chuan Wang, Frank Hennrich, Manfred M. Kappes, Haller, Gary. L., and Pfefferle, Lisa. D. Effect of manganese addition to the co-mcm-41 catalyst in the selective synthesis of single wall carbon nanotubes. The Journal of Physical Chemistry C, 113(52):21611–21620, 2009. URL: http://dx.doi.org/10.1021/jp908262u, doi:10.1021/jp908262u.

[63] Codruta Zoican Loebick, Ramakrishna Podila, Jason Reppert, Joel Chudow, Fang Ren, Gary L. Haller, Apparao M. Rao, and Lisa D. Pfefferle. Selective synthesis of subnanometer diameter semiconducting single-walled carbon nanotubes. Journal of the American Chemical Society, 132(32):11125–11131, 2010. doi:10.1021/ja102011h.

[64] Yuhei Miyauchi, Shohei Chiashi, Yoichi Murakami, Yasunori Hayashida, and Shigeo Maruyama. Fluorescence spectroscopy of single-walled carbon nanotubes synthesized from alcohol. Chemical Physics Letters, 387(1–3):198–203, 2004. doi:10.1016/j.cplett.2004.01.116.

[65] Lianxi Zheng, B. C. Satishkumar, Pingqi Gao, and Qing Zhang. Kinetics studies of ultralong single-walled carbon nanotubes. The Journal of Physical Chemistry C, 113(25):10896–10900, 2009. doi:10.1021/jp901640d.

[66] Sergei M. Bachilo, Leandro Balzano, Jose E. Herrera, Francisco Pompeo, Daniel E. Resasco, and Weisman, R. Bruce. Narrow (n,m)-distribution of single-walled carbon nanotubes grown using a solid supported catalyst. Journal of the American Chemical Society, 125(37):11186–11187, 2003. doi:10.1021/ja036622c.

[67] Kehang Cui, Akihito Kumamoto, Rong Xiang, Hua An, Benjamin Wang, Taiki Inoue, Shohei Chiashi, Yuichi Ikuhara, and Shigeo Maruyama. Synthesis of subnanometer-diameter vertically aligned single-walled carbon nanotubes with copper-anchored cobalt catalysts. Nanoscale, 8(3):1608–1617, 2016. doi:10.1039/C5NR06007A.

[68] Young Lee, Seong Kim, and David Tománek. Catalytic growth of single-wall carbon nanotubes: an ab initio study. Physical Review Letters, 78(12):2393–2396, 1997. doi:10.1103/PhysRevLett.78.2393.

[69] Stephanie Reich, Lan Li, and John Robertson. Control the chirality of carbon nanotubes by epitaxial growth. Chemical Physics Letters, 421(4-6):469–472, 2006. doi:10.1016/j.cplett.2006.01.110.

[70] Muhammad Mansoor, Muhammad Shahid, and Amir Habib. Optimization of ethanol flow rate for improved catalytic activity of ni particles to synthesize mwcnts

using a cvd reactor. Materials Research, 17(3):739–746, 2014. doi:10.1590/S1516-14392014005000070.

[71] Weiwei Zhou, Zuoyan Han, Jinyong Wang, Yan Zhang, Zhong Jin, Xiao Sun, Yawen Zhang, Chunhua Yan, and Yan Li. Copper catalyzing growth of single-walled carbon nanotubes on substrates // copper catalyzing growth of single-walled carbon nanotubes on substrates. Nano Letters, 6(12):2987–2990, 2006. doi:10.1021/nl061871v.

[72] Maoshuai He, Alexander I. Chernov, Pavel V. Fedotov, Elena D. Obraztsova, Jani Sainio, Emma Rikkinen, Hua Jiang, Zhen Zhu, Ying Tian, Esko I. Kauppinen, Marita Niemelä, and Krause, A. Outi I. Predominant (6,5) single-walled carbon nanotube growth on a copper-promoted iron catalyst. Journal of the American Chemical Society, 132(40):13994–13996, 2010. URL: http://dx.doi.org/10.1021/ja106609y, doi:10.1021/ja106609y.

[73] Xiaolin Li, Xiaomin Tu, Sasa Zaric, Kevin Welsher, Won Seok Seo, Wei Zhao, and Hongjie Dai. Selective synthesis combined with chemical separation of single-walled carbon nanotubes for chirality selection. Journal of the American Chemical Society, 129(51):15770–15771, 2007. URL: http://dx.doi.org/10.1021/ja077886s, doi:10.1021/ja077886s.

[74] Theerapol Thurakitseree, Erik Einarsson, Rong Xiang, Pei Zhao, Shinya Aikawa, Shohei Chiashi, Junichiro Shiomi, and Shigeo Maruyama. Diameter controlled chemical vapor deposition synthesis of single-walled carbon nanotubes. Journal of Nanoscience and Nanotechnology, 12(1):370–376, 2012. doi:10.1166/jnn.2012.5398.

[75] Bilu Liu, Wencai Ren, Shisheng Li, Chang Liu, and Hui-Ming Cheng. High temperature selective growth of single-walled carbon nanotubes with a narrow chirality distribution from a copt bimetallic catalyst. Chemical Communications, 48(18):2409–2411, 2012. doi:10.1039/C2CC16491D.

[76] Sreekar Bhaviripudi, Ervin Mile, Stephen A. Steiner, Aurea T. Zare, Mildred S. Dresselhaus, Angela M. Belcher, and Jing Kong. Cvd synthesis of single-walled carbon nanotubes from gold nanoparticle catalysts. Journal of the American Chemical Society, 129(6):1516–1517, 2007. doi:10.1021/ja0673332.

[77] B. Kitiyanan, W. E. Alvarez, J. H. Harwell, and D. E. Resasco. Controlled production of single-wall carbon nanotubes by catalytic decomposition of co on bimetallic co–mo catalysts. Chemical Physics Letters, 317(3–5):497–503, 2000. doi:10.1016/S0009-2614(99)01379-2.

[78] Matthias Kastner, Sabine Stahl, Ivonne Vollert, Christian Loi, Nicolas Rühl, Tobias Hertel, and Friedrich Schöppler. A comparison of raman and photoluminescence spectra for the assessment of single-wall carbon nanotube sample quality. Chemical Physics Letters, 635:245–249, 2015. doi:10.1016/j.cplett.2015.06.076.

[79] Hisayoshi Oshima, Yoshinobu Suzuki, Tomohiro Shimazu, and Shigeo Maruyama. Novel and simple synthesis method for submillimeter long vertically aligned single-walled carbon nanotubes by no-flow alcohol catalytic chemical vapor deposition. Japanese Journal of Applied Physics, 47(4):1982–1984, 2008. doi:10.1143/JJAP.47.1982.

[80] L. X. Zheng, M. J. O'Connell, S. K. Doorn, X. Z. Liao, Y. H. Zhao, E. A. Akhadov, M. A. Hoffbauer, B. J. Roop, Q. X. Jia, R. C. Dye, D. E. Peterson, S. M. Huang, J. Liu, and Y. T. Zhu. Ultralong single-wall carbon nanotubes. Nature materials, 3(10):673–676, 2004. doi:10.1038/nmat1216.

[81] David Bom, Rodney Andrews, David Jacques, John Anthony, Bailin Chen, Mark S. Meier, and John P. Selegue. Thermogravimetric analysis of the oxidation of multiwalled carbon nanotubes: evidence for the role of defect sites in carbon nanotube chemistry. Nano Letters, 2(6):615–619, 2002. doi:10.1021/nl020297u.

[82] Li Qingwen, Yan Hao, Ye Yinchun, Zhang Jin, and Liu Zhongfan. Defect location of individual single-walled carbon nanotubes with a thermal oxidation strategy. Journal of Physical Chemistry B, 106(43):11085–11088, 2002. doi:10.1021/jp026512c.

[83] Michael V. Osier, Andrew J. Pakstis, Himla Soodyall, David Comas, David Goldman, Adekunle Odunsi, Friday Okonofua, Josef Parnas, Leslie O. Schulz, Jaume Bertranpetit, Batsheva Bonne-Tamir, Ru-Band Lu, Judith R. Kidd, and Kenneth K. Kidd. A global perspective on genetic variation at the adh genes reveals unusual patterns of linkage disequilibrium and diversity. American journal of human genetics, 71(1):84–99, 2002. doi:10.1086/341290.

[84] Bo Hou, Rong Xiang, Taiki Inoue, Erik Einarsson, Shohei Chiashi, Junichiro Shiomi, Akira Miyoshi, and Shigeo Maruyama. Decomposition of ethanol and dimethyl ether during chemical vapor deposition synthesis of single-walled carbon nanotubes. Japanese Journal of Applied Physics, 50(6R):065101, 2011. doi:10.1143/JJAP.50.065101.

[85] Matthias J. Kastner. Herstellung halbleitender Kohlenstoffnanoröhren durch Gasphasenabscheidungsprozesse und spektroskopische Charakterisierung. PhD thesis, Uni Würzburg, Würzburg, 2014.

[86] Rong Xiang, Bo Hou, Erik Einarsson, Pei Zhao, Sivasankaran Harish, Kenichi Morimoto, Yuhei Miyauchi, Shohei Chiashi, Zikang Tang, and Shigeo Maruyama. Carbon atoms in ethanol do not contribute equally to formation of single-walled carbon nanotubes. ACS Nano, 7(4):3095–3103, 2013. doi:10.1021/nn305180g.

[87] Tomoya Oguri, Kohei Shimamura, Yasushi Shibuta, Fuyuki Shimojo, and Shu Yamaguchi. Bond dissociation mechanism of ethanol during carbon nanotube synthe-

sis via alcohol catalytic cvd technique: ab initio molecular dynamics simulation. Chemical Physics Letters, 595-596:185–191, 2014. doi:10.1016/j.cplett.2014.02.002.

[88] Kaoru Hisama, Ryo Yoshikawa, Teppei Matsuo, Takuya Noguchi, Tomoya Kawasuzuki, Shohei Chiashi, and Shigeo Maruyama. Growth analysis of single-walled carbon nanotubes based on interatomic potentials by molecular dynamics simulation. The Journal of Physical Chemistry C, 122(17):9648–9653, 2018. doi:10.1021/acs.jpcc.7b12687.

[89] Yoshifumi Izu, Junichiro Shiomi, Yoshiteru Takagi, Susumu Okada, and Shigeo Maruyama. Growth mechanism of single-walled carbon nanotube from catalytic reaction inside carbon nanotube template. ACS Nano, 4(8):4769–4775, 2010. doi:10.1021/nn100461r.

[90] Phillip Vinten, Paul Marshall, Jacques Lefebvre, and Paul Finnie. Thermodynamic and energetic effects on the diameter and defect density in single-walled carbon nanotube synthesis. The Journal of Physical Chemistry C, 117(7):3527–3536, 2013. doi:10.1021/jp308672a.

[91] W. Zhou, Y.H Ooi, R. Russo, P. Papanek, D.E Luzzi, J.E Fischer, M.J Bronikowski, P.A Willis, and R.E Smalley. Structural characterization and diameter-dependent oxidative stability of single wall carbon nanotubes synthesized by the catalytic decomposition of co. Chemical Physics Letters, 350(1-2):6–14, 2001. doi:10.1016/S0009-2614(01)01237-4.

[92] Husnu Emrah Unalan and Manish Chhowalla. Investigation of single-walled carbon nanotube growth parameters using alcohol catalytic chemical vapour deposition. Nanotechnology, 16(10):2153–2163, 2005. doi:10.1088/0957-4484/16/10/031.

[93] Charlotte T.M. Kwok, Brandon J. Reizman, Daniel E. Agnew, Gurjit S. Sandhu, J. Weistroffer, Michael S. Strano, and Edmund G. Seebauer. Temperature and time dependence study of single-walled carbon nanotube growth by catalytic chemical vapor deposition. Carbon, 48(4):1279–1288, 2010. doi:10.1016/j.carbon.2009.11.053.

[94] P. Vinten, J. Lefebvre, and P. Finnie. Kinetic critical temperature and optimized chemical vapor deposition growth of carbon nanotubes. Chemical Physics Letters, 469(4-6):293–297, 2009. doi:10.1016/j.cplett.2008.12.095.

[95] Nick M. Marinov. A detailed chemical kinetic model for high temperature ethanol oxidation. International Journal of Chemical Kinetics, 31(3):183–220, 1999. doi:10.1002/(SICI)1097-4601(1999)31:3<183::AID-KIN3>3.0.CO;2-X.

[96] Andreas Eisenhut. Cvd-wachstum halbleitender swnts auf si-oberflächen und bestimmung der swnt-durchmesserverteilung: bachelorarbeit. 2015.

[97] Michael J. O'Connell, Sergei M. Bachilo, Chad B. Huffman, Valerie C. Moore, Michael S. Strano, Erik H. Haroz, Kristy L. Rialon, Peter J. Boul, William H. Noon, Carter Kittrell, Jianpeng Ma, Robert H. Hauge, Weisman, R. Bruce, and Richard E. Smalley. Band gap fluorescence from individual single-walled carbon nanotubes. Science, 297(5581):593–596, 2002. doi:10.1126/science.1072631.

[98] Stefan Kupka. Synthese von kohlenstoffnanoröhren: diplomarbeit. 2012.

[99] Yoshikazu Homma, Yoshiro Kobayashi, Toshio Ogino, Daisuke Takagi, Roichi Ito, Yung Joon Jung, and Pulickel M. Ajayan. Role of transition metal catalysts in single-walled carbon nanotube growth in chemical vapor deposition. Journal of Physical Chemistry B, 107(44):12161–12164, 2003. doi:10.1021/jp0353845.

[100] Shohei Chiashi, Yuta Saito, Takashi Kato, Satoru Konabe, Susumu Okada, Takahiro Yamamoto, and Yoshikazu Homma. Confinement effect of sub-nanometer difference on melting point of ice-nanotubes measured by photoluminescence spectroscopy. ACS nano, 13(2):1177–1182, 2019. doi:10.1021/acsnano.8b06041.

[101] Bhupender S. Chhikara, Santosh K. Misra, and Santanu Bhattacharya. Cnt loading into cationic cholesterol suspensions show improved dna binding and serum stability and ability to internalize into cancer cells. Nanotechnology, 23(6):065101, 2012. doi:10.1088/0957-4484/23/6/065101.

[102] Michael S. Arnold, Samuel I. Stupp, and Mark C. Hersam. Enrichment of single-walled carbon nanotubes by diameter in density gradients. Nano Letters, 5(4):713–718, 2005. doi:10.1021/nl050133o.

[103] Alexander A. Green, Matthew C. Duch, and Mark C. Hersam. Isolation of single-walled carbon nanotube enantiomers by density differentiation. Nano Research, 2(1):69–77, 2009. doi:10.1007/s12274-009-9006-y.

[104] Daniel Zuleeg. Aufbau, Programmierung und Charakterisierung einer PLE-Spektrometrieanlage. PhD thesis, Uni Würzburg, Würzburg, 2015.

[105] Jae-Yel Yi and J. Bernholc. Atomic structure and doping of microtubules. Physical Review B, 47(3):1708–1711, 1993. doi:10.1103/PhysRevB.47.1708.

[106] Paola Ayala, Raul Arenal, Annick Loiseau, Angel Rubio, and Thomas Pichler. The physical and chemical properties of heteronanotubes. Reviews of Modern Physics, 82(2):1843–1885, 2010. doi:10.1103/RevModPhys.82.1843.

[107] Gordana Ciric-Marjanovic, Igor Pasti, and Slavko. Mentus. One-dimensional nitrogen-containing carbon nanostructures. Progress in Materials Science, 69:61–182, 2015. doi:10.1016/j.pmatsci.2014.08.002.

[108] Kuiyang Jiang, Linda S. Schadler, Richard W. Siegel, Xinjie Zhang, Haifeng Zhang, and Mauricio Terrones. Protein immobilization on carbon nanotubes via a two-step

process of diimide-activated amidation. Journal of Materials Chemistry, 14(1):37, 2004. doi:10.1039/B310359E.

[109] Lain-Jong Li, M. Glerup, A. N. Khlobystov, J. G. Wiltshire, J.-L. Sauvajol, R. A. Taylor, and R. J. Nicholas. The effects of nitrogen and boron doping on the optical emission and diameters of single-walled carbon nanotubes. Carbon, 44(13):2752–2757, 2006. doi:10.1016/j.carbon.2006.03.037.

[110] Joseph G. Wiltshire, Lain-Jong Li, Laura M. Herz, Robin J. Nicholas, Marianne Glerup, Jean-Louis Sauvajol, and Andrei N. Khlobystov. Chirality-dependent boron-mediated growth of nitrogen-doped single-walled carbon nanotubes. Physical Review B, 2005. doi:10.1103/PhysRevB.72.205431.

[111] M. Glerup, J. Steinmetz, D. Samaille, O. Stéphan, S. Enouz, A. Loiseau, S. Roth, and P. Bernier. Synthesis of n-doped swnt using the arc-discharge procedure. Chemical Physics Letters, 387(1-3):193–197, 2004. doi:10.1016/j.cplett.2004.02.005.

[112] F. Villalpando-Paez, A. Zamudio, A. L. Elias, H. Son, E. B. Barros, S. G. Chou, Y. A. Kim, H. Muramatsu, T. Hayashi, J. Kong, H. Terrones, G. Dresselhaus, M. Endo, M. Terrones, and M. S. Dresselhaus. Synthesis and characterization of long strands of nitrogen-doped single-walled carbon nanotubes. Chemical Physics Letters, 424(4-6):345–352, 2006. doi:10.1016/j.cplett.2006.04.074.

[113] Antal A. Koós, Frank Dillon, Ekaterina A. Obraztsova, Alison Crossley, and Nicole Grobert. Comparison of structural changes in nitrogen and boron-doped multi-walled carbon nanotubes. Carbon, 48(11):3033–3041, 2010. doi:10.1016/j.carbon.2010.04.026.

[114] M. Reyes-Reyes, N. Grobert, R. Kamalakaran, T. Seeger, D. Golberg, M. Rühle, Y. Bando, H. Terrones, and M. Terrones. Efficient encapsulation of gaseous nitrogen inside carbon nanotubes with bamboo-like structure using aerosol thermolysis. Chemical Physics Letters, 396(1-3):167–173, 2004. doi:10.1016/j.cplett.2004.07.125.

[115] Hyun Chul Choi, Jeunghee Park, and Bongsoo Kim. Distribution and structure of n atoms in multiwalled carbon nanotubes using variable-energy x-ray photoelectron spectroscopy. The journal of physical chemistry. B, 109(10):4333–4340, 2005. doi:10.1021/jp0453109.

[116] P. Ayala, A. Grüneis, T. Gemming, B. Büchner, M. H. Rümmeli, D. Grimm, J. Schumann, R. Kaltofen, Freire Jr., F. L., Filho, H. D. Fonseca, and T. Pichler. Influence of the catalyst hydrogen pretreatment on the growth of vertically aligned nitrogen-doped carbon nanotubes. Chemistry of Materials, 19(25):6131–6137, 2007. doi:10.1021/cm0715592.

[117] Paola Ayala, Alexander Grueneis, Thomas Gemming, Daniel Grimm, Christian Kramberger, Mark H. Ruemmeli, Freire, Fernando L. , Jr., Hans Kuzmany, Rudolf Pfeiffer, Amelia Barreiro, Bernd Buechner, and Thomas. Pichler. Tailoring n-doped single and double wall carbon nanotubes from a nondiluted carbon/nitrogen feedstock. The Journal of Physical Chemistry C, 111(7):2879–2884, 2007. doi:10.1021/jp0658288.

[118] E.M.M. Ibrahim, Vyacheslav O. Khavrus, Albrecht Leonhardt, Silke Hampel, Steffen Oswald, Mark H. Rümmeli, and Bernd Büchner. Synthesis, characterization, and electrical properties of nitrogen-doped single-walled carbon nanotubes with different nitrogen content. Diamond and Related Materials, 19(10):1199–1206, 2010. doi:10.1016/j.diamond.2010.05.008.

[119] Theerapol Thurakitseree, Christian Kramberger, Akihito Kumamoto, Shohei Chiashi, Erik Einarsson, and Shigeo Maruyama. Reversible diameter modulation of single-walled carbon nanotubes by acetonitrile-containing feedstock. ACS Nano, 7(3):2205–2211, 2013. doi:10.1021/nn3051852.

[120] V. Krstić, Rikken, G. L. J. A, P. Bernier, S. Roth, and M. Glerup. Nitrogen doping of metallic single-walled carbon nanotubes:n-type conduction and dipole scattering. Europhysics Letters (EPL), 77(3):37001, 2007. doi:10.1209/0295-5075/77/37001.

[121] S. Kazaoui, N. Minami, R. Jacquemin, H. Kataura, and Y. Achiba. Amphoteric doping of single-wall carbon-nanotube thin films as probed by optical absorption spectroscopy. Physical Review B, 60(19):13339–13342, 1999. doi:10.1103/PhysRevB.60.13339.

[122] Holger Hartleb, Florian Späth, and Tobias Hertel. Evidence for strong electronic correlations in the spectra of gate-doped single-wall carbon nanotubes. ACS Nano, 9(10):10461–10470, 2015. doi:10.1021/acsnano.5b04707.

[123] Julia Heitmüller. Spektroelektrochemische untersuchungen an kohlenstoff-nanorohrsuspensionen: bachelorarbeit. 2016.

[124] Timothy J. McDonald, Chaiwat Engtrakul, Marcus Jones, Garry Rumbles, and Michael J. Heben. Kinetics of pl quenching during single-walled carbon nanotube rebundling and diameter-dependent surfactant interactions. The journal of physical chemistry. B, 110(50):25339–25346, 2006. doi:10.1021/jp065281x.

[125] Yasuhiko Tanaka, Yasuhiko Hirana, Yasuro Niidome, Koichiro Kato, Susumu Saito, and Naotoshi Nakashima. Experimentally determined redox potentials of individual (n,m) single-walled carbon nanotubes. Angewandte Chemie International Edition in English, 48(41):7655–7659, 2009. doi:10.1002/anie.200902468.

[126] Yasuhiko Hirana, Gergely Juhasz, Yuhei Miyauchi, Shinichiro Mouri, Kazunari Matsuda, and Naotoshi Nakashima. Empirical prediction of electronic potentials of single-walled carbon nanotubes with a specific chirality (n,m). Scientific reports, 3:2959, 2013. doi:10.1038/srep02959.

[127] Liu Hong, Shinichiro Mouri, Yuhei Miyauchi, Kazunari Matsuda, and Naotoshi Nakashima. Redox properties of a single (7,5)single-walled carbon nanotube determined by an in situ photoluminescence spectroelectrochemical method. Nanoscale, 6(21):12798–12804, 2014. doi:10.1039/c4nr03945a.

[128] Holger Edgar Heinz Erich Hartleb. Spektroelektrochemische Untersuchung von halbleitenden Kohlenstoffnanoröhren. PhD thesis, Uni Würzburg, Würzburg, 2015.

[129] Yonghai Cao, Hao Yu, Jun Tan, Feng Peng, Hongjuan Wang, Jing Li, Wenxu Zheng, and Ning-Bew Wong. Nitrogen-, phosphorous- and boron-doped carbon nanotubes as catalysts for the aerobic oxidation of cyclohexane. Carbon, 57:433–442, 2013. doi:10.1016/j.carbon.2013.02.016.

[130] Theerapol Thurakitseree, Christian Kramberger, Pei Zhao, Shinya Aikawa, Sivasankaran Harish, Shohei Chiashi, Erik Einarsson, and Shigeo Maruyama. Diameter-controlled and nitrogen-doped vertically aligned single-walled carbon nanotubes. Carbon, 50(7):2635–2640, 2012. doi:10.1016/j.carbon.2012.02.023.

[131] Souza Filho, A. G., A. Jorio, Ge. G. Samsonidze, G. Dresselhaus, Pimenta, M. A., M. S. Dresselhaus, Anna K. Swan, M. S. Ünlü, B. B. Goldberg, and R. Saito. Competing spring constant versus double resonance effects on the properties of dispersive modes in isolated single-wall carbon nanotubes. Physical Review B, 2003. doi:10.1103/PhysRevB.67.035427.

[132] Tobias Hertel, Sabine Himmelein, Thomas Ackermann, Dominik Stich, and Jared Crochet. Diffusion limited photoluminescence quantum yields in 1-d semiconductors: single-wall carbon nanotubes. ACS Nano, 4(12):7161–7168, 2010. doi:10.1021/nn101612b.

[133] Saunab Ghosh, Sergei M. Bachilo, and Weisman, R. Bruce. Advanced sorting of single-walled carbon nanotubes by nonlinear density-gradient ultracentrifugation. Nature nanotechnology, 5(6):443–450, 2010. doi:10.1038/nnano.2010.68.

[134] Shin Young Kim, Jinyoung Lee, Chan Woong Na, Jeunghee Park, Kwanyong Seo, and Bongsoo Kim. N-doped double-walled carbon nanotubes synthesized by chemical vapor deposition. Chemical Physics Letters, 413(4-6):300–305, 2005. doi:10.1016/j.cplett.2005.07.093.

[135] Christian Kramberger, Theerapol Thurakitseree, Erik Einarsson, Akito Takashima, Toyohiko Kinoshita, Takayuki Muro, and Shigeo Maruyama. From isotope labeled

ch_3cn to n_2 inside single-walled carbon nanotubes. Nanoscale, 6(3):1525–1528, 2014. doi:10.1039/c3nr04729f.

[136] A. Ishii, M. Yoshida, and Y. K. Kato. Exciton diffusion, end quenching, and exciton-exciton annihilation in individual air-suspended carbon nanotubes. Physical Review B, 2015. doi:10.1103/PhysRevB.91.125427.

[137] Carsten Georgi, Miriam Böhmler, Huihong Qian, Lukas Novotny, and Achim Hartschuh. Probing exciton propagation and quenching in carbon nanotubes with near-field optical microscopy. Physica Status Solidi B: Basic Solid State Physics, 246(11-12):2683–2688, 2009. doi:10.1002/pssb.200982306.

[138] Juan G. Duque, Matteo Pasquali, Laurent Cognet, and Brahim Lounis. Environmental and synthesis-dependent luminescence properties of individual single-walled carbon nanotubes. ACS nano, 3(8):2153–2156, 2009. doi:10.1021/nn9003956.

[139] Dmitri A. Tsyboulski, Sergei M. Bachilo, and Weisman, R. Bruce. Versatile visualization of individual single-walled carbon nanotubes with near-infrared fluorescence microscopy. Nano Letters, 5(5):975–979, 2005. doi:10.1021/nl050366f.

[140] Sidney Redner. A Guide To First-Passage Processes. Cambridge University Press, Cambridge, 2001. ISBN 9780511606014. doi:10.1017/CBO9780511606014.

[141] Mitchell D. Anderson, Yee-fang Xiao, and James M. Fraser. First-passage theory of exciton population loss in single-walled carbon nanotubes reveals micron-scale intrinsic diffusion lengths. Physical Review B, 2013. doi:10.1103/PhysRevB.88.045420.

[142] Friedrich Schöppler, Christoph Mann, Tilman C. Hain, Felix M. Neubauer, Giulia Privitera, Francesco Bonaccorso, Daping Chu, Andrea C. Ferrari, and Tobias Hertel. Molar extinction coefficient of single-wall carbon nanotubes. The Journal of Physical Chemistry C, 115(30):14682–14686, 2011. doi:10.1021/jp205289h.

[143] Stéphane Berciaud, Laurent Cognet, and Brahim Lounis. Luminescence decay and the absorption cross section of individual single-walled carbon nanotubes. Physical review letters, 101(7):077402, 2008. doi:10.1103/PhysRevLett.101.077402.

[144] Christoph Mann and Tobias Hertel. 13 nm exciton size in (6,5) single-wall carbon nanotubes. The Journal of Physical Chemistry Letters, 7(12):2276–2280, 2016. doi:10.1021/acs.jpclett.6b00797.

[145] Daniel Schilling, Christoph Mann, Pascal Kunkel, Friedrich Schöppler, and Tobias Hertel. Ultrafast spectral exciton diffusion in single-wall carbon nanotubes studied by time-resolved hole burning. The Journal of Physical Chemistry C, 119(42):24116–24123, 2015. doi:10.1021/acs.jpcc.5b06865.

[146] Larry Lüer, Sajjad Hoseinkhani, Dario Polli, Jared Crochet, Tobias Hertel, and Guglielmo Lanzani. Size and mobility of excitons in (6, 5) carbon nanotubes. Nature Physics, 5(1):54–58, 2009. doi:10.1038/nphys1149.

[147] Carsten Georgi, Nicolai Hartmann, Tobias Gokus, Alexander A. Green, Mark C. Hersam, and Achim Hartschuh. Photoinduced luminescence blinking and bleaching in individual single-walled carbon nanotubes. Chemphyschem, 9(10):1460–1464, 2008. doi:10.1002/cphc.200800179.

[148] Laurent Cognet, Dmitri A. Tsyboulski, John-David R. Rocha, Condell D. Doyle, James M. Tour, and Weisman, R. Bruce. Stepwise quenching of exciton fluorescence in carbon nanotubes by single-molecule reactions. Science, 316(5830):1465–1468, 2007. doi:10.1126/science.1141316.

[149] Yuhei Miyauchi, Munechiyo Iwamura, Shinichiro Mouri, Tadashi Kawazoe, Motoichi Ohtsu, and Kazunari Matsuda. Brightening of excitons in carbon nanotubes on dimensionality modification. Nature Photonics, 7(9):715–719, 2013. doi:10.1038/nphoton.2013.179.

[150] Christoph Mann. Exzitonengröße und -dynamik in (6,5)-Kohlenstoffnanoröhren : Transiente Absorptions- und Photolumineszenzmessungen. PhD thesis, Universität Würzburg, Würzburg, 2015. URL: https://nbn-resolving.org/urn:nbn:de:bvb:20-opus-123407.

[151] Jacques Lefebvre and Paul Finnie. Excited excitonic states in single-walled carbon nanotubes. Nano Letters, 8(7):1890–1895, 2008. doi:10.1021/nl080518h.

[152] Wei Ting Chen, Mohammadreza Khorasaninejad, Alexander Y. Zhu, Jaewon Oh, Robert C. Devlin, Aun Zaidi, and Federico Capasso. Generation of wavelength-independent subwavelength bessel beams using metasurfaces. Light, science & applications, 6(5):e16259, 2017. doi:10.1038/lsa.2016.259.

[153] Z. Bouchal, J. Wagner, and M. Chlup. Self-reconstruction of a distorted nondiffracting beam. Optics Communications, 151(4-6):207–211, 1998. doi:10.1016/S0030-4018(98)00085-6.

[154] Durnin, Miceli, and Eberly. Diffraction-free beams. Physical review letters, 58(15):1499–1501, 1987. doi:10.1103/PhysRevLett.58.1499.

[155] Tilman Christian Hain. Entwicklung eines experimentellen Aufbaus zur Charakterisierung nanoskaliger Systeme mittels Fluoreszenzspektroskopie und -mikroskopie. PhD thesis, Universität Würzburg, Würzburg, 2015.

[156] Jacques Lefebvre, David G. Austing, Jeffery Bond, and Paul Finnie. Photoluminescence imaging of suspended single-walled carbon nanotubes. Nano Letters, 6(8):1603–1608, 2006. doi:10.1021/nl060530e.

[157] S. Reich, C. Thomsen, and P. Ordejón. Electronic band structure of isolated and bundled carbon nanotubes. Physical Review B, 65(15):2506, 2002. doi:10.1103/PhysRevB.65.155411.

[158] Feng Wang, Matthew Y. Sfeir, Limin Huang, X. M. Henry Huang, Yang Wu, Jaehee Kim, James Hone, Stephen O'Brien, Louis E. Brus, and Tony F. Heinz. Interactions between individual carbon nanotubes studied by rayleigh scattering spectroscopy. Physical review letters, 96(16):167401, 2006. doi:10.1103/PhysRevLett.96.167401.

[159] Y. Miyauchi, R. Saito, K. Sato, Y. Ohno, S. Iwasaki, T. Mizutani, J. Jiang, and S. Maruyama. Dependence of exciton transition energy of single-walled carbon nanotubes on surrounding dielectric materials. Chemical Physics Letters, 442(4-6):394–399, 2007. doi:10.1016/j.cplett.2007.06.018.

[160] Anni J. Siitonen, Dmitri A. Tsyboulski, Sergei M. Bachilo, and Weisman, R. Bruce. Surfactant-dependent exciton mobility in single-walled carbon nanotubes studied by single-molecule reactions. Nano Letters, 10(5):1595–1599, 2010. doi:10.1021/nl9039845.

[161] Keith Bradley, Jean-Christophe P. Gabriel, Mikhail Briman, Alexander Star, and George Grüner. Charge transfer from ammonia physisorbed on nanotubes. Physical review letters, 91(21):218301, 2003. doi:10.1103/PhysRevLett.91.218301.

[162] Kong, Franklin, Zhou, Chapline, Peng, Cho, and Dai. Nanotube molecular wires as chemical sensors. Science (New York, N.Y.), 287(5453):622–625, 2000. doi:10.1126/science.287.5453.622.

[163] Jean-Joseph Adjizian, Radouane Leghrib, Antal A. Koos, Irene Suarez-Martinez, Alison Crossley, Philipp Wagner, Nicole Grobert, Eduard Llobet, and Christopher P. Ewels. Boron- and nitrogen-doped multi-wall carbon nanotubes for gas detection. Carbon, 66:662–673, 2014. doi:10.1016/j.carbon.2013.09.064.

[164] Jing Kong and Hongjie Dai. Full and modulated chemical gating of individual carbon nanotubes by organic amine compounds. Journal of Physical Chemistry B, 105(15):2890–2893, 2001. doi:10.1021/jp0101312.

[165] Collins, Bradley, Ishigami, and Zettl. Extreme oxygen sensitivity of electronic properties of carbon nanotubes. Science, 287(5459):1801–1804, 2000. doi:10.1126/science.287.5459.1801.

[166] Hendrik Ulbricht, Gunnar Moos, and Tobias Hertel. Physisorption of molecular oxygen on single-wall carbon nanotube bundles and graphite. Physical Review B, 2002. doi:10.1103/PhysRevB.66.075404.

[167] Hendrik Ulbricht, Jennah Kriebel, Gunnar Moos, and Tobias Hertel. Desorption kinetics and interaction of xe with single-wall carbon nanotube bundles. Chemical Physics Letters, 363(3-4):252–260, 2002. doi:10.1016/S0009-2614(02)01175-2.

[168] Hugo E. Romero, Kim Bolton, Arne Rosén, and Peter C. Eklund. Atom collision-induced resistivity of carbon nanotubes. Science (New York, N.Y.), 307(5706):89–93, 2005. doi:10.1126/science.1102004.

[169] Takushi Uda, Akihiro Ishii, and Yuichiro K. Kato. Single carbon nanotubes as ultrasmall all-optical memories. ACS Photonics, 5(2):559–565, 2017. doi:10.1021/acsphotonics.7b01104.

[170] Shohei Chiashi, Satoshi Watanabe, Tateki Hanashima, and Yoshikazu Homma. Influence of gas adsorption on optical transition energies of single-walled carbon nanotubes. Nano Letters, 8(10):3097–3101, 2008. doi:10.1021/nl801074j.

[171] T. P. Chua, M. Mariatti, A. Azizan, and A. A. Rashid. Surface functionalization of multi-walled carbon nanotubes via electron reduction of benzophenone by potassium metal. Journal of Alloys and Compounds, 480(2):534–536, 2009. doi:10.1016/j.jallcom.2009.01.093.

[172] Lei An, Qiang Fu, Chenguang Lu, and Jie Liu. A simple chemical route to selectively eliminate metallic carbon nanotubes in nanotube network devices. Journal of the American Chemical Society, 126(34):10520–10521, 2004. doi:10.1021/ja046482m.

[173] Nanda Gopal Sahoo, Henry Kuo Feng Cheng, Hongqian Bao, Yongzheng Pan, Lin Li, and Siew Hwa Chan. Covalent functionalization of carbon nanotubes for ultimate interfacial adhesion to liquid crystalline polymer. Soft Matter, 7(19):9505, 2011. doi:10.1039/c1sm05360d.

[174] Shadpour Mallakpour and Samaneh Soltanian. Surface functionalization of carbon nanotubes: fabrication and applications. RSC Advances, 6(111):109916–109935, 2016. doi:10.1039/C6RA24522F.

[175] P. Finnie, Y. Homma, and J. Lefebvre. Band-gap shift transition in the photoluminescence of single-walled carbon nanotubes. Physical review letters, 2005. doi:10.1103/PhysRevLett.94.247401.

[176] Yutaka Ohno, Shinya Iwasaki, Yoichi Murakami, Shigeru Kishimoto, Shigeo Maruyama, and Takashi Mizutani. Chirality-dependent environmental effects in photoluminescence of single-walled carbon nanotubes. Physical Review B, 2006. doi:10.1103/PhysRevB.73.235427.

[177] Tsuneya Ando. Environment effects on excitons in semiconducting carbon nanotubes. Journal of the Physics Society Japan, 79(2):024706, 2010. doi:10.1143/JPSJ.79.024706.

[178] Vasili Perebeinos, J. Tersoff, and Phaedon Avouris. Scaling of excitons in carbon nanotubes. Physical review letters, 92(25 Pt 1):257402, 2004. doi:10.1103/PhysRevLett.92.257402.

[179] Yoshikazu Homma, Shohei Chiashi, Takahiro Yamamoto, Kaname Kono, Daiki Matsumoto, Junpei Shitaba, and Shintaroh Sato. Photoluminescence measurements and molecular dynamics simulations of water adsorption on the hydrophobic surface of a carbon nanotube in water vapor. Physical review letters, 110(15):157402, 2013. doi:10.1103/PhysRevLett.110.157402.

[180] Juan G. Duque, Christopher E. Hamilton, Gautam Gupta, Scott A. Crooker, Jared J. Crochet, Aditya Mohite, Han Htoon, Kimberly A. DeFriend Obrey, Andrew M. Dattelbaum, and Stephen K. Doorn. Fluorescent single-walled carbon nanotube aerogels in surfactant-free environments. ACS nano, 5(8):6686–6694, 2011. doi:10.1021/nn202225k.

[181] Mingyuan Huang, Yang Wu, Bhupesh Chandra, Hugen Yan, Yuyao Shan, Tony F. Heinz, and James Hone. Direct measurement of strain-induced changes in the band structure of carbon nanotubes. Physical Review Letters, 100(13):136803, 2008. doi:10.1103/PhysRevLett.100.136803.

[182] D. E. Milkie, C. Staii, S. Paulson, E. Hindman, A. T. Johnson, and J. M. Kikkawa. Controlled switching of optical emission energies in semiconducting single-walled carbon nanotubes. Nano Letters, 5(6):1135–1138, 2005. doi:10.1021/nl050688j.

[183] Kyung Ah Park, Kwanyong Seo, and Young Hee Lee. Adsorption of atomic hydrogen on single-walled carbon nanotubes. The journal of physical chemistry. B, 109(18):8967–8972, 2005. doi:10.1021/jp0500743.

[184] Kotaro Nagatsu, Shohei Chiashi, Satoru Konabe, and Yoshikazu Homma. Brightening of triplet dark excitons by atomic hydrogen adsorption in single-walled carbon nanotubes observed by photoluminescence spectroscopy. Physical review letters, 105(15):157403, 2010. doi:10.1103/PhysRevLett.105.157403.

[185] T. W. Ebbesen and T. Takada. Topological and sp3 defect structures in nanotubes. Carbon, 33(7):973–978, 1995. doi:10.1016/0008-6223(95)00025-9.

[186] Guangyu Zhang, Pengfei Qi, Xinran Wang, Yuerui Lu, David Mann, Xiaolin Li, and Hongjie Dai. Hydrogenation and hydrocarbonation and etching of single-walled carbon nanotubes. Journal of the American Chemical Society, 128(18):6026–6027, 2006. doi:10.1021/ja061324b.

[187] L. Backman. A novel co/sio2 catalyst for hydrogenation. Catalysis Today, 43(1-2):11–19, 1998. doi:10.1016/S0920-5861(98)00132-1.

[188] H. Qian and E. L. Elson. On the analysis of high order moments of fluorescence fluctuations. Biophysical Journal, 57(2):375–380, 1990. doi:10.1016/S0006-3495(90)82539-X.

[189] Rafael Brüschweiler and Fengli Zhang. Covariance nuclear magnetic resonance spectroscopy. Journal of Chemical Physics, 120(11):5253–5260, 2004. doi:10.1063/1.1647054.

[190] Martin Jaeger and Ruud L.E.G. Aspers. Covariance nmr and small molecule applications. In Graham A. Webb, editor, Annual Reports on NMR Spectroscopy, volume 83, pages 271–349. Elsevier, 2014. doi:10.1016/B978-0-12-800183-7.00005-8.

[191] Jason K. Streit, Sergei M. Bachilo, Stephen R. Sanchez, Ching-Wei Lin, and Weisman, R. Bruce. Variance spectroscopy. The journal of physical chemistry letters, 6(19):3976–3981, 2015. doi:10.1021/acs.jpclett.5b01835.

[192] Stephen R. Sanchez, Sergei M. Bachilo, Yara Kadria-Vili, Ching-Wei Lin, and Weisman, R. Bruce. (n,m)-specific absorption cross sections of single-walled carbon nanotubes measured by variance spectroscopy. Nano letters, 16(11):6903–6909, 2016. doi:10.1021/acs.nanolett.6b02819.

[193] Stephen R. Sanchez, Sergei M. Bachilo, Yara Kadria-Vili, and Weisman, R. Bruce. Skewness analysis in variance spectroscopy measures nanoparticle individualization. The Journal of Physical Chemistry Letters, 8(13):2924–2929, 2017. doi:10.1021/acs.jpclett.7b01184.

[194] S. D. M. Brown, A. Jorio, M. S. Dresselhaus, and G. Dresselhaus. Observations of the d -band feature in the raman spectra of carbon nanotubes. Physical Review B, 64(7):1126, 2001. doi:10.1103/PhysRevB.64.073403.

[195] Yara Kadria-Vili, Sergei M. Bachilo, Jeffrey L. Blackburn, and Weisman, R. Bruce. Photoluminescence side band spectroscopy of individual single-walled carbon nanotubes. The Journal of Physical Chemistry C, 120(41):23898–23904, 2016. doi:10.1021/acs.jpcc.6b08768.

[196] Nicolai F. Hartmann, Kirill A. Velizhanin, Erik H. Haroz, Mijin Kim, Xuedan Ma, YuHuang Wang, Han Htoon, and Stephen K. Doorn. Photoluminescence dynamics of aryl sp(3) defect states in single-walled carbon nanotubes. ACS nano, 10(9):8355–8365, 2016. doi:10.1021/acsnano.6b02986.

[197] Hyejin Kwon, Mijin Kim, Brendan Meany, Yanmei Piao, Lyndsey R. Powell, and YuHuang Wang. Optical probing of local ph and temperature in complex fluids with covalently functionalized, semiconducting carbon nanotubes. The Journal of Physical Chemistry C, 119(7):3733–3739, 2015. doi:10.1021/jp509546d.

[198] Yanmei Piao, Brendan Meany, Lyndsey R. Powell, Nicholas Valley, Hyejin Kwon, George C. Schatz, and YuHuang Wang. Brightening of carbon nanotube photoluminescence through the incorporation of sp3 defects. Nature chemistry, 5(10):840–845, 2013. doi:10.1038/nchem.1711.

[199] Saunab Ghosh, Sergei M. Bachilo, Rebecca A. Simonette, Kathleen M. Beckingham, and Weisman, R. Bruce. Oxygen doping modifies near-infrared band gaps in fluorescent single-walled carbon nanotubes. Science, 330(6011):1656–1659, 2010. doi:10.1126/science.1196382.

[200] Amanda R. Amori, Jamie E. Rossi, Brian J. Landi, and Todd D. Krauss. Defects enable dark exciton photoluminescence in single-walled carbon nanotubes. The Journal of Physical Chemistry C, 122(6):3599–3607, 2018. doi:10.1021/acs.jpcc.7b10565.

[201] Jayakumar Balakrishnan, Gavin Kok Wai Koon, Manu Jaiswal, Castro Neto, A. H., and Barbaros Özyilmaz. Colossal enhancement of spin–orbit coupling in weakly hydrogenated graphene. Nature Physics, 9(5):284–287, 2013. doi:10.1038/nphys2576.

[202] Dmitry V. Kazachkin, Yoshifumi Nishimura, Stephan Irle, Xue Feng, Radisav Vidic, and Eric Borguet. Temperature and pressure dependence of molecular adsorption on single wall carbon nanotubes and the existence of an "adsorption/desorption pressure gap". Carbon, 48(7):1867–1875, 2010. doi:10.1016/j.carbon.2009.11.018.

[203] Jonathan C. Noe, Manuel Nutz, Jonathan Reschauer, Nicolas Morell, Ioannis Tsioutsios, Antoine Reserbat-Plantey, Kenji Watanabe, Takashi Taniguchi, Adrian Bachtold, and Alexander Högele. Environmental electrometry with luminescent carbon nanotubes. Nano letters, 18(7):4136–4140, 2018. doi:10.1021/acs.nanolett.8b00871.

[204] Achim Hartschuh, Hermeneglido N. Pedrosa, Lukas Novotny, and Todd D. Krauss. Simultaneous fluorescence and raman scattering from single carbon nanotubes. Science, 301(5638):1354–1356, 2003. doi:10.1126/science.1087118.

[205] Arthur I. Vogel and B. S. Furniss. Vogel's textbook of practical organic chemistry. Longman Scientific & Technical, 5th ed. edition, 1989. ISBN 9780582462366.

[206] Hang Woo Lee, Yeohoon Yoon, Steve Park, Joon Hak Oh, Sanghyun Hong, Luckshitha S. Liyanage, Huiliang Wang, Satoshi Morishita, Nishant Patil, Young Jun Park, Jong Jin Park, Andrew Spakowitz, Giulia Galli, Francois Gygi, Philip H-S Wong, Jeffrey B-H Tok, Jong Min Kim, and Zhenan Bao. Selective dispersion of high purity semiconducting single-walled carbon nanotubes with regioregular poly(3-alkylthiophene)s. Nature communications, 2:541, 2011. doi:10.1038/ncomms1545.

[207] Yutaka Ohno, Shinya Iwasaki, Yoichi Murakami, Shigeru Kishimoto, Shigeo Maruyama, and Takashi Mizutani. Excitonic transition energies in single-walled carbon nanotubes: dependence on environmental dielectric constant. physica status solidi (b), 244(11):4002–4005, 2007. doi:10.1002/pssb.200776124.

[208] Tobias Hertel. Photophysics. In Dirk M. Guldi and Nazario Martn, editors, Carbon Nanotubes and Related Structures, pages 77–101. Wiley-VCH Verlag GmbH & Co. KGaA, Weinheim, Germany, 2010. doi:10.1002/9783527629930.ch4.

[209] Tetsuo Ogawa and Toshihide Takagahara. Interband absorption spectra and sommerfeld factors of a one-dimensional electron-hole system. Physical Review B, 43(17):14325–14328, 1991. doi:10.1103/PhysRevB.43.14325.

[210] Huiliang Wang, Bing Hsieh, Gonzalo Jiménez-Osés, Peng Liu, Christopher J. Tassone, Ying Diao, Ting Lei, Kendall N. Houk, and Zhenan Bao. Solvent effects on polymer sorting of carbon nanotubes with applications in printed electronics. Small, 11(1):126–133, 2015. doi:10.1002/smll.201401890.

[211] Long Qian, Wenya Xu, XiaoFeng Fan, Chao Wang, Jianhui Zhang, Jianwen Zhao, and Zheng Cui. Electrical and photoresponse properties of printed thin-film transistors based on poly(9,9-dioctylfluorene- co -bithiophene) sorted large-diameter semiconducting carbon nanotubes. The Journal of Physical Chemistry C, 117(35):18243–18250, 2013. doi:10.1021/jp4055022.

[212] J. Lefebvre, J. M. Fraser, P. Finnie, and Y. Homma. Photoluminescence from an individual single-walled carbon nanotube. Physical Review B, 69(7):593, 2004. doi:10.1103/PhysRevB.69.075403.

[213] Imge Namal. Fabrication and Optical and Electronic Characterization of Conjugated Polymer-Stabilized Semiconducting Single-Wall Carbon Nanotubes in Dispersions and Thin Films. Universität Würzburg, Würzburg, 2018.

[214] Kazunari Matsuda, Tadashi Inoue, Yoichi Murakami, Shigeo Maruyama, and Yoshihiko Kanemitsu. Exciton dephasing and multiexciton recombinations in a single carbon nanotube. Physical Review B, 77(3):033406, 2008. doi:10.1103/PhysRevB.77.033406.

[215] Xu Wang, Jack A. Alexander-Webber, Wei Jia, Benjamin P. L. Reid, Samuel D. Stranks, Mark J. Holmes, Christopher C. S. Chan, Chaoyong Deng, Robin J. Nicholas, and Robert A. Taylor. Quantum dot-like excitonic behavior in individual single walled-carbon nanotubes. Scientific reports, 6(1):719, 2016. doi:10.1038/srep37167.

[216] O. N. Torrens, M. Zheng, and J. M. Kikkawa. Energy of k-momentum dark excitons in carbon nanotubes by optical spectroscopy. Physical review letters, 101(15):157401, 2008. doi:10.1103/PhysRevLett.101.157401.

[217] Ming Zheng, Anand Jagota, Ellen D. Semke, Bruce A. Diner, Robert S. McLean, Steve R. Lustig, Raymond E. Richardson, and Nancy G. Tassi. Dna-assisted dispersion and separation of carbon nanotubes. Nature materials, 2(5):338–342, 2003. doi:10.1038/nmat877.

[218] Kerstin Müller. tba. PhD thesis, Uni Würzburg, Würzburg, 2019 (tbp).

[219] Frank Brunecker. Kohlenstoffnanorohr-Komplexe: Adsorption und Desorption von (Bio-)Polymeren. PhD thesis, Uni Würzburg, Würzburg, 2015.

[220] P. Alston Steiner and W. Gordy. Precision measurement of dipole moments and other spectral constants of normal and deuterated methyl fluoride and methyl cyanide. Journal of Molecular Spectroscopy, 21(1-4):291–301, 1966. doi:10.1016/0022-2852(66)90152-4.

[221] Po-Yu Yang, Shin-Pon Ju, Hua-Sheng Hsieh, and Jenn-Sen Lin. The diffusion behavior and capacitance of tetraethylammonium/tetrafluoroborate ions in acetonitrile with different molar concentrations: a molecular dynamics study. RSC Advances, 7(87):55044–55050, 2017. doi:10.1039/c7ra09465e.

[222] M. Yoshida, A. Popert, and Y. K. Kato. Gate-voltage induced trions in suspended carbon nanotubes. Physical Review B, 2016. doi:10.1103/physrevb.93.041402.

[223] Don N. Futaba, Kenji Hata, Takeo Yamada, Tatsuki Hiraoka, Yuhei Hayamizu, Yozo Kakudate, Osamu Tanaike, Hiroaki Hatori, Motoo Yumura, and Sumio Iijima. Shape-engineerable and highly densely packed single-walled carbon nanotubes and their application as super-capacitor electrodes. Nature materials, 5(12):987–994, 2006. doi:10.1038/nmat1782.

[224] Yuhei Miyauchi, Mototeru Oba, and Shigeo Maruyama. Cross-polarized optical absorption of single-walled nanotubes by polarized photoluminescence excitation spectroscopy. Physical Review B, 2006. doi:10.1103/PhysRevB.74.205440.

[225] Seiji Uryu and Tsuneya Ando. Exciton absorption of perpendicularly polarized light in carbon nanotubes. Physical Review B, 74(15):107, 2006. doi:10.1103/PhysRevB.74.155411.

[226] Yoichi Murakami, Benjamin Lu, Said Kazaoui, Nobutsugu Minami, Tatsuya Okubo, and Shigeo Maruyama. Photoluminescence sidebands of carbon nanotubes below the bright singlet excitonic levels. Physical Review B, 2009. doi:10.1103/PhysRevB.79.195407.

[227] Vasili Perebeinos, J. Tersoff, and Phaedon Avouris. Effect of exciton-phonon coupling in the calculated optical absorption of carbon nanotubes. Physical Review Letters, 94(2):027402, 2005. doi:10.1103/PhysRevLett.94.027402.

[228] Jeffrey L. Blackburn, Josh M. Holt, Veronica M. Irurzun, Daniel E. Resasco, and Garry Rumbles. Confirmation of k-momentum dark exciton vibronic sidebands using 13c-labeled, highly enriched (6,5) single-walled carbon nanotubes. Nano letters, 12(3):1398–1403, 2012. doi:10.1021/nl204072x.

[229] T. Uda, M. Yoshida, A. Ishii, and Y. K. Kato. Electric-field induced activation of dark excitonic states in carbon nanotubes. Nano letters, 16(4):2278–2282, 2016. doi:10.1021/acs.nanolett.5b04595.

[230] Peter Linstrom. Nist chemistry webbook, nist standard reference database 69. doi:10.18434/T4D303.

[231] Krzysztof Bernard Beć, Daniel Karczmit, Michał Kwaśniewicz, Yukihiro Ozaki, and Mirosław Antoni Czarnecki. Overtones of vc≡n vibration as a probe of structure of liquid ch 3 cn, cd 3 cn, and ccl 3 cn: combined infrared, near-infrared, and raman spectroscopic studies with anharmonic density functional theory calculations. The Journal of Physical Chemistry A, 123(20):4431–4442, 2019. doi:10.1021/acs.jpca.9b02170.

[232] L. Nitin Seetohul, Zulfiqur Ali, and Meez Islam. Liquid-phase broadband cavity enhanced absorption spectroscopy (bbceas) studies in a 20 cm cell. The Analyst, 134(9):1887–1895, 2009. doi:10.1039/b907316g.

[233] Vitaly Chaban. Filling carbon nanotubes with liquid acetonitrile. Chemical Physics Letters, 496(1-3):50–55, 2010. doi:10.1016/j.cplett.2010.07.003.

[234] Yutaka Maniwa, Hiromichi Kataura, Masatoshi Abe, Akiko Udaka, Shinzo Suzuki, Yohji Achiba, Hiroshi Kira, Kazuyuki Matsuda, Hiroaki Kadowaki, and Yutaka Okabe. Ordered water inside carbon nanotubes: formation of pentagonal to octagonal ice-nanotubes. Chemical Physics Letters, 401(4-6):534–538, 2005. doi:10.1016/j.cplett.2004.11.112.

[235] W. Wenseleers, S. Cambré, J. Čulin, A. Bouwen, and E. Goovaerts. Effect of water filling on the electronic and vibrational resonances of carbon nanotubes: characterizing tube opening by raman spectroscopy. Advanced Materials, 19(17):2274–2278, 2007. doi:10.1002/adma.200700773.

[236] Sofie Cambré, Bob Schoeters, Sten Luyckx, Etienne Goovaerts, and Wim Wenseleers. Experimental observation of single-file water filling of thin single-wall carbon nanotubes down to chiral index (5,3). Physical Review Letters, 104(20):207401, 2010. doi:10.1103/PHYSREVLETT.104.207401.

[237] Sofie Cambré, Silvia M. Santos, Wim Wenseleers, Ahmad R. T. Nugraha, Riichiro Saito, Laurent Cognet, and Brahim Lounis. Luminescence properties of individual empty and water-filled single-walled carbon nanotubes. ACS Nano, 6(3):2649–2655, 2012. doi:10.1021/NN300035Y.

[238] Jhinhwan Lee, H. Kim, S-J Kahng, G. Kim, Y-W Son, J. Ihm, H. Kato, Z. W. Wang, T. Okazaki, H. Shinohara, and Young Kuk. Bandgap modulation of carbon nanotubes by encapsulated metallofullerenes. Nature, 415(6875):1005–1008, 2002. doi:10.1038/4151005a.

[239] Sofie Cambré, Jochen Campo, Charlie Beirnaert, Christof Verlackt, Pegie Cool, and Wim Wenseleers. Asymmetric dyes align inside carbon nanotubes to yield a large nonlinear optical response. Nature nanotechnology, 10(3):248–252, 2015. doi:10.1038/nnano.2015.1.

[240] Thomas A. Ford and Leslie Glasser. Ab initio calculations of the structural, energetic, and vibrational properties of some hydrogen bonded and van der waals dimers. part 4. the acetonitrile dimer. International Journal of Quantum Chemistry, 84(2):226–240, 2001. doi:10.1002/qua.1325.

[241] M. Szlachta and P. Wójtowicz. Adsorption of methylene blue and congo red from aqueous solution by activated carbon and carbon nanotubes. Water science and technology : a journal of the International Association on Water Pollution Research, 68(10):2240–2248, 2013. doi:10.2166/wst.2013.487.

[242] Bruce R. Weisman and Sergei M. Bachilo. Dependence of optical transition energies on structure for single-walled carbon nanotubes in aqueous suspension: an empirical kataura plot. Nano Letters, 3(9):1235–1238, 2003. doi:10.1021/nl034428i.

[243] Valerie C. Moore, Michael S. Strano, Erik H. Haroz, Robert H. Hauge, Richard E. Smalley, Judith Schmidt, and Yeshayahu Talmon. Individually suspended single-walled carbon nanotubes in various surfactants. Nano Letters, 3(10):1379–1382, 2003. doi:10.1021/nl034524j.

[244] Tsuyohiko Fujigaya and Naotoshi Nakashima. Non-covalent polymer wrapping of carbon nanotubes and the role of wrapped polymers as functional dispersants. Science and Technology of Advanced Materials, 16(2):024802, 2015. doi:10.1088/1468-6996/16/2/024802.

[245] Jose M. Lobez and Ali Afzali. Surface-selective directed assembly of carbon nanotubes using side-chain functionalized poly(thiophene)s. Chemistry of Materials, 25(18):3662–3666, 2013. doi:10.1021/cm401881w.

[246] Ninette Stürzl, Frank Hennrich, Sergei Lebedkin, and Manfred M. Kappes. Near monochiral single-walled carbon nanotube dispersions in organic solvents. The Journal of Physical Chemistry C, 113(33):14628–14632, 2009. doi:10.1021/jp902788y.

[247] Hiroaki Ozawa, Tsuyohiko Fujigaya, Suhee Song, Hongsuk Suh, and Naotoshi Nakashima. Different chiral selective recognition/extraction of (n,m)single-walled carbon nanotubes using copolymers carrying a carbazole or fluorene moiety. Chemistry Letters, 40(5):470–472, 2011. doi:10.1246/cl.2011.470.

[248] Jorge Mario Salazar-Rios, Wytse Talsma, Vladimir Derenskyi, Widianta Gomulya, Tina Keller, Martin Fritsch, Sebastian Kowalski, Eduard Preis, Ming Wang, Sybille Allard, Guillermo Carlos Bazan, Ullrich Scherf, Maria Cristina dos Santos, and Maria Antonietta Loi. Understanding the selection mechanism of the polymer wrapping technique toward semiconducting carbon nanotubes. Small Methods, 2(4):1700335, 2018. doi:10.1002/smtd.201700335.

[249] Fabien Lemasson, Nicolas Berton, Jana Tittmann, Frank Hennrich, Manfred M. Kappes, and Marcel Mayor. Polymer library comprising fluorene and carbazole homo- and copolymers for selective single-walled carbon nanotubes extraction. Macromolecules, 45(2):713–722, 2012. doi:10.1021/ma201890g.

[250] Frank K. Brunecker, Friedrich Schöppler, and Tobias Hertel. Interaction of polymers with single-wall carbon nanotubes. The Journal of Physical Chemistry C, 120(18):10094–10103, 2016. doi:10.1021/acs.jpcc.6b02198.

[251] Samuel D. Stranks, Anton M. R. Baker, Jack A. Alexander-Webber, Beate Dirks, and Robin J. Nicholas. Production of high-purity single-chirality carbon nanotube hybrids by selective polymer exchange. Small, 9(13):2245–2249, 2013. doi:10.1002/smll.201202434.

[252] Jian Chen, Haiying Liu, Wayne A. Weimer, Mathew D. Halls, David H. Waldeck, and Gilbert C. Walker. Noncovalent engineering of carbon nanotube surfaces by rigid, functional conjugated polymers. Journal of the American Chemical Society, 124(31):9034–9035, 2002. doi:10.1021/ja026104m.

[253] Anton V. Naumov, Saunab Ghosh, Dmitri A. Tsyboulski, Sergei M. Bachilo, and Weisman, R. Bruce. Analyzing absorption backgrounds in single-walled carbon nanotube spectra. ACS Nano, 5(3):1639–1648, 2011. doi:10.1021/nn1035922.

[254] Imge Namal, Ali Can Ozelcaglayan, Yasemin Arslan Udum, and Levent Toppare. Synthesis and electrochemical characterization of fluorene and benzimidazole containing novel conjugated polymers: effect of alkyl chain length on electrochemical properties. European Polymer Journal, 49(10):3181–3187, 2013. doi:10.1016/j.eurpolymj.2013.06.016.

[255] Livia N. Glanzmann, Duncan J. Mowbray, and Angel Rubio. Pfo-bpy solubilizers for swnts: modelling of polymers from oligomers. Physica Status Solidi B: Basic Solid State Physics, 251(12):2407–2412, 2014. doi:10.1002/pssb.201451171.

[256] Angela Eckstein, Renata Karpicz, Ramūnas Augulis, Kipras Redeckas, Mikas Vengris, Imge Namal, Tobias Hertel, and Vidmantas Gulbinas. Excitation quenching in polyfluorene polymers bound to (6,5) single-wall carbon nanotubes. Chemical Physics, 467:1–5, 2016. doi:10.1016/j.chemphys.2015.12.006.

[257] Florian Leonhard Späth. Präparation und Charakterisierung einwandiger Kohlenstoffnanorohr-Polyfluoren-Komplexe. PhD thesis, Universität Würzburg, Würzburg, 2015. URL: https://nbn-resolving.org/urn:nbn:de:bvb:20-opus-123874.

[258] James A. Barnes, Andrew R. Chi, Leonard S. Cutler, Daniel J. Healey, David B. Leeson, Thomas E. McGunigal, James A. Mullen, Warren L. Smith, Richard L. Sydnor, Robert F. C. Vessot, and Gernot M. R. Winkler. Characterization of frequency stability. IEEE Transactions on Instrumentation and Measurement, IM-20(2):105–120, 1971. doi:10.1109/TIM.1971.5570702.

[259] David W. Allan. Should the classical variance be used as a basic measure in standards metrology? IEEE Transactions on Instrumentation and Measurement, IM-36(2):646–654, 1987. doi:10.1109/TIM.1987.6312761.